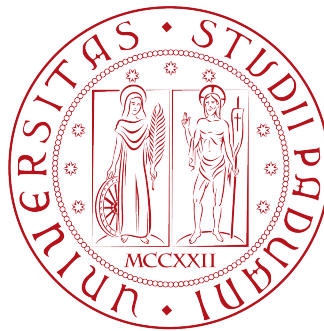


UNIVERSITÀ DEGLI STUDI DI PADOVA

SCUOLA DI INGEGNERIA

Dipartimento di Ingegneria Civile, Edile e Ambientale - ICEA

CORSO DI LAUREA MAGISTRALE IN INGEGNERIA CIVILE



**Mesh independence study of X-FEM  
simulations on fracture propagation in  
porous media**

---

*Relatore:* Chiar.mo Prof. Ing. Andrea Defina

*Correlatore:* Chiar.mo Prof. Ing. Bernhard A. Schrefler

*Correlatore:* Chiar.mo Prof. Ing. Jacques M.R.J. Huyghe

*Controrelatore:* Chiar.mo Prof. Ing. Lorenzo Sanavia

*Candidato:* Paolo Rizzato

*Matricola:* 1041385

---

ANNO ACCADEMICO 2013/2014



*To my parents, Giovanni and Fanny.*



# Contents

<b>List of Figures</b>	<b>iv</b>
<b>List of Tables</b>	<b>vi</b>
<b>1 Introduction</b>	<b>1</b>
1.1 Physical behavior of fractures . . . . .	3
1.2 Fracture models . . . . .	5
1.3 FEM for fracture propagation . . . . .	6
1.4 Computational poroelastic fracturing models . . . . .	11
1.5 Research goal and lay-out of the thesis . . . . .	14
<b>2 The eXtended Finite Element Method (X-FEM)</b>	<b>16</b>
2.1 The problem of mesh dependence . . . . .	16
2.2 The X-FEM applied to cohesive fracture . . . . .	18
2.2.1 Advantages of the X-FEM applied to cohesive fracture . . . . .	21
2.3 Analytical solutions . . . . .	22
2.3.1 Kinematic relations . . . . .	22
2.3.2 Balance equations . . . . .	24
2.3.3 Weak form . . . . .	29
2.4 Numerical description . . . . .	33
2.4.1 Discretized momentum equations . . . . .	37
2.4.2 Discretized mass balance . . . . .	39
2.4.3 Discrete system of equations . . . . .	40
2.5 Cohesive zone method . . . . .	44
2.5.1 Crack nucleation and propagation . . . . .	44
2.5.2 Cohesive zone model . . . . .	49
<b>3 Settings and Parameters</b>	<b>51</b>
3.1 Materials . . . . .	51
3.2 Numerical tools . . . . .	53
3.2.1 Mesh . . . . .	54

---

3.2.2	Numerical model . . . . .	56
3.2.3	Matlab and ParaView . . . . .	57
3.3	Settings . . . . .	59
<b>4</b>	<b>Numerical simulations: results</b>	<b>60</b>
4.1	Physical behavior or numerical artifact? . . . . .	60
4.2	Solid . . . . .	61
4.3	Porous . . . . .	65
4.4	Discussion . . . . .	81
4.4.1	Limitations, recommendations and future work . . . . .	84
<b>5</b>	<b>Conclusions</b>	<b>87</b>
<b>6</b>	<b>Bibliography</b>	<b>88</b>
	<b>Appendix A</b>	<b>105</b>
	<b>Appendix B</b>	<b>108</b>

---

# List of Figures

1.1	Structural failure, American Airlines Flight 587. . . . .	1
1.2	Two examples about the importance of fractures in porous materials. . . . .	2
1.3	Micro-separations and force lines lines around an existing crack. . . . .	4
1.4	Diffuse crack pattern in concrete. . . . .	5
1.5	Early discrete crack modeling. . . . .	7
1.6	Representation of the cohesive zone approach to fracture. . . . .	9
1.7	Close-up representation of the cohesive zone. . . . .	10
1.8	Crack modes used for modeling rock fractures in a reservoir. . . . .	13
1.9	Physical stepwise advancement in hydrogels. . . . .	14
2.1	Normalized tractions across the discontinuity. . . . .	18
2.2	Schematic representation of the Heaviside step function and of the Dirac delta function. . . . .	20
2.3	Crack growth simulation with the X-FEM. . . . .	21
2.4	The body $\Omega$ crossed by discontinuity $\Gamma_d$ , and its boundary conditions. . . . .	22
2.5	Finite element mesh crossed by a discontinuity. . . . .	35
2.6	Numerical integration of quadrilateral elements crossed by a discontinuity. . . . .	36
2.7	Material including at the crack tip global and local coordinate systems. . . . .	45
2.8	2D finite element mesh before and after crack propagation. . . . .	47
2.9	Examples of nucleation checkpoints with corresponding cohesive zones. . . . .	48
2.10	Normalized distribution of the exponential cohesive law for tensile loading. . . . .	50
3.1	Representative volume unit in a porous material. . . . .	52
3.2	Mesh composition. . . . .	54
3.3	Mesh example obtained through Gmsh Mesh Generator. . . . .	55
3.4	Defaults file, an example. . . . .	58
4.1	Cohesive traction zone. . . . .	63
4.2	Solid beam simulation: influence of the applied load. . . . .	64
4.3	Boundary conditions of the beam. . . . .	65
4.4	$\lambda$ effect on rough and smooth mesh: time versus intf plots. . . . .	67

---

4.5	$\lambda$ effect on rough and smooth mesh: time versus Tip0x plots. . . . .	68
4.6	$\lambda$ effect on rough and smooth mesh: d versus intf plots. . . . .	69
4.7	$\lambda$ effect on rough and smooth mesh: d versus Tip0x plots. . . . .	71
4.8	$\lambda$ effect on rough and smooth mesh: Tip0x versus intf plots. . . . .	71
4.9	Comparison between rough, medium and smooth mesh using $\lambda = 0.01$ . . . . .	72
4.10	$\lambda = 0.05$ and new damage model for the cohesive zone permeability. . . . .	74
4.11	Intrinsic permeability and dynamic viscosity effects. . . . .	76
4.12	Intrinsic permeability and dynamic viscosity effects: detailed analysis. . . . .	76
4.13	Differences by using $K_{int} = 5.0e^{-6} \text{ mm}^2$ and $K_{int} = 5.0e^{-12} \text{ mm}^2$ : time versus intf. . . . .	78
4.14	Differences by using $K_{int} = 5.0e^{-6} \text{ mm}^2$ and $K_{int} = 5.0e^{-12} \text{ mm}^2$ : time versus Tip0x. . . . .	78
4.15	Stepwise advancement, part I. . . . .	79
4.16	Stepwise advancement, part II. . . . .	80
4.17	Pressure distribution in a delamination test. . . . .	81
4.18	S22 distribution in the beam under mode I loading. . . . .	81
1	1D consolidation problem. . . . .	100
2	Scheme of the Mandel-Cryer problem. . . . .	102
3	Normalized pressure $\frac{pa}{F}$ over the sample in x-direction. . . . .	103
4	Results for Mandel's problem. . . . .	104
5	Representation of the fibers rotated around an angle $\theta_f$ in the x-y coordinate system. . . . .	108

---



## List of Tables

3.1	Mechanical properties of rocks. . . . .	53
3.2	General mesh values. . . . .	59
4.1	Intrinsic permeability and dynamic viscosity values. . . . .	75
1	Model parameters used for the consolidation benchmark. . . . .	101
2	Model parameters used in the isotropic Mandel-Cryer benchmark. . . .	102

## Abstract

Fracture propagation in porous materials is an important issue in many petroleum and civil engineering problems such as hydraulic fracturing and overtopping stability of dams. In this Thesis an eXtended Finite Element Method (X-FEM) formulation for 2D poroelasticity is presented. Using X-FEM, a fracture is modeled as a discontinuity in the displacement field by exploiting the partition of unity property of finite element shape functions. This step in the displacement field is represented by adding additional degrees of freedom to already existing nodes thus no remeshing is required. A discontinuity can be inserted or extended in any direction and at anytime during the simulation. The fracture process zone is lumped into a single plane ahead of the existing crack by using the cohesive zone approach. Fracture propagation is based on a stress state averaged from the effective stress in the surrounding of the crack tip. Darcy's law is used to calculate the fluid flow in the bulk material. Fluid flow from the formation into the crack and vice versa are accounted for. Several fracture simulations have been done to show the performance of the numerical model.

This research is addressed to investigate if there is a mesh independence fracture propagation in saturated porous media by means of X-FEM simulations. Attention will be focused on the stepwise advancement of a fracture submitted to a mode I crack propagation. Simulations will be performed by testing similar meshes with different element sizes.

# 1: Introduction

In order to better understand the behavior of materials under external loads that lead to failure mechanisms, the study of fracture propagation has become an important issue in engineering.

In fact, predicting the probability of total failure of a structure or its residual strength, requires not only the analysis of the onset of the first damage in the material, but also the investigation of the evolution of the fracture itself.

If the attention is focused on our society, for instance, it can be easily seen that people are usually surrounded by mechanical systems and installations. Nuclear power plant to produce energy; dams to protect cities from floods; power lines to transfer electricity; aeroplanes or high speed trains to travel; satellites to guarantee communications. If one or more of these structures fail, the consequences can be very serious (see Figure 1.1): from financial or environmental problems, up to worse scenarios such as a big dam failure in a densely populated area, or the breaking of a nuclear power plant.

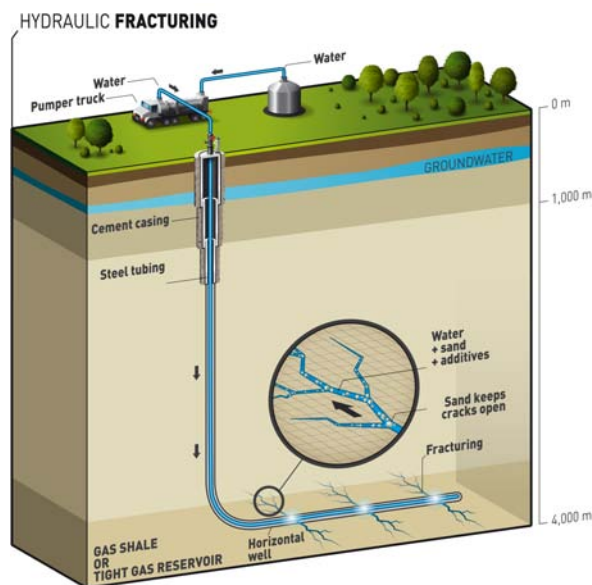


Figure 1.1: On November 12<sup>th</sup> 2001, the American Airlines Flight 587 crashed shortly after takeoff because of a tail structure failure while encountering wake turbulence.

Porous materials consist of a solid skeleton including interconnected networks of pores

that can be filled with air (void) or with fluid at the gas or liquid phase.

Understanding the behavior of these materials and their fracturing and failing mechanisms, together with the fluid redistribution, is now leading to new technological challenges. Applications can be found, for instance, in Oil&Gas, Civil and Biomedical engineering problems.



(a) A schematic representation of the extraction of shale or tight gas [1]. A mixture of water, sand, and chemicals are pumped into a shale/sandstone layer under high pressures. Hydraulic fracturing occurs and shale/tight gas flows out of the small fissures that were created.

(b) Aerial picture shows giant cracks at the base of Campos Novos concrete gravity Dam (Brazil).

Figure 1.2: Two examples about the importance of fractures in porous materials.

In Oil&Gas engineering, hydraulic fracturing (sometimes referred to as ‘fracking’) is the process of pumping water underground, mixed with a small proportion of sand and chemicals, at a high enough pressure to create small cracks in the rock (see Figure 1.2a). Unconventional gas is located in rocks with extremely low permeability such

as shale or sandstone, which makes extracting it more difficult. These cracks help to release the unconventional natural gas that would otherwise not be accessible. The International Energy Agency (IEA) predicts that the global industrial energy demand will increase by almost 40% up to 2035 [52], and natural gas will meet around 26% of total global energy demand by the same year [2]. In Civil engineering, an application of importance is related to the overtopping stability analysis of dams [88] (see Figure 1.2b). In Biomedical engineering, instead, applications can be found in the intervertebral disc herniation. A herniated disc occurs when the annulus fibrosus breaks open due to the propagation of a crack [55].

Thus, poroelastic models able to predict fractures could give more details about those kind of processes.

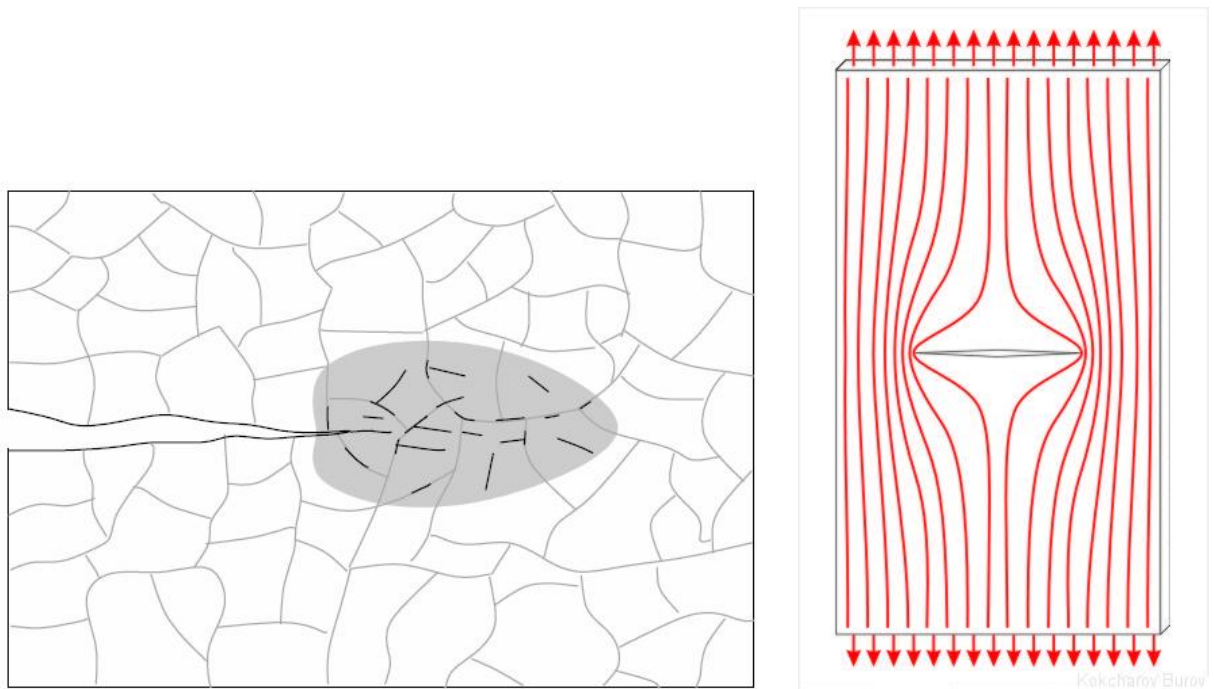
## 1.1: Physical behavior of fractures

Fractures can be seen as a complex succession of different mechanical events. The first event in fracture propagation of an existing crack is the *nucleation* of the micro-separations in a small area, called process zone, see Figure 1.3a.

The process zone consists of a small damage area, ahead of the growth of the macro-cracks, in which micro-separations and crack-bridging (i.e. fibers running from one crack-surface to the other) take place. From a microscopic point of view, micro-separations are tiny cracks in the micro-structure of the material. The nucleation phenomenon of these cracks usually occurs in areas with specific features: the stresses are high, and the inter-atomic bonds are sufficiently weak; this happens close to material inhomogeneities such as a cavity, or around phase boundaries like an existing crack or a notch (Figure 1.3b). Another possibility for the crack to nucleate is at imperfections on the free surfaces of specimens, because these locations are generally favorable to stress corrosion cracking and fatigue failure (e.g. crystalline solids).

The nucleation process corresponds to a energy dissipation, through friction (production of heat) and plastic permanent deformation (of the surrounding bulk material). This means that the step is irreversible, reducing the stiffness and the strength of the material also when the applied loads are removed. On the other hand, whenever the

---



(a) A simplified representation of the process zone (shade area) with micro-separations ahead of an existing crack in a granular material [76].

(b) Internal force field in a continuum, with an existing crack, under extension. The concentration of the internal force is higher near the crack tips.

Figure 1.3: Micro-separations and force lines lines around an existing crack.

applied loads are increased, a growth and a melting of the micro-cracks can be seen. At this point larger growths and defects can be visible with the naked eye, without using specific equipment. Moreover, these kinds of bigger defects give rise to higher stress concentrations in the material that, combined with a reduction of strength and stiffness, can lead to the total failure of the structure.

The evolution processes from micro-separations to final failure are different for each material [20]. Analyzing the behavior of two materials commonly used in civil engineering (i.e. concrete and steel), from the structural macroscopic level of observation, it can be said that concrete acts like a heterogeneous material, instead steel does not. In fact, concrete is characterized by differences in strength and stiffness of the two main

ingredients (i.e. cement paste, and aggregates of different shapes and dimensions) while steel can be considered as a homogeneous material. As a result, in concrete there are many possible sources for nucleation of micro-separations, also because of the initial drying shrinkage [18], instead in steel, where also the atomic structure is more regular than in the previous material, the final crack, if it exists, can be very sharp. It can be concluded that the process zone in concrete is wider than in steel, and also the final crack pattern is more spread in heterogeneous materials [102].

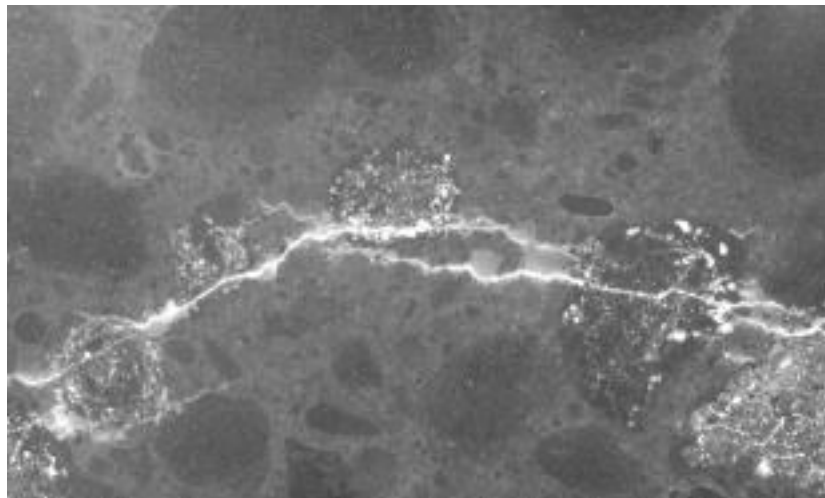


Figure 1.4: Diffuse crack pattern in concrete (Van Mier 1997).

Finally, fracture processes can be influenced by loading conditions (e.g. cyclic loadings that lead to fatigue fracture) and by environmental conditions (e.g. salt water can accelerate the fracture evolution in metals by means of a process called “stress-corrosion”, or even temperature can lead to failure composite materials).

## 1.2: Fracture models

Nowadays, to model the fracture propagation in the process zone, it is usual to lump all the effects due to micro-separations into just one model that can guarantee to govern the propagation of the main crack, instead of paying attention to each single micro-separation. This model has to keep in consideration two important hypotheses

---

of fracturing processes: first, the stiffness and the strength of the material must be reduced in a realistic way; secondly, this reduction must be accompanied by a correct reduction of the internal energy of the material itself [76].

The first models on fractures propagation date back to almost one century ago. The first work about this topic is due to the English aeronautical engineer Griffith that was interested in explaining the failure in brittle materials and developed, during the World War I, a first theory in 1920 [38] that was mainly based on the theorem of minimum energy. Griffith assumed the crack like a discontinuity in a smooth displacement field, allowing it to go further over a certain length when the surface energy in the structure was equal to the energy needed in the process zone for micro-separations to nucleate and grow. Several years later, at the U.S. Naval Research Laboratory, a group working under Irwin extended Griffith's theory for ductile materials [47] by including small-scale yielding around the crack tip and by introducing the idea of stress intensity factors to quantify the stress nearby a crack tip. In 1968, Rice [80] gave a new generalization of the previous works to elastic-plastic solids. The combination of this application with the Finite Element Method (FEM) led to the so-called Linear Elastic Fracture Mechanics (LEFM) which represented the most advanced theory for simulating cracks growth. Even though this method gives important benefits, it also has three main drawbacks: first of all, the small-scale yielding assumption represents a limitation because it requires that the process zone is comparable with the geometrical dimensions of the crack or, at least, that the difference is relatively small; secondly, the LEFM method does not consider any kind of crack nucleation in an undamaged part of the material away from a flaw; the third reason is related with the numerical modeling, in fact the direction of the propagation is not truly implemented into the FEM model, which means that expensive computational remeshing techniques are required.

### **1.3: FEM for fracture propagation**

Many computational models are based on Finite Elements (FE). FE uses a grid and shape approximations to calculate the fields of interest. The factors that play a key-role and have to be considered in computational fracture mechanics are:

---



- model for bulk behavior
- method for including discontinuities in the FEM
- damage initiation or yield criterion
- damage evolution model or constitutive model for crack growth

There are two approaches to the numerical analysis of failure in media, continuum damage mechanics and fracture mechanics.

The coming of the FEM in computational engineering and science represented a turning point and marked the rise of deeply new techniques for simulating fracture propagation, generally denoted as nonlinear theories. The most important of them are divided into two branches: the smeared (or continuous) approach, and the discrete (or discontinuous) approach [76].

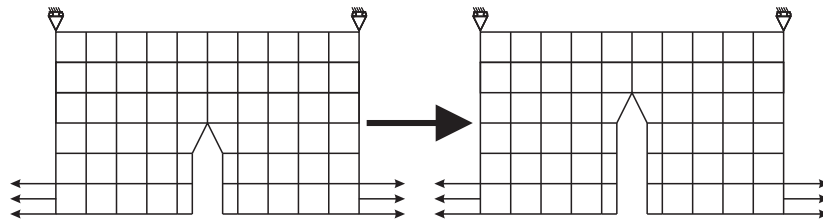


Figure 1.5: Early discrete crack modeling.

In the first approach, the displacement field is assumed to be continuous everywhere and cracks are introduced by deteriorating the stiffness and the strength of the material in the integration points of the the process zone. This means that in these models there is not a true introduction of a real crack (i.e. the displacement field is not discontinuous and there are no physical separations in the mesh). Hence, in these simulations there are large deformation gradients in the process zone, which eventually cause numerical problems to the algorithm [76]. Total failure can occur once the stiffness of the whole structure is equal to zero.

Furthermore, the band in the process zone, where the deformations are located, must have at least the maximum width available for each single element of the mesh.

---

This implies strict limitations for the applicability of this model to materials with quite narrow process zones. In order to avoid these problems the so-called Embedded Discontinuity Elements approaches have been developed [69, 15, 91]. In these methods, the large deformation gradients are taken into account as additional strain fields in the kinematic relations and the effects of displacement jumps to the finite elements are added as an incompatible mode strain. However, these methods lack robustness. Unfortunately, all the continuous models suffer from another important problem: since the entire structure is considered homogeneous, the models are not able to correctly describe the width of the process zone and, consequently, all damage is put in one single material point. Because of the nature of the problem, remediations like remeshing techniques are not useful for this purpose, but strategies named *regularisation models* [26], in which the strain term is usually extended with a higher order derivative (nonlocal strain), have been incorporated.

On the other hand, in the discrete approach, cracks are modeled as discontinuities in the displacement field. This method offers the advantage of its applicability also in materials in which process zones are narrow, compared to the structural dimensions. There are several discrete methods to introduce discontinuities in FEM: adaptive remeshing, interface elements or meshless methods [55]. In remeshing techniques, the mesh is continuously reconstructed in order to fit the discontinuity between the elements, this is why this method is classified as a geometrical approach. The problems related to adaptive remeshing are: difficulty in implementation and the computational complexity. From a numerical point of view, interface elements use elements of zero width that are fitted between the elements to model discontinuity and the nodes of the continuum elements are linked to the ones of the new elements. Interface modeling requires an a priori knowledge of the crack path, for the elements have to be aligned with it. Therefore the discontinuity is mesh dependent and a dummy stiffness has to be introduced in order to prevent the crack from debonding when it is not physical [27].

Finally, as a continuation of LEFM, in the 1960s, Dugdale and Barenblatt [33, 13] introduced the so-called cohesive zone approach, which is still considered a discrete

---

method. This tool represents the key to avoid the problem of limitation of LEFM due to the length of the process zone, in fact the cohesive zone also works when this restriction fails to hold.

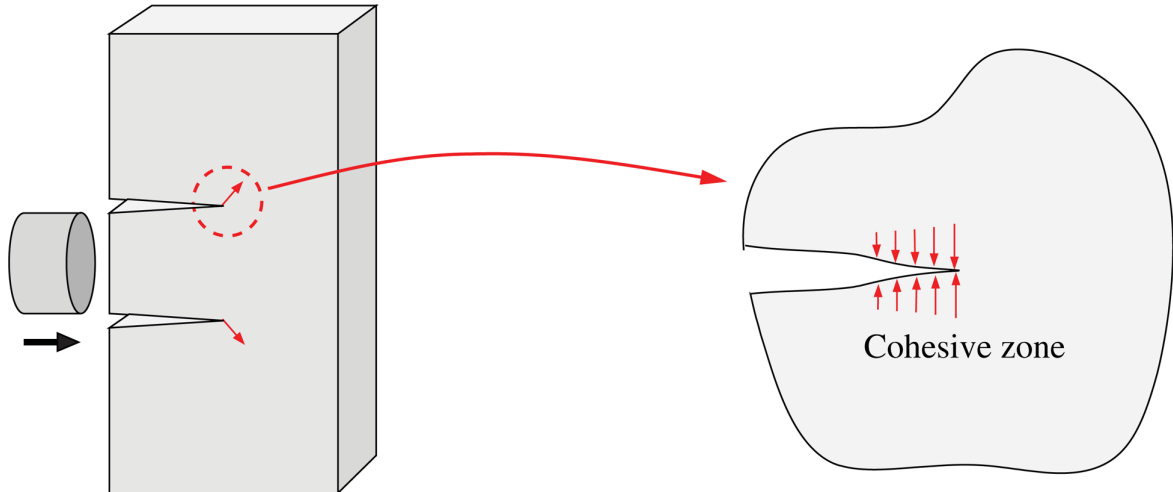


Figure 1.6: Schematic representation of the cohesive surface approach to fracture. The interface tractions that describe the perfect bond and debonding processes are represented in red.

Through this technique, as shown in Figure 1.6, the whole process zone is lumped into one single plane (or line) ahead of the existing fracture, which means that all the physical processes ahead of the tip are reduced to one equation. The nature of the work of the cohesive zone is such that the stress singularity in the tip of the crack is canceled; in other words, the traction forces are reduced to zero towards the crack-tip (Figure 1.7).

However, the actual shape of the cohesive zone is still a point of research [22, 101, 109]. Among the main advantages of this approach, it should be mentioned: firstly, the possibility that this method gives for capturing crack nucleation; secondly, the fact that it does not need the determination of the process zone's length, when the cohesive relation along the surface is specified. Moreover, a constitutive relation of the cohesive surface completely determines failure characteristics so that, together with balance laws, boundary conditions and constitutive relation for the bulk, it fully speci-

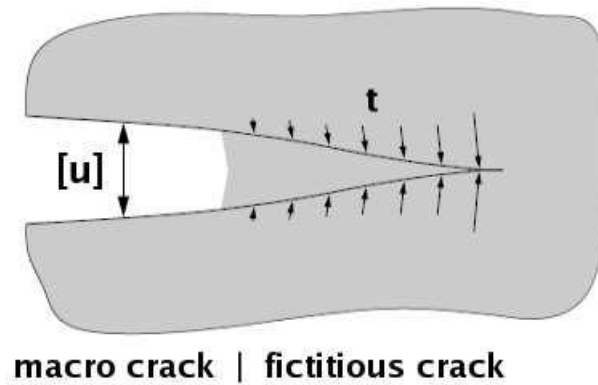


Figure 1.7: Close-up of a schematic representation of the cohesive zone. The opening of the surface is denoted as  $[u]$ .

fies the problem and fractures can grow up as a consequence of the deformation process without any additional failure criterion. Later on, this approach has been developed in different ways, e.g. by inserting cohesive constitutive relations at specified planes in the structure independently from the presence or not of a crack [67]. The simplest cohesive constitutive relation keeps in count the cohesive surface traction as a function of the displacement jump across that surface. For ductile fracture, the most relevant parameters are tensile strength and fracture energy [41] and from dimensional considerations, this introduces a characteristic length into the model. For brittle decohesion relations, the shape of the stress-separation relation plays a much larger role [82].

Several Authors [10, 85, 9] worked on the relation between cohesive surfaces and the finite element mesh, so that now it is conventional to incorporate them into the meshes using interface elements positioned between the standard continuum elements to model discontinuities. In order to simulate a perfect bond before cracking, a high dummy stiffness is introduced into the model and it is applied to the interface elements. When fracture takes place along well defined interfaces and when the crack path is already known a priori (i.e. from experiments), interface elements can be placed along the crack path in the mesh [83].

In 1994, Xu and Needleman [110] placed interface elements between all continuum elements in the finite mesh and they achieved the important goal of modeling complex fracture phenomena (e.g. crack branching or crack initiation away from the crack tip).

The drawback of placing interfaces between all continuum elements is that the process is not completely mesh independent, because the crack path is aligned with element boundaries. Moreover, a too weak dummy stiffness generates flexible results and, on the other side, a too strong dummy stiffness can cause numerical problems like traction oscillation at the cohesive surfaces [84, 27, 76].

In this Thesis, a discrete crack on Porous Media is modeled through elements based on the partition of unity property of finite element shape functions [63]. This approach, firstly proposed by Belytschko and other Authors in 1999 [14, 32], will be explained in the next Chapter. The main reasons for which this method is preferred, compared to the others, are listed below:

- discontinuities can be extended or added at any moment and in any direction
- the topology of the FE mesh is not modified
- no alignment between elements and crack path is required
- no dummy stiffness is needed
- relatively coarse meshes can be used
- cohesive constitutive models can be used

#### **1.4: Computational poroelastic fracturing models**

Starting from the 1960s, mathematical models have been developed to study the behavior of fractures, especially on Porous Media. This growing interest was mostly due to the massive use of hydraulic fracturing (also known as high-volume hydraulic fracturing, 1968) for recovering unconventional oil and gas economically from tight sandstone reservoirs in the U.S.

In fact, tight gas sands require advanced fracture technologies to be exploited efficiently and most of them have to be fractured before they flow at commercial rates. The main reason for such operations lies in the fact that this kind of rock is characterized by low permeability and low porosity.

---

Analytical solutions in the framework of LEFM have been obtained during past decades (e.g. [81, 40, 31]) but all of them were limited by the assumption of stationary problems and they were affected by strong simplifications (e.g. minimization of the exchange of fluid between soil and the crack tip). Moreover, fracture processes on porous media are preceded by a damage zone, therefore the materials are classified as quasi-brittle, and the models based on the LEFM cannot capture this nonlinear behavior in the process zone. The exact evolution of micro-damage to macro-cracks strongly depends on the material and its heterogeneity and initial defects. In 1990, Boone and Ingraffea [19] presented a general model of linear fracture mechanics, in which there was hydraulic driven fracture propagation in a porous medium. The model implemented a discrete fracture process using interface elements, so that the crack path is known a priori, neglecting fracture toughness (i.e. traction free) and the fluid was assumed to have a laminar flow and to be incompressible. Darcy's law was used to estimate the fluid flow from the crack into the structure by means of material permeability and water pressure gradient.

Schrefler *et al.*, and Secchi *et al.* [86, 90] proposed a method for simulating hydraulic fracture nucleation and propagation in poroelastic media using remeshing techniques. Thanks to the remeshing model, the fracture follows the face of the elements around the fracture tip which is closest to the normal direction of the maximum principal stress at the fracture tip. Thus, the direction of propagation is based on the principal stress. The Authors kept the same hypothesis concerning the fluid flow as Boone and Ingraffea, but the fluid is now considered compressible. One of the most relevant disadvantages in remeshing techniques is the requirement of a suitable algorithm to map nodal data between remeshing steps [55]. The work has been extended, in 2012, by the same Authors, to simulate hydraulically driven fractures in 3-D environments [88].

All these models present a traction-separation relation to model fracture processes, in which the cohesive law is able to capture the linear elastic behavior prior to fracture. Fracture processes can be generally divided into three main classes (see also Figure 1.8): mode I fracture (peel test; opening mode; a tensile stress normal to the plane of the crack), mode II fracture (shear; sliding mode; a shear stress acting parallel to the plane

---

of the crack and perpendicular to the crack front), mixed mode fracture (a combination of peel and shear; tearing mode; a shear stress acting parallel to the plane of the crack and parallel to the crack front).

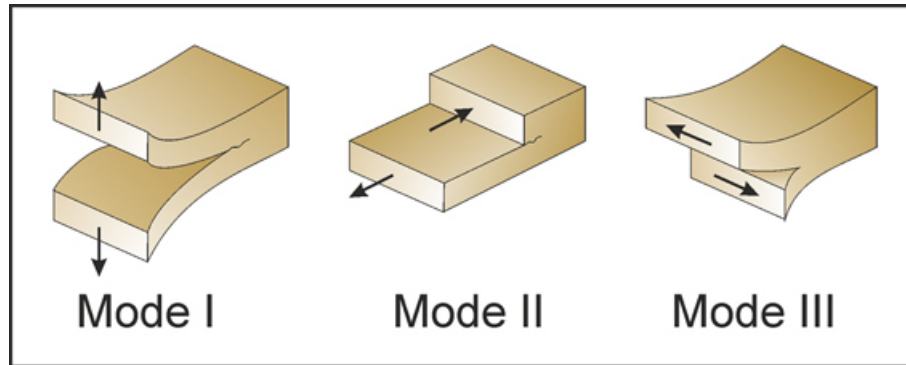


Figure 1.8: Crack modes used in modeling rock fractures in a reservoir. (Picture taken from [70]).

Interface elements in combination with remeshing techniques were used by Khoei *et al.* [53] for fracturing processes in saturated porous media. Moreover, they implemented a mixed mode cohesive model to represent the process zone considering dynamic conditions. The previous poroelastic models, in fact, considered quasi-static conditions. This implies the negligibility of inertial mass effects, while time cannot be neglected. In fact, in hydraulic fracturing processes the law of conservation of mass of the fluid is time-dependent.

R  thor  , De Borst *et al.* [28] were able to model shear banding in a porous material by means of the partition of unity method, where the fluid flow was considered by using Darcy’s law with constant permeability and gradient of pressures established from the pressure difference on both sides of the crack. Later on [78], a continuous description of pressures was used, the fluid flow was related to crack opening and a viscous Couette flow profile in the crack. However, this model does not consider crack propagation.

The partition of unity method was used by Remmers [76] and later on was also applied by Kraaijeveld [55] to simulate the behavior of crack propagations in ionized porous media, and by Remij [74] to simulate arbitrary crack propagation and nucleation in porous materials.

Recently, numerical simulations of crack propagation in porous materials, solids permeated by an interconnected network of pores filled with a fluid, for both mode I, tensile loading, and mode II, shear loading, of fracture mechanics, showed that the crack does not propagate smoothly inside the material, but has a stepwise pattern [55, 88, 89]. Moreover an experimental work confirms that mode I crack propagation in hydrogels is stepwise [71]. However, at the moment, there are no numerical projects aimed to investigate the stepwise advancement of fractures in porous media.

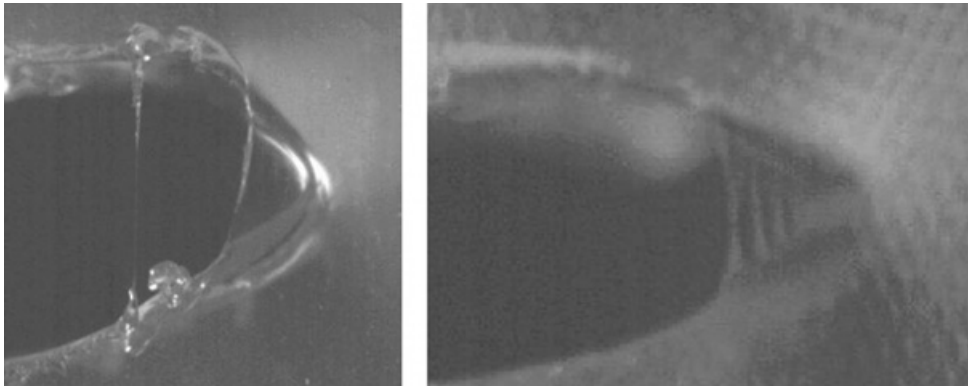


Figure 1.9: Two pictures of the physical stepwise crack propagation identified by Pizzocolo in hydrogels [71].

## 1.5: Research goal and lay-out of the thesis

In this work a poroelastic model that can simulate fracture nucleation and propagation using the partition of unity method is presented. In particular, attention is given to mode I fractures, to investigate the mesh independence of the model. Simulations are performed for several mesh sizes and the influence of materials and numerical parameters of the model are discussed. The utilization of the numerical model can also be extended for simulating multiple cracks in a continuum, but there are no examples in this Thesis. Firstly, the crack will be modeled in solid materials; secondly, in porous ones with identical loading conditions and by means of a continuous formulation for the porous phase.

---



The study on mesh independence may also give more insight in the investigation of stepwise behavior of fractures during fracturing processes and Hydraulic Fracturing operations on porous media. By means of the eXtended FEM (X-FEM) code of the Department of Mechanical Engineering of the Eindhoven University of Technology, the research aims to better understand if the stepwise progress of cracks, recently obtained through Numerical Simulations both with remeshing techniques and the Partition of Unity Method, in the research groups of the University of Padova and the Eindhoven University of Technology, corresponds to the physical behavior of fractures in materials or if it is a numerical artifact.

The *lay-out of the Thesis* will be as follows: in the next Chapter the X-FEM will be discussed from both a theoretical and analytical point of view: momentum and mass balance relations will be derived; the cohesive law used in this work will be described; a quasi-static model with small strain theory will be included as well as some remarks concerning the implementation of the model on the FE code. In the Third Chapter the main settings, the relevant parameters and the choices made for the simulations will be explained. In the Fourth Chapter the numerical results obtained during Mode-I fracturing processes will be presented and discussed. Recommendations for future works will be given. Finally, in the last Chapter, a conclusion will be drawn based on the numerical performances of the code.

---

## 2: The eXtended Finite Element Method (X-FEM)

In order to describe the fracture processes involved in this work, the partition of unity approach is used.

Mathematically speaking, discrete cracks are generally referred to as strong discontinuities, i.e. displacement jumps. However, the traditional FE models are suitable for those cases in which no prominent cracks can be recognized.

Therefore, an alternative way to introduce into the FEM fractures, consists on modeling them as discontinuities in the displacement fields by exploiting the partition of unity property of finite element shape functions. Hence, an approximation of the discontinuous field, independently of the underlying mesh, is used. Thus, no remeshing techniques are required, because the step in the displacement field is obtained by adding extra degrees of freedom into the already existing nodes.

PU-FEM and X-FEM were developed in the nineties and use enhancement functions to add discontinuities to the standard shape functions of the FE.

For in this work an eXtended Finite Element Method (X-FEM) formulation for 2D poroelastic media is presented, the fracture process zone is lumped into a single plane that is located ahead of the existing crack by using the cohesive zone modeling approach.

### 2.1: The problem of mesh dependence

Both continuous and discontinuous fracture models have the disadvantage to be limited because of the mesh size. The effects have been seen in several problems (e.g. numerical anomalies due to large deformations gradients [76]). In order to overcome these numerical anomalies, especially in the process zone, recent improvements in the field of numerical fracture mechanics have tried to shift the attention on new methods able to avoid mesh dependencies.

Camacho and Ortiz [22] were initially interested in avoiding finite element mesh problems in cohesive surface <sup>1</sup> models. Therefore they considered a rigid cohesive surface in

---

<sup>1</sup>Discontinuities or cracks are also referred to as cohesive surfaces

combination with a continuous adaptive mesh refinement so that whenever there was an exceeding of the maximum ultimate stress in the material, the algorithm created a new initially-rigid interface element in the FE mesh.

The remeshing technique replaced the intersected continuum elements. This approach is mainly based on a procedure commonly used in LEFM, like showed by Ingraffea and Saouma in 1985 [46]. Here, the fracture simulation is stopped every time the crack tip is propagated, in order to rebuild a new FE mesh. This operation requires a laborious process of reallocating the variables (e.g. local stresses) to the new material points in the FE mesh.

Subsequently, another path has been investigated, in which the cohesive surface is incorporated in the continuum elements. This was possible by means of using the partition of unity property of finite element shape functions [11] together with a discontinuous mode incorporated at the element level [65]. In this approach the cohesive zone is represented by using a jump in the displacement field of the continuum elements [105, 106, 64]. The partition of unity approach to cohesive fracture is commonly referred to as an application of the eXtended Finite Element Method (e.g. [29, 76, 77, 96]).

Even though the name seems to lead to the conclusion that the method consists on an extension of the FEM, this is not true. In fact, the X-FEM exploits a property of the standard FE shape functions that has not been acknowledged until Babuška and Melenk published, in 1997, their seminal paper [11]. Nevertheless, this specific partition of unity property has been used unintentionally previously in a certain number of publications (e.g. Goto *et al.* 1992 [37]).

Summarizing, whereas in previous research the cohesive zone model has generally been introduced either at all element boundaries [109] or in the path of interest [83, 85], the application of this method on discontinuity kinematics allows the crossing of continuum elements for the cohesive zone [64, 75, 104] and also the overcoming of the mesh dependence problem.

## 2.2: The X-FEM applied to cohesive fracture

In this section a concise overview of cohesive fracture models will be given, especially focusing the attention on the cohesive zone models applied in combination with X-FEM. In fact, X-FEM (or PU-FEM) are used to represent a discontinuity, instead the cohesive zone is used to represent a fracture.

The cohesive zone model represents a damage evolution. The evolution can be described as nonlinear springs (see Figure 2.1).

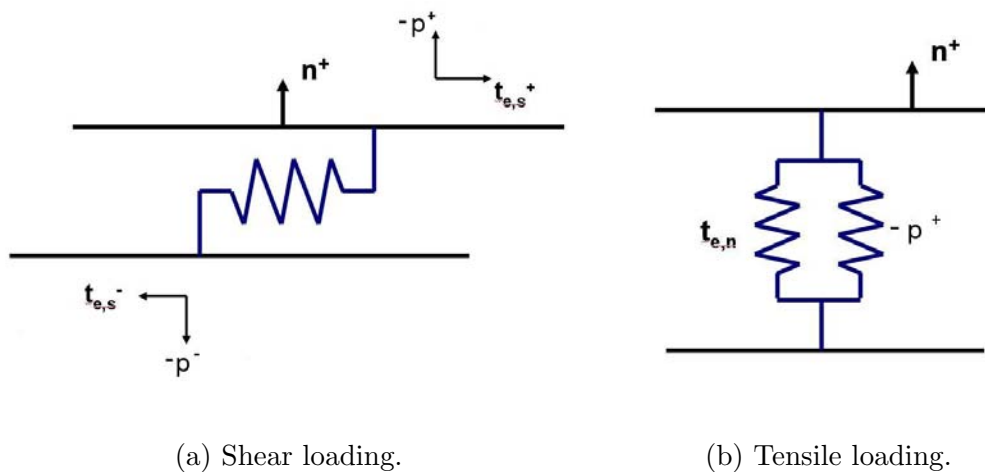


Figure 2.1: Traction forces at the discontinuity represented as (nonlinear) springs for **a.** Shear loading **b.** Tensile loading.

The idea of introducing a cohesive surface methodology [33, 13, 39] is a very useful technique to simulate fracture propagations in several engineering applications, especially in the field of material science. In fact, all the events, that eventually occur in the process zone, are lumped into one single surface ahead of the crack tip. From a mathematical point of view, the separation of this cohesive surface is regulated by an independent constitutive relation that is responsible for the fracturing process on the material.

In the past decades, a generalization of the methodology has been given [67]: this

configuration allowed to model crack nucleations away from an existing crack tip or void.

The cohesive surface can be considered as a discontinuity in the displacement field of the body [76], which is in direct conflict with the classical formulations of solid mechanics where, instead, a body is described by continuous and smooth displacements, stress and strain fields.

A FE domain, characterized by a spatial discretization, played a key role for the introduction of discontinuities. In the first models (e.g. Ngo and Scordelis, 1967 [68]) a jump in the displacement field was created by simply disconnecting two adjacent elements. In this way the relative displacement of the elements was a measure for the separation of the cohesive zone and the nodal forces at the disconnected elements were extrapolated from the tractions obtained through the cohesive constitutive equation.

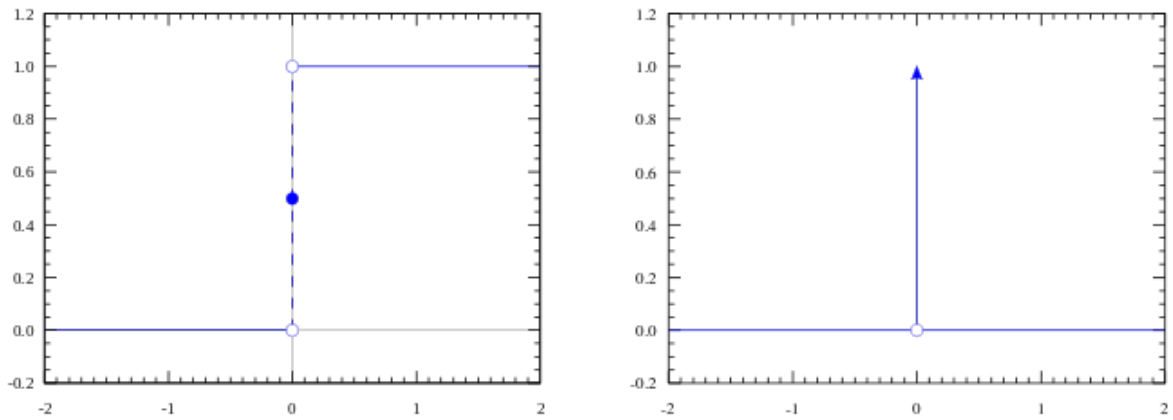
In the following years a more elegant method was introduced: instead of just disconnecting elements in FE model, several Authors [10, 84, 9] modeled cracks by using the so-called *interface elements*. These elements are made of two surfaces, connected to the adjacent continuum elements. Interface elements have been preferred to the previous ones, especially for those simulations in which big geometrical effects were expected (e.g. delamination buckling) because they offer the advantage of an adequate description of either relative displacement of the two surfaces and total rotation of the cohesive zone.

In order to avoid a mesh dependent model, generated by inserting the discontinuity after the discretization (i.e. the crack path is dependent to the FE mesh), the displacement jump can be incorporated in the analytical field of displacements before performing the discretization. The discontinuity is then part of the boundary value problem without changing the mechanical model.

The smartest way to introduce discontinuities on continuous and smooth fields is to insert another displacement field, on the top of the existing base field, multiplied with a *unit step function* [14]. A unit step function, usually referred to as *Heaviside function*, is a discontinuous function whose value is zero for negative argument and one for positive argument. It is used in structural mechanics, together with the Dirac delta

---

function, to describe different types of structural loads (see Figure 2.2).



(a) The Heaviside step function, using the half-maximum convention. The function is used in the mathematics of fracture mechanics theory to represent discontinuities on a continuous displacement field.

(b) The Dirac delta function represented by a line surmounted by an arrow. The height of the arrow is usually used to specify the value of any multiplicative constant, which will give the area under the function.

Figure 2.2: Schematic representation of the Heaviside step function and of the Dirac delta function.

Here, the Heaviside function is equal to zero on one side of the discontinuity, one on the other side, so that the final amplitude of the displacement jump is equal to the amplitude of the second added displacement field exactly at the discontinuity.

Hence, the discontinuous displacement field can be transformed into a discretized field by exploiting the partition of unity property of FE shape functions [11]. By means of an extra set of degrees of freedom, added to the existing nodes of the FE mesh, the additional displacement field is represented. The use of these enhanced functions makes the preservation of the continuity along the crack possible. This method has been recently extended in cohesive surface formulations [105, 64] after a period in which it was used for LEFM simulations.

### 2.2.1: Advantages of the X-FEM applied to cohesive fracture

The partition of unity approach to cohesive fracture presents a number of advantages over conventional models.

One of the great advantages of this method lies in the fact that discontinuities can be extended or added in any moment, in arbitrary directions and anywhere in the model, during simulations just by adding new additional degrees of freedom irrespective of the structure of the underlying FE mesh (e.g. Figure 2.3 taken from Wells *et al.* [105]).

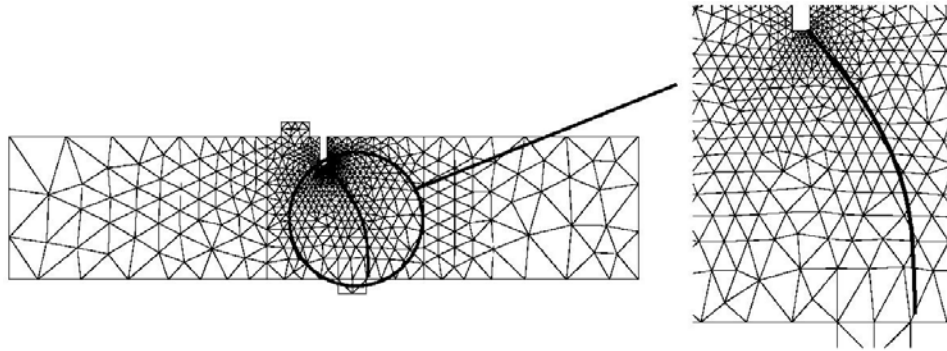


Figure 2.3: Crack growth in a single edge notched beam, simulated with the partition of unity approach to cohesive fracture. The cohesive surface (bold line) crosses the continuum elements (Wells and Sluys 2001).

Another great advantage, for instance over remeshing techniques, highlighted by Camacho and Ortiz [22], is that the topology of the FE mesh is not modified. The amount of nodes and elements remains therefore the same, as well as their mutual connectivity, which means that the discontinuity is projected on the element by additional degrees of freedom and not nodes.

Furthermore, no alignment between elements and crack path is required, no dummy stiffness is needed and a standard discretization is used. Avoiding the use of high dummy stiffnesses, numerical problems such as spurious stress oscillations [84] or stress wave reflections in dynamic simulations [76] are prevented.

Another benefit related to this method is also that relatively coarse meshes can

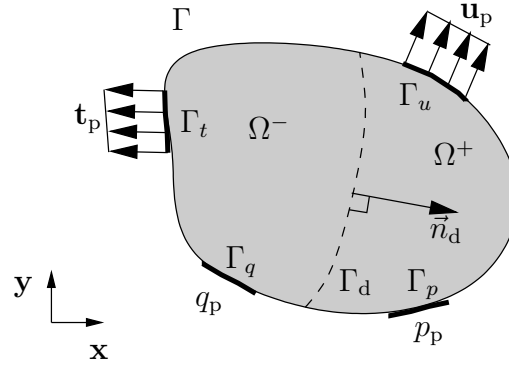


Figure 2.4: The body  $\Omega$  crossed by discontinuity  $\Gamma_d$ . The body is completed with the boundary conditions.

be used, even if it has to be said that the method is not easy to be implemented in commercial codes.

Finally, since this methodology is based on an existing cohesive surface formulation, existing cohesive constitutive models can still be used.

## 2.3: Analytical solutions

Following the work by Wells *et al.* (2001-2002), analytical formulations for the X-FEM applied to cohesive surfaces problems are given in the next subsections. In particular, the principal equations that govern the problem of this Thesis will be derived.

### 2.3.1: Kinematic relations

Consider a domain  $\Omega$  with boundary  $\Gamma$  as shown in Figure 2.4. The domain is crossed by discontinuity  $\Gamma_d$  and divided in two domains,  $\Omega^+$  and  $\Omega^-$ . The normal  $\mathbf{n}_d$  of the discontinuity is directed towards the domain  $\Omega^+$ . The total displacement field  $\mathbf{u}(\mathbf{x}, t)$  is decomposed into two parts: a continuous regular field  $\hat{\mathbf{u}}(\mathbf{x}, t)$  and an additional discontinuous enhanced displacement field  $\tilde{\mathbf{u}}(\mathbf{x}, t)$  [105]:

$$\mathbf{u}(\mathbf{x}, t) = \hat{\mathbf{u}}(\mathbf{x}, t) + \mathcal{H}_{\Gamma_d}(\mathbf{x})\tilde{\mathbf{u}}(\mathbf{x}, t) \quad (2.1)$$



where  $\mathbf{x}$  is the position of the material point in the body  $\Omega$ ,  $t$  is the time and  $\mathcal{H}_{\Gamma_d}$  is a step function which is constant and defined in each side of a discontinuity:

$$\mathcal{H}_{\Gamma_d} = \begin{cases} \mathcal{H}^+ & \text{if } \mathbf{x} \in \Omega^+ \\ \mathcal{H}^- & \text{if } \mathbf{x} \in \Omega^- \end{cases} \quad (2.2)$$

The step  $h$  is defined as the magnitude of the following function:

$$h = \mathcal{H}^+ + \mathcal{H}^- \quad (2.3)$$

Wells and Sluys [105] used a standard Heaviside step function to describe the jump:

$$\mathcal{H}_{\Gamma_d} = \begin{cases} 1 & \text{if } \mathbf{x} \in \Omega^+ \\ 0 & \text{if } \mathbf{x} \in \Omega^- \end{cases} \quad (2.4)$$

But also other functions have been used in the past years (e.g. Réthoré *et al.* [79]).

The model assumes a small strain formulation and the strain field can be calculated by taking the derivative displacement field (2.1) with respect to the position in the body  $x$ :

$$\boldsymbol{\epsilon}(\mathbf{x}, t) = \nabla^s \hat{\mathbf{u}}(\mathbf{x}, t) + \mathcal{H}_{\Gamma_d} \nabla^s \tilde{\mathbf{u}}(\mathbf{x}, t) \quad \mathbf{x} \notin \Gamma_d \quad (2.5)$$

where  $\nabla^s$  is the symmetric differential operator:

$$\nabla^s \mathbf{u} = \frac{1}{2}(\nabla \mathbf{u} + (\nabla \mathbf{u})^T) \quad (2.6)$$

The displacement jump is not uniquely defined at the discontinuity, hence the corresponding strain field is unbounded. Therefore the magnitude of the displacement jump  $[\mathbf{u}(\mathbf{x}, t)]_d$  at the discontinuity  $\Gamma_d$  is representing the opening of the crack and it is given by:

$$[\mathbf{u}(\mathbf{x}, t)]_d = h \tilde{\mathbf{u}}(\mathbf{x}, t) \quad \mathbf{x} \in \Gamma_d \quad (2.7)$$

The pressure in the domain  $\Omega$  is assumed to be discontinuous as well. Pressure values inside the discontinuity are different from the ones in the surrounding formation. The gradient of this difference quantifies the interaction of fluid flow between the fracture and the formation. By enhancing the pressure field with a signed distance function like in previous works (e.g. Réthoré *et al.* 2007, [78]), the gradient near a discontinuity is taken into account in a natural way:

$$p(\mathbf{x}, t) = \hat{p}(\mathbf{x}, t) + \mathcal{D}_{\Gamma_d}(\mathbf{x})\tilde{p}(\mathbf{x}, t) \quad (2.8)$$

in which the distance function  $\mathcal{D}_{\Gamma_d}(\mathbf{x})$  is defined:

$$\mathcal{D}_{\Gamma_d}(\mathbf{x}) = |(\mathbf{x} - \mathbf{x}_{\Gamma_d}) \cdot \mathbf{n}_d| \quad \mathbf{x} \in \Omega \quad (2.9)$$

Here,  $\mathbf{x}_{\Gamma_d}$  represents the coordinate of the nearest point on the discontinuity and  $\mathbf{n}_d$  is the corresponding normal vector. The pressure gradient flow follows from the spatial derivative of the pressure field (2.8):

$$\nabla p(\mathbf{x}) = \nabla \hat{p}(\mathbf{x}) + \mathcal{D}_{\Gamma_d}(\mathbf{x})\nabla \tilde{p}(\mathbf{x}) + \nabla \mathcal{D}_{\Gamma_d}(\mathbf{x})\tilde{p}(\mathbf{x}) \quad (2.10)$$

where the gradient of the distance function  $\mathcal{D}_{\Gamma_d}$  is:

$$\nabla \mathcal{D}_{\Gamma_d}(\mathbf{x}) = \begin{cases} \mathbf{n}_d & \text{if } \mathbf{x} \in \Omega^+ \\ -\mathbf{n}_d & \text{if } \mathbf{x} \in \Omega^- \end{cases} \quad (2.11)$$

### 2.3.2: Balance equations

The whole system can be described by using two balance equations: the balance of linear momentum and the mass balance. In this section, the weak forms of the two balance equations are derived for both the bulk material and the interface. The skeleton is assumed to be incompressible and linear elastic. The permeability is assumed to be isotropic and constant.

---

### 2.3.2.1: Linear momentum balance

The porous skeleton is considered to be fully saturated with a fluid. It is assumed that there is no mass transfer between the two constituents. The process is quasi-static and isothermal. Gravity, inertia and convection are neglected. The momentum balance for constituent  $\chi$  is than [28]:

$$\nabla \cdot \boldsymbol{\sigma}_\chi + \hat{\mathbf{m}}_\chi = \mathbf{0} \quad (2.12)$$

where  $\boldsymbol{\sigma}$  is the total stress tensor and  $\hat{\mathbf{m}}$  is the source momentum. The constituents  $\chi$  are the solid and the fluid respectively notated as  $\chi_s$  and  $\chi_f$ . The momentum balance states that:

$$\sum_{\chi=s,f} \hat{\mathbf{m}}_\chi = \mathbf{0} \quad (2.13)$$

With these assumptions the linear momentum balance reads, e.g. [28, 56, 58]:

$$\nabla \cdot \boldsymbol{\sigma} = \mathbf{0} \quad (2.14)$$

with:

$$\boldsymbol{\sigma} = \boldsymbol{\sigma}_s + \boldsymbol{\sigma}_f = \boldsymbol{\sigma}_s - \alpha p \mathbf{I} = \boldsymbol{\sigma}_e - \alpha p \mathbf{I} \quad (2.15)$$

where  $\boldsymbol{\sigma}$  can be decomposed in Terzaghi's effective stress  $\boldsymbol{\sigma}_e$ , the hydrostatic pressure  $p$ ,  $\mathbf{I}$  is the unit matrix and  $\alpha$  the Biot effective stress coefficient [28].

Biot's effective stress coefficient is given by:

$$\alpha = 1 - \frac{K_t}{K_s} \quad (2.16)$$

here  $K_t$  is the bulk modulus of the porous medium and  $K_s$  is the bulk modulus of the solid grains. The solid grains are assumed to be incompressible and thus  $\alpha = 1$ .

In the small strain theory the effective stress is described with a linear stress-strain

relation:

$$\boldsymbol{\sigma}_e = 2\mu\boldsymbol{\epsilon} + \lambda \text{tr}(\boldsymbol{\epsilon})\mathbf{I} \quad (2.17)$$

where the strain tensor  $\boldsymbol{\epsilon}$  has been defined in (2.5) and  $\mu$  and  $\lambda$  are respectively the first and second Lamé constants. In an isotropic material, like the one used in this Thesis, these are defined as:

$$\mu = \frac{E}{2(1+\nu)} \quad \lambda = \frac{\nu E}{(1+\nu)(1-2\nu)} \quad (2.18)$$

with  $E$  and  $\nu$  being the Young's modulus and the Poisson's ratio, respectively.

Generally, (2.14) is also written as:

$$\boldsymbol{\sigma} = \boldsymbol{\sigma}_e - p\mathbf{I} \quad (2.19)$$

neglecting the Biot effective stress coefficient.

The effective stress  $\boldsymbol{\sigma}_e$  is related to the strains  $\boldsymbol{\epsilon}$  which have been defined in (2.5) by means of a linear elastic constitutive law. In rate form, this Hooke's law reads:

$$\dot{\boldsymbol{\sigma}}_e = \mathbf{C}\dot{\boldsymbol{\epsilon}} \quad (2.20)$$

The momentum balance is completed with the following boundary conditions:

$$\begin{aligned} \boldsymbol{\sigma} \cdot \mathbf{n}_\Gamma &= \mathbf{t}_p(\mathbf{x}, t) & \mathbf{x} \in \Gamma_t \\ \mathbf{u}(\mathbf{x}, t) &= \mathbf{u}_p(\mathbf{x}, t) & \mathbf{x} \in \Gamma_u \end{aligned} \quad (2.21)$$

with  $\Gamma_t \cup \Gamma_u = \Gamma$ ,  $\Gamma_t \cap \Gamma_u = \emptyset$ .

### 2.3.2.2: Mass balance

Under equal assumptions as made for the momentum balance, the mass balance is written as [28]:

$$\frac{\delta \rho_\chi}{\delta t} + \nabla \cdot (\rho_\chi \mathbf{v}_\chi) = 0 \quad (2.22)$$

where  $\rho_\chi$  is the mass density and  $\mathbf{v}_\chi$  is the absolute velocity. A fully saturated medium is considered, which means:

$$n^f + n^s = 1 \quad (2.23)$$

where  $n^f = \frac{V^f}{V}$  and  $n^s = \frac{V^s}{V}$  are the volume fractions. Under the assumption of incompressible constituents equation (2.22) can be written as [28, 78]:

$$\nabla \cdot \mathbf{v}_s + \nabla \cdot n^f (\mathbf{v}_f - \mathbf{v}_s) = 0 \quad (2.24)$$

In equation (2.24) the last term represents the seepage flux:

$$\mathbf{q} = n^f (\mathbf{v}_f - \mathbf{v}_s) \quad (2.25)$$

Generally, the mass balance with an incompressible fluid assumption, is also written in a smoother way [28]:

$$\nabla \cdot \mathbf{v}_s + \nabla \cdot \mathbf{q} = 0 \quad (2.26)$$

where  $\mathbf{v}_s$  is the deformation velocity of the solid skeleton and  $\mathbf{q}$  is related to the pressure gradient by means of Darcy's law [55]. Darcy's relation is assumed to hold for the fluid flow in the bulk material [17]:

$$\mathbf{q} = -\mathbf{K} \cdot \nabla p \quad (2.27)$$

where  $\mathbf{K}$  is the permeability tensor, which is assumed to be constant in time and space [56]. In the case of an isotropic material, the permeability is equal to  $\mathbf{K} = KI$ .

---

The mass balance is supported by the following boundary conditions:

$$\begin{aligned} \mathbf{q}(\mathbf{x}, t) \cdot \mathbf{n}_\Gamma &= q_p & \mathbf{x} \in \Gamma_q \\ p(\mathbf{x}, t) &= p_p & \mathbf{x} \in \Gamma_p \end{aligned} \quad (2.28)$$

with  $\Gamma_q \cup \Gamma_p = \Gamma$ ,  $\Gamma_q \cap \Gamma_p = \emptyset$ .

### 2.3.2.3: Local constitutive behavior

The governing equations are completed by momentum and mass balance at the fracture surface. There is a need of coupling the discontinuity and the surrounding porous medium in the balance equations. Momentum and balance equations are coupled respectively by traction in the discontinuity and a fluid flow through the discontinuity.

In accordance with the cohesive zone approach, the softening of the material is governed by a traction acting on the discontinuity surface. The relation between the traction and the opening displacement is defined with a cohesive law. This traction is coupled to the hydrostatic pressure in the crack [29]. Assuming continuity of stress from the formation to the fracture, the local momentum balance can be written as:

$$\boldsymbol{\sigma} \cdot \mathbf{n}_d = \mathbf{t}_d - p_d \mathbf{n}_d \quad (2.29)$$

where  $\mathbf{t}_d$  is the cohesive traction relating the opening of the crack with crack softening,  $\mathbf{n}_d$  is the normal of the crack surface directed into the body and  $p_d$  is the hydrostatic pressure in the discontinuity:

$$p_d = p(\mathbf{x} \in \Gamma_d) \quad (2.30)$$

In order to describe the local mass balance, assumptions on how the fluid flow takes place are needed. In particular, referring to mode I loading, the one used in this Thesis, fluid flow is dependent on the crack rate opening and the tangential flow into the crack. Réthoré *et al.* [29, 78] coupled the fluid flow to the opening rate of the crack and the local mass balance, based on Couette flow, in the crack. The disadvantage of

---

this approach is that a second order derivative is needed to describe the local fluid flow. In this work, Couette flow is considered, also considering different damage models for the cohesive zone permeability. Fluid flow is assumed to only depend on the opening rate of the crack. In the description of the local mass balance it is not considered the tangential fluid flow in the fracture. Mass balance is therefore an equilibrium of fluid exchange between the formation and the fracture, and of the opening rate of the fracture. Integrating the local mass balance, this reads:

$$\mathbf{q}_{\Gamma_d}^+ \cdot \mathbf{n}_d - \mathbf{q}_{\Gamma_d}^- \cdot \mathbf{n}_d + [\dot{\mathbf{u}}]_n - u_n \frac{\delta}{\delta s} (k_d \frac{\delta p_d}{\delta s}) \quad (2.31)$$

with  $\mathbf{q}_{\Gamma_d}^+$  and  $\mathbf{q}_{\Gamma_d}^-$  being the fluid flow from the fracture into formation for the fracture side of the  $\Omega^+$  and the  $\Omega^-$  domain respectively,  $[\dot{\mathbf{u}}]_n$  denoting the time derivative of the normal opening of the fracture,  $u_n$  being the opening in the fracture and  $k_d$  being the permeability in the fracture. In Equation (2.31), under the assumption of small deformations, the normal vectors of the two fracture lips in opposite direction are used. Assuming a Couette flow, the permeability is given by:

$$k_d = \frac{u_n^2}{12\mu} \quad (2.32)$$

where  $\mu$  is the dynamic viscosity of the fluid. The derivation of this equation can be found in Irzal *et al.* 2013, [48].

### 2.3.3: Weak form

Weak formulation is an important tool for the analysis of mathematical equations that allow the transfer of concepts of linear algebra to solve problems in other fields (e.g. partial differential equations). In a weak formulation, an equation is no longer required to hold absolutely (and this is not even necessarily well defined) and has instead weak solutions only with respect to certain “test vectors” or “test functions”.

The weak form of the balance equation is obtained by multiplying Equations (2.14) and (2.26) with admissible test functions for the displacement and pressure field.

These functions are called  $\boldsymbol{\eta}$  and  $\zeta$ , respectively, and have the same form as the

original fields:

$$\begin{aligned}\boldsymbol{\eta} &= \hat{\boldsymbol{\eta}} + \mathcal{H}_{\Gamma_d} \tilde{\boldsymbol{\eta}} \\ \zeta &= \hat{\zeta} + \mathcal{D}_{\Gamma_d} \tilde{\zeta}\end{aligned}\tag{2.33}$$

This means that they can be decomposed in a regular part and in an enhanced part.

The weak form of the momentum balance (2.14), using the divergence theorem, is:

$$\int_{\Omega} \boldsymbol{\eta} \cdot (\nabla \cdot \boldsymbol{\sigma}) d\Omega = 0\tag{2.34}$$

Substituting the variations into Equations (2.14) and (2.26), applying Gauss' theorem, using the symmetry of the Cauchy stress tensor, introducing the internal boundary  $\Gamma_d$  and the corresponding admissible displacement jump and using the boundary conditions at the external boundaries  $\Gamma_t$  and  $\Gamma_q$  it gives:

$$\begin{aligned}\int_{\Omega} \nabla \hat{\boldsymbol{\eta}} : \boldsymbol{\sigma} d\Omega + \int_{\Omega} \mathcal{H}_{\Gamma_d} \nabla \tilde{\boldsymbol{\eta}} : \boldsymbol{\sigma} d\Omega = \\ \int_{\Gamma_t} \hat{\boldsymbol{\eta}} \cdot \mathbf{t}_p d\Gamma_t + \int_{\Gamma_t} \mathcal{H}_{\Gamma_d} \tilde{\boldsymbol{\eta}} \cdot \mathbf{t}_p d\Gamma_t - \int_{\Gamma_d} \tilde{\boldsymbol{\eta}} \cdot (\boldsymbol{\sigma} \cdot \mathbf{n}_d) d\Gamma_d\end{aligned}\tag{2.35}$$

$$\begin{aligned}- \int_{\Omega} \hat{\zeta} \nabla \cdot \mathbf{v}_s d\Omega - \int_{\Omega} \mathcal{D}_{\Gamma_d} \tilde{\zeta} \nabla \cdot \mathbf{v}_s d\Omega + \int_{\Omega} \nabla(\hat{\zeta}) \cdot \mathbf{q} d\Omega \\ + \int_{\Omega} \nabla(\mathcal{D}_{\Gamma_d} \tilde{\zeta}) \cdot \mathbf{q} d\Omega = \\ \int_{\Gamma_q} \hat{\zeta} \mathbf{q}_p d\Gamma_q + \int_{\Gamma_q} \mathcal{D}_{\Gamma_d} \tilde{\zeta} \mathbf{q}_p d\Gamma_q - \int_{\Gamma_d} \hat{\zeta} \mathbf{q}_{\Gamma_d}^+ \cdot \mathbf{n}_d d\Gamma + \int_{\Gamma_d} \hat{\zeta} \mathbf{q}_{\Gamma_d}^- \cdot \mathbf{n}_d d\Gamma\end{aligned}\tag{2.36}$$

In these equations,  $\mathbf{t}_p$  and  $\mathbf{q}_p$  are the prescribed traction and prescribed fluid outflow boundary conditions, respectively, (Figure 2.4) and  $\Gamma_d$  represents the integral over the internal boundary of the discontinuity. The terms  $\boldsymbol{\sigma} \cdot \mathbf{n}_d$ ,  $\mathbf{q}_{\Gamma_d}^+ \cdot \mathbf{n}_d$  and  $\mathbf{q}_{\Gamma_d}^- \cdot \mathbf{n}_d$  are given by the balance Equations at the discontinuity (2.29) and (2.31). By taking one of the admissible variations  $\delta \hat{\boldsymbol{\eta}}$ ,  $\delta \tilde{\boldsymbol{\eta}}$ ,  $\delta \hat{\zeta}$  and  $\delta \tilde{\zeta}$  at the time, the weak form of equilibrium

---



can be separated into four sets of equations that can be called: continuous momentum balance ( $\tilde{\boldsymbol{\eta}} = 0$ ), discontinuous momentum balance ( $\hat{\boldsymbol{\eta}} = 0$ ), continuous mass balance ( $\hat{\zeta} = 0$ ), discontinuous mass balance ( $\tilde{\zeta} = 0$ ). A detailed theoretical description is given in [78, 105].

### 2.3.3.1: Continuous momentum balance $\tilde{\boldsymbol{\eta}} = 0$

$$\int_{\Omega} (\nabla \hat{\boldsymbol{\eta}}) : \boldsymbol{\sigma} d\Omega = \int_{\Gamma_t} \hat{\boldsymbol{\eta}} \cdot \boldsymbol{t}_t d\Gamma - \int_{\Gamma_d^+} \hat{\boldsymbol{\eta}} \cdot (\boldsymbol{\sigma} \cdot \boldsymbol{n}^+) d\Gamma - \int_{\Gamma_d^-} \hat{\boldsymbol{\eta}} \cdot (\boldsymbol{\sigma} \cdot \boldsymbol{n}^-) d\Gamma \quad (2.37)$$

The last two terms describe the traction on the discontinuity. The cohesive traction  $t_d$  and the pressure are equal one to the other at the two opposite crack surfaces. The two total stresses are thus equal in sign but directed in opposite direction. This leads to the following continuous momentum equation:

$$\int_{\Omega} (\nabla \hat{\boldsymbol{\eta}}) : \boldsymbol{\sigma} d\Omega = \int_{\Gamma_t} \hat{\boldsymbol{\eta}} \cdot \boldsymbol{t}_t d\Gamma \quad (2.38)$$

### 2.3.3.2: Discontinuous momentum balance $\hat{\boldsymbol{\eta}} = 0$

The momentum balance for the discontinuous part as follows:

$$\int_{\Omega} \mathcal{H}_{\Gamma_d} \nabla \tilde{\boldsymbol{\eta}} : \boldsymbol{\sigma} d\Omega = \int_{\Gamma_t} (\mathcal{H}_{\Gamma_d} \tilde{\boldsymbol{\eta}}) \cdot \boldsymbol{t}_t d\Gamma - \int_{\Gamma_d^+} (\mathcal{H}_{\Gamma_d} \tilde{\boldsymbol{\eta}}) \cdot (\boldsymbol{\sigma} \cdot \boldsymbol{n}^+) d\Gamma - \int_{\Gamma_d^-} (\mathcal{H}_{\Gamma_d} \tilde{\boldsymbol{\eta}}) \cdot (\boldsymbol{\sigma} \cdot \boldsymbol{n}^-) d\Gamma \quad (2.39)$$

The last two integrals can be simplified by using the momentum balance on the discontinuity ( $\boldsymbol{\sigma} \cdot \boldsymbol{n}^+ = t_d - \mu_f \boldsymbol{n}^+$ ) and filling in the Heaviside function (2.2):

$$- \int_{\Gamma_d^+} (\mathcal{H}_{\Gamma_d} \tilde{\boldsymbol{\eta}}) \cdot (\boldsymbol{\sigma} \cdot \boldsymbol{n}^+) d\Gamma - \int_{\Gamma_d^-} (\mathcal{H}_{\Gamma_d} \tilde{\boldsymbol{\eta}}) \cdot (\boldsymbol{\sigma} \cdot \boldsymbol{n}^-) d\Gamma = - \int_{\Gamma_d^+} h \tilde{\boldsymbol{\eta}} \cdot (t_d - p \boldsymbol{n}^+) d\Gamma \quad (2.40)$$

Substituting this into the momentum equation, the momentum equation for the dis-

continuous part is reached:

$$\int_{\Omega} \mathcal{H}_{\Gamma_d} \nabla \tilde{\eta} : \boldsymbol{\sigma} d\Omega + \int_{\Gamma_d^+} h \tilde{\eta} \cdot (t_d - p n^+) d\Gamma = \int_{\Gamma_t} (\mathcal{H}_{\Gamma_d} \tilde{\eta}) \cdot t_t d\Gamma \quad (2.41)$$

Identical to the derivation of the momentum balance, the continuous mass balance ( $\tilde{\zeta} = 0$ ) and the discontinuous part ( $\hat{\zeta} = 0$ ) are considered.

### 2.3.3.3: Continuous mass balance $\hat{\zeta} = 0$

$$\begin{aligned} & - \int_{\Omega} \hat{\zeta} \nabla \cdot v_s d\Omega + \int_{\Omega} \nabla \hat{\zeta} \cdot q d\Omega = \\ & \int_{\Gamma_f} \hat{\zeta} f_f d\Gamma - \int_{\Gamma_d^+} \hat{\zeta} q_{\Gamma_d^+} \cdot n^+ d\Gamma - \int_{\Gamma_d^-} \hat{\zeta} q_{\Gamma_d^-} \cdot n^- d\Gamma \end{aligned} \quad (2.42)$$

The last two integrals represent the fluid flow through the crack. These terms are given in equation (2.31):

$$\begin{aligned} & - \int_{\Gamma_d^+} \hat{\zeta} q_{\Gamma_d^+} \cdot n^+ d\Gamma - \int_{\Gamma_d^-} \hat{\zeta} q_{\Gamma_d^-} \cdot n^- d\Gamma = \\ & - \int_{\Gamma_d^+} \hat{\zeta} (q_{\Gamma_d^+} \cdot n^+ + q_{\Gamma_d^-} \cdot n^-) d\Gamma = \int_{\Gamma_d^+} \hat{\zeta} [\dot{u}]_n d\Gamma \end{aligned} \quad (2.43)$$

Using (2.44) in the mass balance equation, this leads to the continuous mass balance:

$$- \int_{\Omega} \hat{\zeta} \nabla \cdot v_s d\Omega + \int_{\Omega} \nabla \hat{\zeta} \cdot q d\Omega - \int_{\Gamma_d^+} \hat{\zeta} [\dot{u}]_n d\Gamma = \int_{\Gamma_f} \hat{\zeta} f_f d\Gamma \quad (2.44)$$

### 2.3.3.4: Discontinuous mass balance $\tilde{\zeta} = 0$

Immediately, using  $\mathcal{D}_{\Gamma_d} = 0$  on  $\Gamma_d$ , the discontinuous equation for the mass balance is reduced to:

$$- \int_{\Omega} \mathcal{D}_{\Gamma_d} \tilde{\zeta} \nabla \cdot v_s d\Omega + \int_{\Omega} \nabla \mathcal{D}_{\Gamma_d} \tilde{\zeta} \cdot q d\Omega = \int_{\Gamma_f} \mathcal{D}_{\Gamma_d} \tilde{\zeta} f_f d\Gamma \quad (2.45)$$

where  $\delta \mathcal{D}_{\Gamma_d}$  is the gradient of the signed distance function.

## 2.4: Numerical description

The governing equations, including boundary conditions and local behavior at the crack surface, were given. These equation are solved in a FEM context.

By using a 2D FEM, a body is discretized into small elements where every node has two displacement degrees of freedom and one pressure degree of freedom. In this configuration, jump in the displacement field cannot be captured as present in a fracture. Hence, the nodes surrounding the discontinuity are enhanced with additional degrees of freedom by exploiting the partition of unity property of finite element shape functions [63, 105].

A continuous scalar field  $f(x, t)$  in a domain can be represented by discrete values that are assigned to the nodes and their corresponding shape functions:

$$f(x, t) = \sum_{i=1}^{n_{nod}} \phi_i(x) a_i(t) \quad (2.46)$$

here  $\phi_i(x)$  is the shape function associated to node  $i$  and  $a_i(t)$  is the discrete value of the scalar field  $f$  in that specific node. The shape function  $\phi_i(x)$  is therefore equal to 1 in node  $i$  and 0 in all other nodes. Additionally, the set of shape functions possesses the so-called partition of unity property, which implies that the sum of all shape functions in an arbitrary point  $x$  in the domain is equal to 1:

$$\sum_{i=1}^{n_{nod}} \phi_i(x) = 1 \quad \forall x \in \Omega \quad (2.47)$$

The part of the domain  $\Omega$  for which the magnitude of the shape function of node  $i$  is non-zero is called the *support of the node*. It has been shown [11] that when the field  $f(x, t)$  is not continuous, it can still be discretised using the FE shape functions by means of a combination with an enhanced basis function, according to:

$$f(x, t) = \sum_{i=1}^{n_{mod}} \phi_i(x) \left( a_i(t) + \sum_{j=1}^m \gamma_j(x) b_{ij}(t) \right) \quad (2.48)$$

where  $\gamma_j(x, t)$  is an enhanced basis with  $m$  orthogonal terms and  $b_{ij}$  are the additional nodal degrees of freedom that support the enhanced basis functions. The number  $m$  of enhanced base functions may be different for each node  $i$  in the model. However, in order to avoid linear dependence, the enhanced basis  $\gamma_j$  and the shape functions  $\phi_i$  may not originate from the same span of functions.

The displacement field is enhanced with the Heaviside function causing the fracture to be represented by a jump in the displacement field. The pressure is enhanced with the distance function, therefore it must be enriched with a continuous function that has a discontinuous spatial derivative.

Discretization is performed following the Bubnov-Galerkin approach. Momentum and mass balance will be derived in a FE formulation with displacement and pressure as degrees of freedom. Both pressure and displacement fields are interpolated with bilinear shape functions. The time discretization is performed with an implicit Euler time scheme. The resulting system is time-dependent and non-linear, and it is therefore solved using a Crank-Nicholson scheme for time-integration and Newton-Raphson iteration within each time increment. The porous media is considered to be fully saturated with a fluid and subjected to small variations in the displacement gradient. The bulk poroelasticity is based on Biot theory.

Consider a finite element domain crossed by a discontinuity as shown in Figure 2.5. A structured mesh containing four nodal elements is used in this work. Additional degrees of freedom are added to the black nodes that are crossed by the discontinuity.

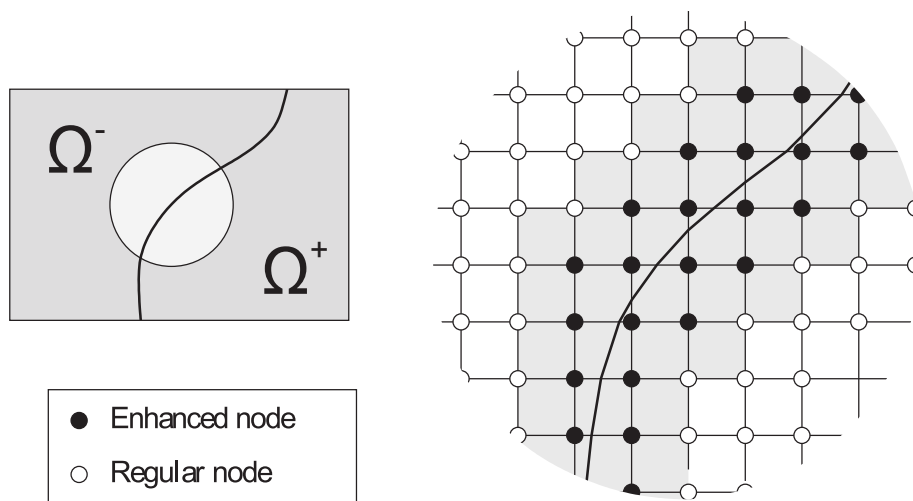


Figure 2.5: Two-dimensional finite element mesh crossed by a discontinuity represented by the black bold line. The black nodes are enhanced with additional degrees of freedom notated by  $\tilde{\cdot}$ . The gray elements contain additional terms in the stiffness matrix and the internal force vector.

It is assumed that the discontinuity within an element is a straight line, always ends at an element edge, and it is referred to as *cohesive segment*.

The numerical integration is performed by the standard Gauss integration. However, only using the original integration points, is not sufficient any more since the discontinuity can cross at least an element at arbitrary direction. In order to acquire sufficient integrations points at each side of the discontinuity an adopted integration method, introduced by Wells and Sluys [105], is used (see Figure 2.6). Two integration points per element are located at the discontinuity to integrate the discretized local balance equations.

Following the Bubnov-Galerkin approach, the discretized displacement fields becomes:

$$u = N\hat{u} + \mathcal{H}_{\Gamma_d}N\tilde{u} \quad (2.49)$$

$$p = H\hat{p} + \mathcal{D}_{\Gamma_d}H\tilde{p} \quad (2.50)$$

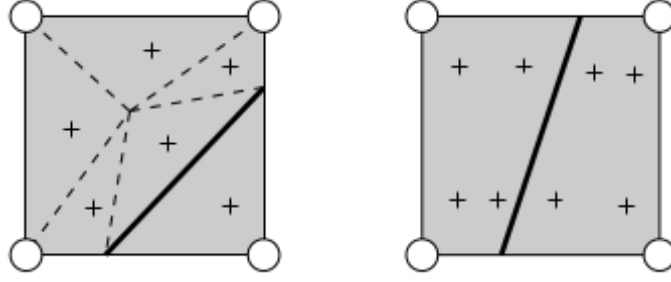


Figure 2.6: Numerical integration of quadrilateral elements crossed by a discontinuity (bold line). The sample points are denoted by a +. The element on the left is split into a sub-element with five vertices and one with three vertices. The first part must be triangulated into five smaller areas, denoted by the dashed lines. Each of these areas is integrated using a standard 1 point Gauss integration scheme. The element on the right is split into two quadrilateral sub-elements. Each of these parts can be integrated with a standard  $2 \times 2$  Gauss integration scheme.

where  $\underline{N}$  and  $\underline{H}$  contain the shape functions for respectively the nodal displacement and pressure. The columns  $\hat{u}$  and  $\hat{p}$  contain the continuous nodal values of respectively the displacement and the pressure while  $\tilde{u}$  and  $\tilde{p}$  contain the values in the enhanced nodes.

The discretized strain in the bulk can be calculated as:

$$\begin{aligned} \underline{\epsilon} &= \nabla^s u = \nabla^s \underline{N} \hat{u} + \mathcal{H}_{\Gamma_d} \nabla^s \underline{N} \tilde{u} \\ &= \underline{B} \hat{u} + \mathcal{H}_{\Gamma_d} \underline{B} \tilde{u} \end{aligned} \quad (2.51)$$

with  $\underline{B} = \nabla^s \underline{N}$ .

The discretized gradient of the pressure is defined as follows:

$$\nabla p = \nabla \underline{H} \hat{p} + (\mathcal{D}_{\Gamma_d} \nabla \underline{H} + \delta \mathcal{D}_{\Gamma_d} \underline{H}) \tilde{p} \quad (2.52)$$

The constitutive equation for the total stress is:

$$\nabla \cdot \underline{\sigma} = \underline{\sigma}_e - p \mathbf{I} \quad (2.53)$$

The total stress, written in vector notation as  $\underline{\sigma} = [\sigma_{xx} \ \sigma_{yy} \ \sigma_{xy}]^T$ , can be transformed using equation (2.49) to nodal values:

$$\begin{aligned} \underline{\sigma}_{\sim} &= \frac{\delta \underline{\sigma}}{\delta \underline{\epsilon}} \frac{\delta \underline{\epsilon}}{\delta \hat{\underline{u}}_{\sim}} \hat{\underline{u}}_{\sim} + \frac{\delta \underline{\sigma}}{\delta \underline{\epsilon}} \frac{\delta \underline{\epsilon}}{\delta \tilde{\underline{u}}_{\sim}} \tilde{\underline{u}}_{\sim} + \frac{\delta \underline{\sigma}}{\delta \hat{\underline{p}}_{\sim}} \hat{\underline{p}}_{\sim} + \frac{\delta \underline{\sigma}}{\delta \tilde{\underline{p}}_{\sim}} \tilde{\underline{p}}_{\sim} \\ &= \underline{\mathbf{D}} \underline{\mathbf{B}} \hat{\underline{u}}_{\sim} + \mathcal{H}_{\Gamma_d} \underline{\mathbf{D}} \underline{\mathbf{B}} \tilde{\underline{u}}_{\sim} + \underline{\mathbf{H}} \hat{\underline{p}}_{\sim} + \mathcal{D}_{\Gamma_d} \underline{\mathbf{H}} \tilde{\underline{p}}_{\sim} \end{aligned} \quad (2.54)$$

with  $\underline{\mathbf{D}}$  being the stiffness matrix defined as:

$$\underline{\mathbf{D}} = \begin{pmatrix} c & c - 2\mu & 0 \\ c - 2\mu & c & 0 \\ 0 & 0 & 2\mu \end{pmatrix}$$

with  $c = 2\mu + \lambda$ . Where  $\mu$  and  $\lambda$  represent, respectively, the first and the second Lamé constants.

The flow is transformed by:

$$q = \frac{\delta q}{\delta \hat{\underline{u}}_{\sim}} \hat{\underline{u}}_{\sim} + \frac{\delta q}{\delta \tilde{\underline{u}}_{\sim}} \tilde{\underline{u}}_{\sim} + \frac{\delta q}{\delta \hat{\underline{p}}_{\sim}} \hat{\underline{p}}_{\sim} + \frac{\delta q}{\delta \tilde{\underline{p}}_{\sim}} \tilde{\underline{p}}_{\sim} \quad (2.55)$$

$$= -k_f \nabla \underline{\mathbf{H}} \hat{\underline{p}}_{\sim} - k_f (\mathcal{D}_{\Gamma_d} \nabla \underline{\mathbf{H}} + \delta \mathcal{D}_{\Gamma_d} \underline{\mathbf{H}}) \tilde{\underline{p}}_{\sim} \quad (2.56)$$

#### 2.4.1: Discretized momentum equations

Using (2.49), (2.51) and (2.54), the continuous momentum equation can be discretized into:

$$\int_{\Omega_e} \underline{\mathbf{B}}^T \underline{\mathbf{D}} \underline{\mathbf{B}} d\Omega_e \hat{\mathbf{u}} + \int_{\Omega_e} \mathcal{H}_{\Gamma_d} \underline{\mathbf{B}}^T \underline{\mathbf{D}} \underline{\mathbf{B}} d\Omega_e \tilde{\mathbf{u}} - \int_{\Omega_e} \underline{\mathbf{B}}^T (\underline{\mathbf{m}} \underline{\mathbf{H}}) d\Omega_e \hat{\mathbf{p}} - \int_{\Omega_e} \mathcal{D}_{\Gamma_d} \underline{\mathbf{B}}^T (\underline{\mathbf{m}} \underline{\mathbf{H}}) d\Omega_e \tilde{\mathbf{p}} =$$

$$\int_{\Gamma_t} \underline{\mathbf{N}}^T \underline{\mathbf{t}}_t d\Gamma$$
(2.57)

with  $\underline{\mathbf{m}}$  being a column vector  $\underline{\mathbf{m}} = [1, 1, 0]^T$ .

In order to discretize the discontinuous momentum equation, the discretization of the tractions at discontinuity  $\Gamma_d$  is needed:

$$\underline{\mathbf{t}}_d = h \underline{\mathbf{Q}}^T \underline{\mathbf{T}}_{ed} \underline{\mathbf{Q}} \underline{\mathbf{N}} \tilde{\mathbf{u}} - n^+ \underline{\mathbf{H}} \hat{\mathbf{p}}$$
(2.58)

here is  $\underline{\mathbf{T}}_{ed}$  the linearized tangent stiffness of the cohesive material law defined in the local coordinate system of the crack and,  $\underline{\mathbf{Q}}$  is an orthogonal transformation matrix that performs the transformation from the local coordinate system to the global coordinate system [76]. In (2.58) it is assumed that the pressure at the crack surface is only determined by the continuous nodes:  $p = \hat{p}$ . The tangent stiffness in the global coordinate system is defined as  $\underline{\mathbf{T}} = \underline{\mathbf{Q}}^T \underline{\mathbf{T}}_{ed} \underline{\mathbf{Q}}$ .

The discretization of the discontinuous momentum equation (2.41) in separate terms reads:

$$\int_{\Omega} \mathcal{H}_{\Gamma_d} \nabla \tilde{\eta} : \underline{\boldsymbol{\sigma}} d\Omega =$$

$$\int_{\Omega_e} \mathcal{H}_{\Gamma_d} \underline{\mathbf{B}}^T \underline{\mathbf{D}} \underline{\mathbf{B}} d\Omega_e \hat{\mathbf{u}} + \int_{\Omega_e} \mathcal{H}_{\Gamma_d}^2 \underline{\mathbf{B}}^T \underline{\mathbf{D}} \underline{\mathbf{B}} d\Omega_e \tilde{\mathbf{u}} - \int_{\Omega_e} \mathcal{H}_{\Gamma_d} \underline{\mathbf{B}}^T (\underline{\mathbf{m}} \underline{\mathbf{H}}) d\Omega_e \hat{\mathbf{p}}$$

$$- \int_{\Omega_e} \mathcal{H}_{\Gamma_d} \mathcal{D}_{\Gamma_d} \underline{\mathbf{B}}^T (\underline{\mathbf{m}} \underline{\mathbf{H}}) d\Omega_e \tilde{\mathbf{p}}$$
(2.59)



$$\int_{\Gamma_d^+} h\tilde{\eta} \cdot (t_d - pn^+)d\Gamma = \int_{\Gamma_d^+} h\tilde{N}^T \underline{\mathbb{T}} \tilde{N} d\Gamma \tilde{u} - \int_{\Gamma_d^+} h\tilde{N}^T n^+ H d\Gamma \hat{p} \quad (2.60)$$

Putting the results together, the discontinuous part of the momentum equation is therefore achieved:

$$\begin{aligned} & \int_{\Omega_e} \mathcal{H}_{\Gamma_d} \underline{\mathbb{B}}^T \underline{\mathbb{D}} \underline{\mathbb{B}} d\Omega_e \hat{u} + \int_{\Omega_e} \mathcal{H}_{\Gamma_d}^2 \underline{\mathbb{B}}^T \underline{\mathbb{D}} \underline{\mathbb{B}} d\Omega_e \tilde{u} - \int_{\Omega_e} \mathcal{H}_{\Gamma_d} \underline{\mathbb{B}}^T (m\tilde{H}) d\Omega_e \hat{p} \\ & - \int_{\Omega_e} \mathcal{H}_{\Gamma_d} \mathcal{D}_{\Gamma_d} \underline{\mathbb{B}}^T (m\tilde{H}) d\Omega_e \tilde{p} + \int_{\Gamma_d^+} h\tilde{N}^T \underline{\mathbb{T}} \tilde{N} d\Gamma \tilde{u} - \int_{\Gamma_d^+} h\tilde{N}^T n^+ H d\Gamma \hat{p} \\ & = \int_{\Gamma_t} \mathcal{H}_{\Gamma_d} N t_t d\Gamma \end{aligned} \quad (2.61)$$

#### 2.4.2: Discretized mass balance

Using  $\nabla \cdot v_s = \underline{m}^T \nabla v_s$  and following the same procedure as in the previous section, the discrete continuous mass balance is given by:

$$\begin{aligned} & - \int_{\Omega_e} \tilde{H}^T \tilde{m}^T \underline{\mathbb{B}} d\Omega_e \dot{\hat{u}} - \int_{\Omega_e} \mathcal{H}_{\Gamma_d} \tilde{H}^T \tilde{m}^T \underline{\mathbb{B}} d\Omega_e \dot{\tilde{u}} - \int_{\Omega_e} k_f \nabla \tilde{H}^T \nabla \tilde{H} d\Omega_e \hat{p} \\ & - \int_{\Omega_e} k_f \nabla \tilde{H}^T (\mathcal{D}_{\Gamma_d} \nabla \tilde{H} + \delta \mathcal{D}_{\Gamma_d} \tilde{H}) d\Omega_e \tilde{p} - h \int_{\Gamma_d^+} \tilde{H}^T (n^+)^T \tilde{N} d\Gamma \dot{\tilde{u}} = \\ & \int_{\Gamma_f} \tilde{H}^T f_f d\Gamma \end{aligned} \quad (2.62)$$

Doing the same for the discontinuous part of the mass balance equation, this leads to:

$$\begin{aligned} & - \int_{\Omega_e} \mathcal{D}_{\Gamma_d} \tilde{H}^T \tilde{m}^T \underline{\mathbb{B}} d\Omega_e \dot{\hat{u}} - \int_{\Omega_e} \mathcal{D}_{\Gamma_d} \mathcal{H}_{\Gamma_d} \tilde{H}^T \tilde{m}^T \underline{\mathbb{B}} d\Omega_e \dot{\tilde{u}} \\ & - \int_{\Omega_e} k_f (\mathcal{D}_{\Gamma_d} \nabla \tilde{H} + \delta \mathcal{D}_{\Gamma_d} \tilde{H}) \nabla \tilde{H} d\Omega_e \hat{p} \\ & - \int_{\Omega_e} k_f (\mathcal{D}_{\Gamma_d} \nabla \tilde{H} + \delta \mathcal{D}_{\Gamma_d} \tilde{H})^T (\mathcal{D}_{\Gamma_d} \nabla \tilde{H} + \delta \mathcal{D}_{\Gamma_d} \tilde{H}) d\Omega_e \tilde{p} = \int_{\Gamma_f} \mathcal{D}_{\Gamma_d} \tilde{H}^T f_f d\Gamma \end{aligned} \quad (2.63)$$

### 2.4.3: Discrete system of equations

The discrete equations for the momentum balance (2.57, 2.61) and mass balance (2.62, 2.63) lead to following set of equations:

$$\begin{bmatrix} 0 & 0 & 0 & 0 \\ 0 & 0 & 0 & 0 \\ \underline{C}_{\hat{p}\hat{u}} & \underline{C}_{\hat{p}\tilde{u}} & 0 & 0 \\ \underline{C}_{\tilde{p}\hat{u}} & \underline{C}_{\tilde{p}\tilde{u}} & 0 & 0 \end{bmatrix} \begin{bmatrix} \dot{\hat{u}} \\ \dot{\tilde{u}} \\ \dot{\hat{p}} \\ \dot{\tilde{p}} \end{bmatrix} + \begin{bmatrix} \underline{K}_{\hat{u}\hat{u}} & \underline{K}_{\hat{u}\tilde{u}} & \underline{C}_{\hat{u}\hat{p}} & \underline{C}_{\hat{u}\tilde{p}} \\ \underline{K}_{\tilde{u}\hat{u}} & \underline{K}_{\tilde{u}\tilde{u}} & \underline{C}_{\tilde{u}\hat{p}} & \underline{C}_{\tilde{u}\tilde{p}} \\ 0 & 0 & \underline{M}_{\hat{p}\hat{p}} & \underline{M}_{\hat{p}\tilde{p}} \\ 0 & 0 & \underline{M}_{\tilde{p}\hat{p}} & \underline{M}_{\tilde{p}\tilde{p}} \end{bmatrix} \begin{bmatrix} \hat{u} \\ \tilde{u} \\ \hat{p} \\ \tilde{p} \end{bmatrix} = \begin{bmatrix} \mathcal{L}_{\hat{u}}^{ext} \\ \mathcal{L}_{\tilde{u}}^{ext} \\ \mathcal{L}_{\hat{p}}^{ext} \\ \mathcal{L}_{\tilde{p}}^{ext} \end{bmatrix} \quad (2.64)$$

The element matrices are divided in two categories:

The stiffness matrices:

$$\begin{aligned} \underline{K}_{\hat{u}\hat{u}} &= \int_{\Omega_e} \underline{B}^T \underline{D} \underline{B} d\Omega_e \\ \underline{K}_{\hat{u}\tilde{u}} &= \int_{\Omega_e} \mathcal{H}_{\Gamma_d} \underline{B}^T \underline{D} \underline{B} d\Omega_e \\ \underline{K}_{\tilde{u}\tilde{u}} &= \int_{\Omega_e} \mathcal{H}_{\Gamma_d}^2 \underline{B}^T \underline{D} \underline{B} d\Omega_e + \int_{\Gamma_d^+} h \underline{N}^T \underline{T} \underline{N} d\Gamma \\ \underline{M}_{\hat{p}\hat{p}} &= - \int_{\Omega_e} k_f \nabla \underline{H}^T \nabla \underline{H} d\Omega_e \\ \underline{M}_{\hat{p}\tilde{p}} &= - \int_{\Omega_e} k_f \nabla \underline{H}^T (\mathcal{D}_{\Gamma_d} \nabla \underline{H} + \delta \vec{\mathcal{D}}_{\Gamma_d} \underline{H}) \\ \underline{M}_{\tilde{p}\hat{p}} &= - \int_{\Omega_e} k_f (\mathcal{D}_{\Gamma_d} \nabla \underline{H} + \delta \vec{\mathcal{D}}_{\Gamma_d} \underline{H})^T \nabla \underline{H} d\Omega_e \\ \underline{M}_{\tilde{p}\tilde{p}} &= - \int_{\Omega_e} k_f (\mathcal{D}_{\Gamma_d} \nabla \underline{H} + \delta \vec{\mathcal{D}}_{\Gamma_d} \underline{H})^T (\mathcal{D}_{\Gamma_d} \nabla \underline{H} + \delta \vec{\mathcal{D}}_{\Gamma_d} \underline{H}) d\Omega_e \end{aligned}$$

and the coupling matrices:

$$\begin{aligned}
\underline{\underline{C}}_{\hat{u}\hat{p}} &= - \int_{\Omega_e} \underline{\underline{B}}^T(\underline{\underline{m}}\underline{\underline{H}})d\Omega_e \\
\underline{\underline{C}}_{\hat{u}\hat{p}} &= - \int_{\Omega_e} \mathcal{D}_{\Gamma_d}\underline{\underline{B}}^T(\underline{\underline{m}}\underline{\underline{H}})d\Omega_e \\
\underline{\underline{C}}_{\hat{u}\hat{p}} &= - \int_{\Omega_e} \mathcal{H}_{\Gamma_d}\underline{\underline{B}}^T(\underline{\underline{m}}\underline{\underline{H}})d\Omega_e - \int_{\Gamma_d^+} hN^T n^+ \underline{\underline{H}}d\Gamma \\
\underline{\underline{C}}_{\hat{u}\hat{p}} &= - \int_{\Omega_e} \mathcal{H}_{\Gamma_d}\mathcal{D}_{\Gamma_d}\underline{\underline{B}}^T(\underline{\underline{m}}\underline{\underline{H}})d\Omega_e \\
\underline{\underline{C}}_{\hat{p}\hat{u}} &= - \int_{\Omega_e} \underline{\underline{H}}^T \underline{\underline{m}}^T \underline{\underline{B}}d\Omega_e \\
\underline{\underline{C}}_{\hat{p}\hat{u}} &= - \int_{\Omega_e} \mathcal{H}_{\Gamma_d}\underline{\underline{H}}^T \underline{\underline{m}}^T \underline{\underline{B}}d\Omega_e - \int_{\Gamma_d^+} h\underline{\underline{H}}^T (n^+)^T \underline{\underline{N}}d\Gamma \\
\underline{\underline{C}}_{\hat{p}\hat{u}} &= - \int_{\Omega_e} \mathcal{D}_{\Gamma_d}\underline{\underline{H}}^T \underline{\underline{m}}^T \underline{\underline{B}}d\Omega_e \\
\underline{\underline{C}}_{\hat{p}\hat{u}} &= - \int_{\Omega_e} \mathcal{D}_{\Gamma_d}\mathcal{H}_{\Gamma_d}\underline{\underline{H}}^T \underline{\underline{m}}^T \underline{\underline{B}}d\Omega_e
\end{aligned}$$

The external force vectors are given by:

$$\begin{aligned}
\underline{\underline{f}}_{\hat{u}}^{ext} &= \int_{\Gamma_t} \underline{\underline{N}}^T t_t d\Gamma \\
\underline{\underline{f}}_{\hat{u}}^{ext} &= \int_{\Gamma_t} \mathcal{H}_{\Gamma_d} \underline{\underline{N}} t_t d\Gamma \\
\underline{\underline{f}}_{\hat{p}}^{ext} &= \int_{\Gamma_f} \underline{\underline{H}}^T f_f d\Gamma \\
\underline{\underline{f}}_{\hat{p}}^{ext} &= \int_{\Gamma_f} \mathcal{D}_{\Gamma_d} \underline{\underline{H}}^T f_f d\Gamma
\end{aligned}$$

In order to solve this system of equations, the Crank-Nicholson scheme is used. Time dependent terms are approximated in a linearized way by means of:

$$\frac{\delta(\cdot)}{\delta t} = \frac{(\cdot)^{t+\Delta t} - (\cdot)^t}{\Delta t} \tag{2.65}$$

where the term  $(\cdot)^{t+\Delta t}$  is the unknown solution at the next time step,  $(\cdot)^t$  is the known solution from the previous time step, and  $\Delta t$  is the length of the time step. On the other hand, the time independent terms are approximated by a scaling between the old and new time step by:

$$(\cdot) = \bar{\theta}(\cdot)^{t+\Delta t} + (1 - \bar{\theta})(\cdot)^t \quad \text{and} \quad \bar{\theta} \in [0, 1] \quad (2.66)$$

Previous literature [55] concluded that stabilization is reached if  $\bar{\theta} \geq \frac{1}{2}$ .

The Euler implicit time scheme is retrieved when  $\bar{\theta} = 1$ , while for  $\bar{\theta} = 0$  the explicit Euler scheme is retrieved. Taking a short time step, it will lead to initial oscillations. In order to have a stable time integration the following law needs to be satisfied [55, 103]:

$$\Delta t > \frac{\Delta x^2}{ck_f} \quad (2.67)$$

here  $x$  is the length of the element and  $c$  is usually the consolidation constant. For an incompressible material, like the one used in this Thesis, the denominator becomes  $(E \cdot K)$ .

At this point, the general system of equations is linear. However, the cohesive law introduces a non-linear term to the system. In order to solve the system in an iterative way, a linearization of the system is needed, according to:

$$\underline{\sigma}_j = \underline{\sigma}_{j-1} + \delta \underline{\sigma} \quad (2.68)$$

$$p_j = p_{j-1} + \delta p \quad (2.69)$$

in which subscripts  $j$  and  $j - 1$  define the iteration numbers. In combination with the time stepping scheme, the following result can be found:

$$\frac{(\cdot)_{j-1}^{t+\Delta t} + \delta(\cdot) - (\cdot)^t}{\Delta t} + \bar{\theta}\{(\cdot)_{j-1}^{t+\Delta t} + \delta(\cdot)\} + (1 - \bar{\theta})(\cdot)^t \quad (2.70)$$

Using this last tool in System (2.64), the final system can be obtained:

$$\begin{bmatrix} \underline{\mathbf{K}}_{\hat{u}\hat{u}} & \underline{\mathbf{K}}_{\hat{u}\tilde{u}} & \underline{\mathbf{C}}_{\hat{u}\hat{p}} & \underline{\mathbf{C}}_{\hat{u}\tilde{p}} \\ \underline{\mathbf{K}}_{\tilde{u}\hat{u}} & \underline{\mathbf{K}}_{\tilde{u}\tilde{u}} & \underline{\mathbf{C}}_{\tilde{u}\hat{p}} & \underline{\mathbf{C}}_{\tilde{u}\tilde{p}} \\ \underline{\mathbf{C}}_{\hat{p}\hat{u}} & \underline{\mathbf{C}}_{\hat{p}\tilde{u}} & \bar{\theta}\Delta t\underline{\mathbf{M}}_{\hat{p}\hat{p}} & \bar{\theta}\Delta t\underline{\mathbf{M}}_{\hat{p}\tilde{p}} \\ \underline{\mathbf{C}}_{\tilde{p}\hat{u}} & \underline{\mathbf{C}}_{\tilde{p}\tilde{u}} & \bar{\theta}\Delta t\underline{\mathbf{M}}_{\tilde{p}\hat{p}} & \bar{\theta}\Delta t\underline{\mathbf{M}}_{\tilde{p}\tilde{p}} \end{bmatrix} \begin{bmatrix} \delta\hat{u} \\ \delta\tilde{u} \\ \delta\hat{p} \\ \delta\tilde{p} \end{bmatrix} = \begin{bmatrix} \underline{\mathcal{L}}_{\hat{u}}^{ext} & -\underline{\mathcal{L}}_{\hat{u}}^{int} \\ \underline{\mathcal{L}}_{\tilde{u}}^{ext} & -\underline{\mathcal{L}}_{\tilde{u}}^{int} \\ \Delta t\underline{\mathcal{L}}_{\hat{p}}^{ext} & -\underline{\mathcal{L}}_{\hat{p}}^{int} \\ \Delta\underline{\mathcal{L}}_{\tilde{p}}^{ext} & -\underline{\mathcal{L}}_{\tilde{p}}^{int} \end{bmatrix} \quad (2.71)$$

$$\underline{\mathcal{L}}_{\hat{u}}^{ext} = \int_{\Gamma_t} \underline{\mathbf{N}}^T t^{t+\Delta t} d\Gamma$$

$$\underline{\mathcal{L}}_{\hat{u}}^{int} = \int_{\Omega_e} \underline{\mathbf{B}}^T \underline{\sigma}_{j-1} d\Omega_e$$

$$\underline{\mathcal{L}}_{\tilde{u}}^{ext} = \int_{\Gamma_t} \mathcal{H}_{\Gamma_d} \underline{\mathbf{N}}^T t^{t+\Delta t} d\Gamma$$

$$\underline{\mathcal{L}}_{\tilde{u}}^{int} = \int_{\Omega_e} \mathcal{H}_{\Gamma_d} \underline{\mathbf{B}}^T \underline{\sigma}_{j-1} d\Omega_e + \int_{\Gamma_d^+} h \underline{\mathbf{N}}^T \{t_{d_{j-1}} - (p_{j-1}^{crack})\} d\Gamma$$

$$\underline{\mathcal{L}}_{\hat{p}}^{ext} = \int_{\Gamma_f} \Delta t \underline{\mathbf{H}}^T (\bar{\theta} f_f^{t+\Delta t} + (1 - \bar{\theta}) f_f^t) d\Gamma + \underline{\mathbf{H}}^T (s^+)^T \cdot q_{\Gamma_d} |_{S_d}$$

$$\begin{aligned} \underline{\mathcal{L}}_{\hat{p}}^{int} &= \underline{\mathbf{C}}_{\hat{p}\hat{u}} \cdot (\hat{u}_{j-1}^{t+\Delta t} - \hat{u}^t) + \underline{\mathbf{C}}_{\hat{p}\tilde{u}} \cdot (\tilde{u}_{j-1}^{t+\Delta t} - \tilde{u}^t) + \Delta t \underline{\mathbf{M}}_{\hat{p}\hat{p}} \cdot (\bar{\theta} \hat{p}_{j-1}^{t+\Delta t} + (1 - \bar{\theta}) \hat{p}^t) \\ &+ \Delta t \underline{\mathbf{M}}_{\hat{p}\tilde{p}} \cdot (\bar{\theta} \tilde{p}_{j-1}^{t+\Delta t} + (1 - \bar{\theta}) \tilde{p}^t) \end{aligned}$$

$$\underline{\mathcal{L}}_{\tilde{p}}^{ext} = \int_{\Gamma_f} \Delta t \underline{\mathbf{D}}_{\Gamma_d} \underline{\mathbf{H}}^T (\bar{\theta} f_f^{t+\Delta t} + (1 - \bar{\theta}) f_f^t) d\Gamma$$

$$\begin{aligned} \underline{\mathcal{L}}_{\tilde{p}}^{int} &= \underline{\mathbf{C}}_{\tilde{p}\hat{u}} \cdot (\hat{u}_{j-1}^{t+\Delta t} - \hat{u}^t) + \underline{\mathbf{C}}_{\tilde{p}\tilde{u}} \cdot (\tilde{u}_{j-1}^{t+\Delta t} - \tilde{u}^t) + \Delta t \underline{\mathbf{M}}_{\tilde{p}\hat{p}} \cdot (\bar{\theta} \hat{p}_{j-1}^{t+\Delta t} + (1 - \bar{\theta}) \hat{p}^t) \\ &+ \Delta t \underline{\mathbf{M}}_{\tilde{p}\tilde{p}} \cdot (\bar{\theta} \tilde{p}_{j-1}^{t+\Delta t} + (1 - \bar{\theta}) \tilde{p}^t) \end{aligned}$$

This matrix is symmetric if the linearized stiffness matrix, which descends from the cohesive law, is symmetric. With the Camacho-Ortiz cohesive law, that will be introduced in the next paragraph, this is not the case. However, for the solution, this method does not suffer this kind of problems [55]. As mentioned before, the system is

solved in an iterative way using the Newton-Raphson method.

Convergence is therefore reached when:

$$\|\underline{\underline{f}}^{int} - \underline{\underline{f}}^{ext}\| \leq \epsilon_{res} \|\underline{\underline{f}}^{int}\| \quad (2.72)$$

where  $\epsilon_{res}$  is a given precision and:

$$\|\underline{\underline{f}}\| = \sqrt{\underline{\underline{f}} \underline{\underline{f}}^T} \quad (2.73)$$

## 2.5: Cohesive zone method

The first part of this section explains how the numerical model handles crack nucleation and propagation. In the second part the cohesive zone model, used in this work, is explained.

### 2.5.1: Crack nucleation and propagation

The development of micro-cracks into mature cracks can be divided into 3 stages: nucleation, growth and merging. The merging of two cracks in the vicinity of each other is not considered in this work. To govern the nucleation and the propagation of a fracture, a yield criterion is needed to determine the moment and the direction of the propagating fracture. The stress state at the crack tip is not known exactly, hence an approximation based on the stress in the integration points surrounding the crack tip is necessary. Therefore, a Gaussian weighting function is used to calculate the average stress [49]. The average stress  $\sigma_{av}$  at the crack tip is then the weighted sum of the integration points near the crack tip:

$$\sigma_{av} = \sum_{i=1}^{n_{int}} \frac{w_i}{w_{tot}} \sigma_{e,i} \quad \text{with} \quad w_{tot} = \sum_{j=1}^{n_{int}} w_j \quad (2.74)$$

here  $n_{int}$  is the number of integration points in the domain,  $\sigma_{e,i}$  is the current

effective stress state at the integration point  $i$ , which has a weight factor  $w_i$  defined as:

$$w_i = \frac{(2\pi)^{\frac{2}{3}}}{l_a^3} e^{-\frac{r_i^2}{2l_a^2}} \quad (2.75)$$

with  $r_i$  being the distance between the crack tip and the integration point  $n_i$ , and  $l_a$  being a length scale parameter defining how fast the weight factor decays as a function of the distance between the integration points and the crack tip.

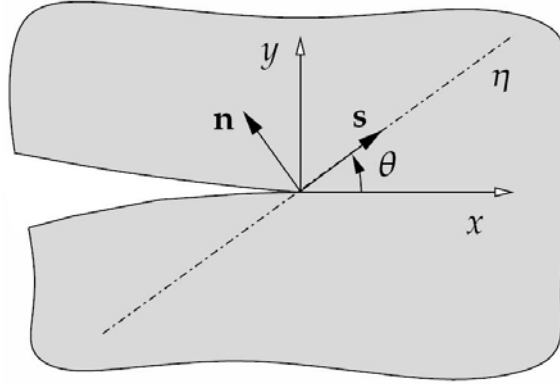


Figure 2.7: Schematic representation of a material with at the crack tip a global x-y coordinate system and a local coordinate system, described with a normal unit vector  $\mathbf{n}$  and a tangential unit vector  $\mathbf{s}$ .

As it was proposed by Remmers *et al.* [77], the average stress surrounding the crack tip is used to determine both the moment and the direction of propagation. From this average stress, an equivalent traction  $t_{\text{eq}}$  at the crack tip is calculated [22]:

$$t_{\text{eq}}(\theta) = \sqrt{\langle t_n \rangle^2 + \frac{1}{\beta} t_s^2} \quad \text{with} \quad \langle t_n \rangle = \begin{cases} 0 & \text{if } t_n \leq 0 \\ t_n & \text{if } t_n > 0 \end{cases} \quad (2.76)$$

where  $\langle \cdot \rangle$  are the McCauley brackets defined as:

$$\langle x \rangle = \begin{cases} 0 & \text{if } x \leq 0 \\ x & \text{if } x > 0 \end{cases} \quad (2.77)$$

Normal and shear tractions,  $t_n$  and  $t_s$ , can be calculated from the averaged tip

stress in equation (2.74) according to:

$$t_n = \mathbf{n}^T \boldsymbol{\sigma}_{av} \mathbf{n} \qquad t_s = \mathbf{s}^T \boldsymbol{\sigma}_{av} \mathbf{n} \qquad (2.78)$$

where  $\mathbf{n}$  and  $\mathbf{s}$  are respectively the normal and tangent vector to an axis  $\eta$ . The axis  $\eta$  is rotated by an angle  $\theta$  with respect to the x-axis (see Figure 2.7). The normal and tangent vector are defined by:

$$\mathbf{n} = [-\sin(\theta), \cos(\theta)]^T \qquad \mathbf{s} = [\cos(\theta), \sin(\theta)]^T \qquad (2.79)$$

The parameter  $\beta$  is used to scale the influence of the shear traction on the equivalent traction, typically  $\beta = 2.3$  is used [22, 77]. The equivalent traction can be calculated for all angles  $\theta$ .

If the maximum equivalent traction exceeds the yield strength  $\tau_{ult}$  of the material, the fracture is extended in the direction of angle  $\theta$  through one element. The angle for which this occurs is exactly the direction of the crack growth. Remmers *et al.* [76] showed that, due to the periodic trigonometric functions, it is sufficient to calculate the equivalent tractions for angles in the range of  $0 < \theta < \pi$ . The representation of extending an existing crack in a two-dimensional finite element mesh is shown in Figure 2.8. The extended discontinuity is a straight line through the next element. The part of the discontinuity that crosses through one element is called a cohesive segment.

For the calculation of the angle  $\theta$  and the initial tractions  $t_n$  and  $t_s$  of the new segment, two different averaged stresses  $\boldsymbol{\sigma}_{av}$  are used: (i) a smeared averaged stress with length scale  $l_a$  and (ii) a local averaged stress. The equivalent tractions calculated from the smeared stress are used to check whether the yield criterion is exceeded. The initial tractions are closely related to the local stress state. Therefore, initial tractions are calculated with the local stress using the angle  $\theta$  determined from the smeared stress.



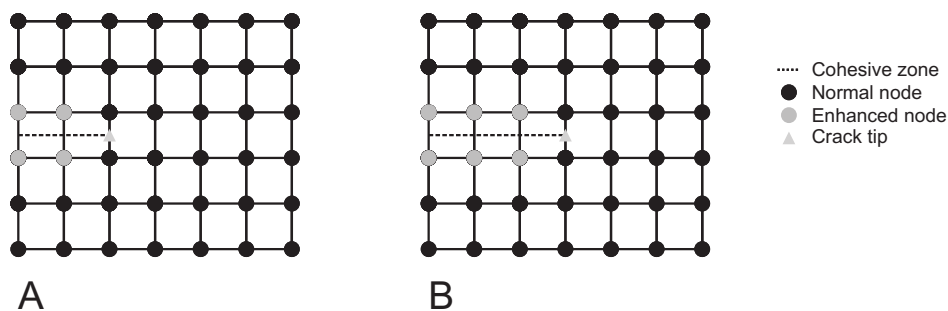


Figure 2.8: Representation of an extension of a discontinuity along a two-dimensional finite element mesh. Before crack propagation (A) and after crack propagation (B). Left: when the tractions in the additional sample point (denoted with the triangle) exceed the threshold value, the discontinuity is extended into the next element along the projected weak interface (dashed line). Right: the hashed nodes and the elements have just been enhanced. In this case the propagation angle  $\theta = 0$ . Note that in both pictures the nodes supporting the tip are not enhanced in order to have zero opening at the crack tip.

The disadvantage of using an average stress in the yield criterion is that the crack propagation can be slightly delayed due to the averaging of the stress. Instead, the advantage, is that the direction of propagation is more reliable since it is based on a global stress state. However, the initial tractions in the discontinuity will also be underestimated [77]. To avoid this problem, two different length scale parameters  $l_a$  are used, see Equation (2.75). The moment and direction of fracture propagation are determined by a length scale parameter which is typically three times the element size [105], while the initial tractions are calculated with one fourth of this length scale.

The average stress criterion based on the equivalent traction in Equation (2.76) is also used to determine the moment of fracture nucleation. Instead of calculating this criterion for each integration point in the mesh, which would be computationally inefficient, an additional checkpoint is added, since there is no integration point in the center of an element hence it is necessary to add an extra checkpoint to use Equation (2.74). Therefore, it is possible to restrict nucleation to a prescribed area. Thus, in order to further increase the numerical efficiency, the nucleation criterion is not calculated for every integration in an element but only once in the center of the element. Whenever the equivalent traction in one of the checkpoints exceeds the nucleation criterion, a discontinuity is added. The cohesive segment is assumed to be straight and

crosses the checkpoint under the angle  $\theta$  with respect to the x-axis. The cohesive zone of the nucleated crack must have a length of at least one element to be, kinematically speaking, possible.

However, since nucleation is not the goal of this research, numerical implementations of this restriction are illustrated in Figure 2.9 with three examples, and briefly described in the next section.

### 2.5.1.1: Examples

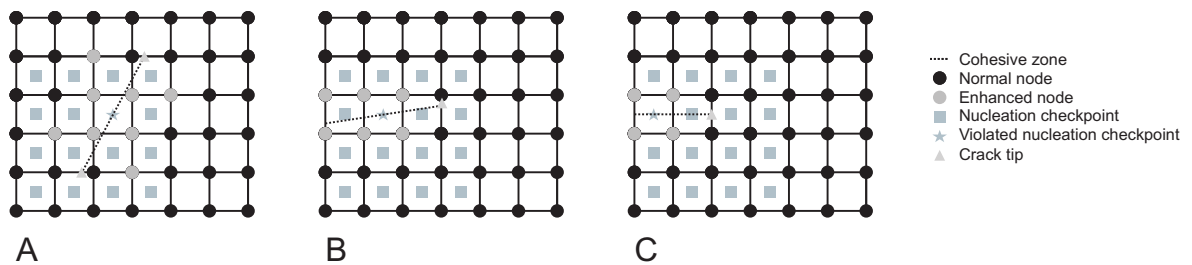


Figure 2.9: Three different locations of nucleation checkpoints with corresponding cohesive zones.

The first example is when the nucleation point is located in the middle of the material. The length of the cohesive zone is therefore such that crack tips are not located at the boundaries of the element, where the nucleation point is located (Figure 2.9 A).

A second example is illustrated with the nucleation point located in an element that is a neighbor of an element on the mesh boundary (Figure 2.9 B). Here, the nodes at the mesh boundary also need to be enhanced to prevent having a crack tip at the mesh boundary.

The last and simplest example is when the nucleation point is in an element at the mesh boundary (Figure 2.9 C). The cohesive zone is then only extended through one more element. If the nucleation criterion is exceeded in multiple checkpoints at the same time, nucleations occurs in the checkpoint with the highest equivalent traction. For further numerical implementation issues see Remmers *et al.* [77].

### 2.5.2: Cohesive zone model

The cohesive law used in this work was firstly introduced by Camacho and Ortiz [22]. In order to avoid sudden jumps in the stress field, the initial tractions of the cohesive segment are chosen to be equal to tractions calculated in equation (2.78) with the local length scale parameter. If the initial normal traction  $t_{n_0}$  is positive, the segment is assumed to open in tensile mode (mode I). A cohesive law is used for the damage evolution, i.e. softening behavior after reaching the critical stress state. The critical length can be obtained by:

$$\delta_n = \frac{G_c}{\tau_{ult}} \quad (2.80)$$

where  $\tau_{ult}$  represents the ultimate traction forces, and  $G_c$  is the fracture toughness. Fracture toughness is a property that describes the ability of a material containing a crack to resist fracture. It is therefore one of the most important properties in any material for many design applications [74].

Hence, when there is a positive opening of the crack, the cohesive law reads:

$$t_n = \tau_{ult} e^{-\frac{[u]_n}{\delta_n}} \quad \text{with} \quad [u]_n \geq 0 \quad (2.81)$$

This relation is shown in Figure 2.10. Note that the area underneath the softening curve is the fracture toughness  $G_c$ . From an analytical point of view, this is calculated:

$$\int_{-\infty}^{+\infty} t_n d[u]_n = \int_0^{+\infty} t_n d[u]_n = \tau_{ult} \delta_n \int_0^{+\infty} e^{-r} dr = \tau_{ult} \delta_n = G_c \quad (2.82)$$

In this model, a loading function  $f$  is defined as:

$$f(u_n, k) = u_n - k \quad (2.83)$$

where  $u_n$  is the normal separation crack and  $k$  is a history parameter.  $k$  is introduced

---

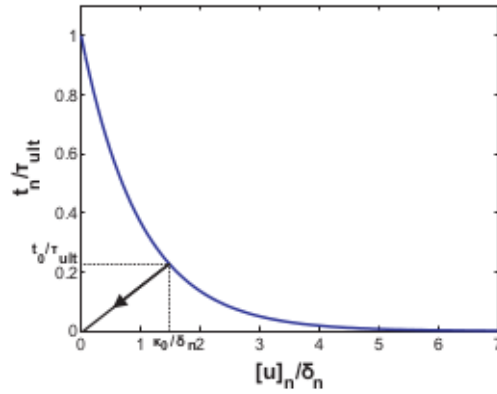


Figure 2.10: Normalized distribution of the exponential cohesive law for tensile loading related to traction forces and displacements.

in order to remember the current opening  $k_0$  and the traction  $\tau_0$  in case of unloading each time step, and it is equal to the largest value of  $u_n$  reached. When  $f = 0$ , loading occurs and when  $f < 0$  there is unloading. When the new opening is smaller than previous, then unloading can take place according to:

$$t_n = \frac{\tau_0}{k_0} [u]_n \quad (2.84)$$

Instead, damage is defined as:

$$D = 1 - \frac{t_n}{\tau_{ult}} \quad (2.85)$$

When the cohesive law approaches zero, a macro crack is developed (i.e. when the local damage approaches maximum,  $D = 1$ ). When locally the opening decreases, compared to previous time step, unloading takes place. The aforementioned cohesive law parameters  $G_c$  and  $\tau_{ult}$  can be obtained from experimental data.

## 3: Settings and Parameters

After the first Introduction concerning fracture mechanics and the overview about the numerical method implemented in this work, a presentation of the settings and parameters chosen for this Thesis will be given in this section.

### 3.1: Materials

A solid material is characterized by structural rigidity and resistance to changes of shape or volume. The atoms in a solid are tightly bound to each other. A solid does not exhibit macroscopic flow, as fluids do. Any degree of departure from its original shape is called *deformation*. The proportion of deformation to original size is called *strain*. If the applied stress is sufficiently low, almost all solid materials behave in such a way that the strain is directly proportional to the stress (Hooke's law). The coefficient of the proportion is called the modulus of elasticity or Young's modulus. This region of deformation is known as the linear-elastic region.

A porous medium (or a porous material) is a material formed by a solid skeleton that includes pores. These pores can be filled with air (void) or with fluid. The skeletal part of the material is often called *matrix* or *frame*.

A porous material put under a constant load is not deforming instantaneously but settles gradually to a final deformation. This is a common effect observed in sands, clays and rocks with the presence of an interstitial fluid. In geotechnics, this behavior is commonly referred to as *consolidation*. The rate of deformation due to the applied load depends on the velocity with which the water is squeezed out of the solid skeleton.

In 1923, Terzaghi [93, 94] described this coupling between the pore pressure and the solid skeleton deformation. Terzaghi assumed that a porous material was build up from internally connected elastic solid grains and a fluid filling the voids between the grains. In order to describe the consolidation behavior, Terzaghi introduced the effective stress notation. This means that the total stress in the porous material is divided into an effective stress in the solid skeleton and a hydrostatic pressure, according to:

$$\boldsymbol{\sigma} = \boldsymbol{\sigma}_e - p\mathbf{I} \quad (3.1)$$

where  $\boldsymbol{\sigma}$  is the total stress,  $\boldsymbol{\sigma}_e$  is the effective stress,  $p$  is the hydrostatic pressure and  $\mathbf{I}$  is the unit matrix. Even though Terzaghi's theory is almost one century aged, it is still remarkably accurate for the consolidation of 1D soil layers and is still being used as a benchmark (see also Appendix A). Later on, Biot presented a theory of three-dimensional poroelasticity of fluid saturated porous materials [16, 17].

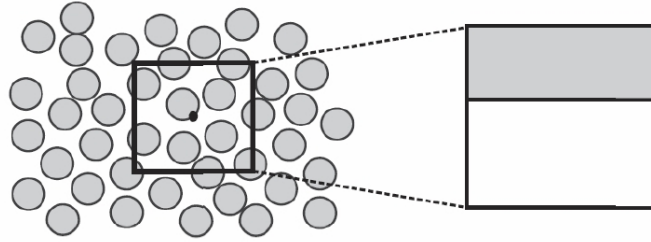


Figure 3.1: Schematic representation of the representative volume unit of the solid grains and the internal fluid.

Since the compressibility of the constituents is small with respect to the compressibility of the medium, the constituents are assumed to be incompressible also in this work. Instead this is not the case for hydraulic fracturing processes, where high pressures influence the compressibility both of the fluid and the bulk material. Small deformation theory is used.

In this work either solid and saturated porous media will be analyzed.

In particular, the porous beam used in the numerical simulations will be considered made of an isotropic material. In materials science, “isotropic” means having identical values of a property in all directions.

Crack initiation and propagation in an isotropic material occurs if the equivalent traction in equation (2.76) exceeds the fracture criterion  $\tau_{ult}$ . In an isotropic material this parameter is independent of the fracture direction. This means that there is no dependency between the orientation of the cohesive zone and the fiber direction. Thus, the strength of the material is equally distributed in the body of the material and there are no fiber directions with maximum of minimum values reached. To model fracture in an isotropic material, the fracture criterion  $\tau_{ult}$  is therefore taken to be independent

on the angle between the fiber direction and the normal of the fracture.

To summarize, it will be assumed a material which is: two-dimensional, linear elastic, isothermal, homogeneous, isotropic and fully saturated (the last assumption only for the porous phase). This does not represent exactly the reality of the shale/sandstone rocks formations (see Appendix B for further details) but the analysis of the results obtained could give indications for future projects.

The material chosen in this work is sandstone. The general mechanical properties of sandstone are listed in Table 3.1. A detailed description of petroleum rock mechanics, especially referring to shale and sandstone rocks, can be found in [3]. In the next Chapter the values of the parameters of interest will be precisely specified for every simulation.

Table 3.1: The mechanical properties given in this Table are the typical properties of two known rock materials which have been tested in laboratory for various applications. It should be noted that these properties may vary significantly depending especially on geological location, chemical compositions, internal defects or fissures, temperature, regional seismic activities, loading history, age, dimensions of test specimens.

	<b>SedimentaryClastic</b>	<b>Sandstone</b>	<b>Shale</b>
Elastic Properties	Poisson's Ratio	0.05 - 0.40	0.05 - 0.32
	Isotropic Elastic Modulus (GPa)	4.6 - 90.0	4.6 - 90.0
	Isotropic Shear Modulus (GPa)	1.9 - 36.7	1.9 - 36.7
Strength Properties	Tensile Strength (MPa)	2 - 25	2 - 25
	Shear Strength (MPa)	8 - 40	8 - 40
Other Properties	Porosity (%)	1.8 - 21.4	1.8 - 21.4
	Permeability ( $\mu\text{m}$ )	$10^{-5}$ - 0.1	$10^{-8}$ - $(2 \cdot 10^{-6})$

Note that in the input file of the material properties (named *sandstone.dat*) the Tensile Strength will be called 'Tultimate' and the Fracture Toughness simply 'Toughness'. In this work, only sandstone will be considered in the simulations.

### 3.2: Numerical tools

The simulations presented in this report have been run in a Ubuntu 12.04 operating system, and different programming languages have been used to achieve the tasks

required.

### 3.2.1: Mesh

The very first step of this work consists of the realizations of the two-dimensional meshes. The use of mesh generation techniques, enables the division a complex domain into small elements.

The meshes used for this purpose have been created via a tool called *Gmsh Mesh Generator* (GMG). In order to produce the FE mesh, GMG needs to compile an input text file written in the programming language C++. The extension of these files is .geo, and one file has to be prepared for each mesh. The contents of these files are the vertices of the mesh geometry, the length of the lines that connect the vertices and the amount of elements desired on each side of the beam. However, to better reach the goal of this Thesis, a refinement in the meshes has been done in the central zone. Thus, the global 2D mesh appears like a composition of two different meshes, see Figure 3.2.

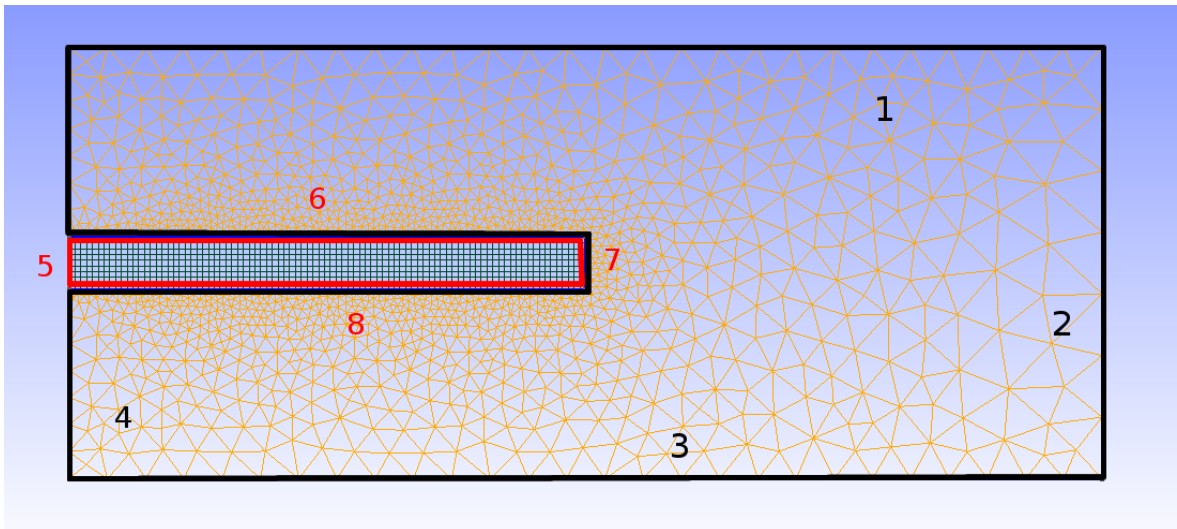


Figure 3.2: The bold black line represents the inverse-C-shaped mesh and it contains triangular elements. The bold red line represents the refined mesh and it contains squared elements. The two mesh are unified in order to obtain one overall mesh. (The numbers represent the sides of the beam ad they will be used as references for the Table 3.2).

A first part, made with triangular bigger elements, in which the loads will be



applied. A second part, fitted in between the other one, made with four nodal fine square elements.

An algorithm has been implemented to link the two surfaces so that the final beam consists of one unique surface. Once the surfaces are connected and the input file is ready, GMG creates automatically the discretization of the domain (see Figure 3.3).

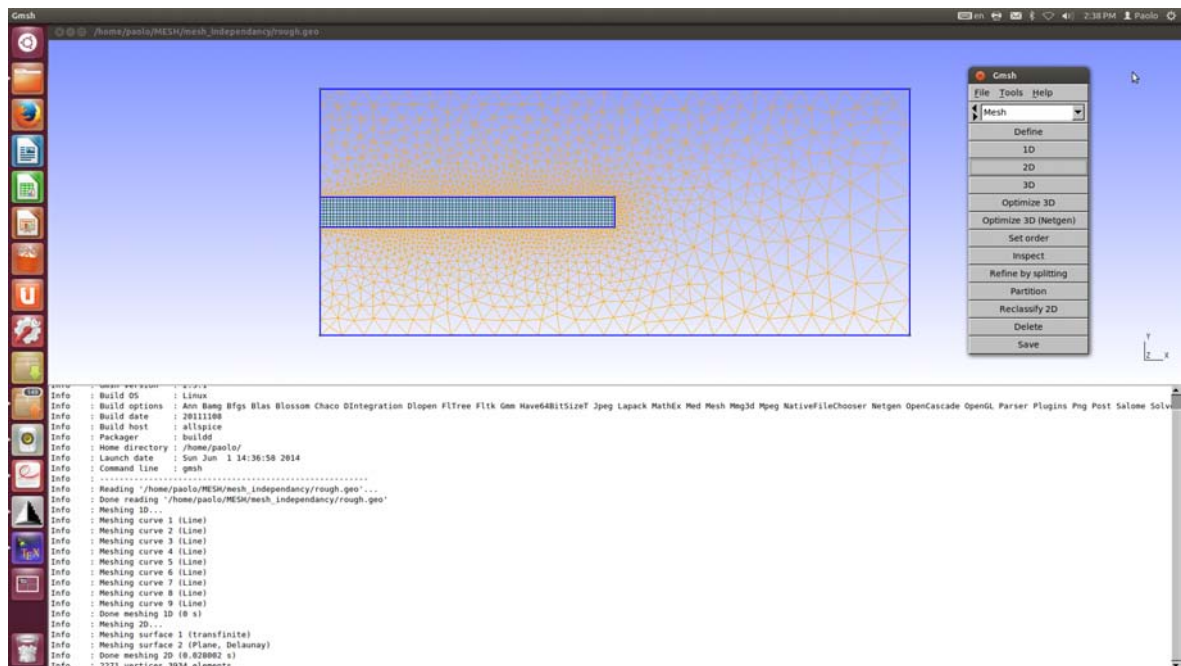


Figure 3.3: One of the meshes used during simulations. The refined zone in the middle, where the initial crack is placed, is coupled with the roughest part. This 2D mesh has 2271 vertices and 3934 elements.

The zone of major interest in the mesh is surely the central one, where the square elements are allocated. The central region is made of a finer mesh, since fracture growth occurs here. Moreover in this part, in the middle of the vertical left side, the initial discontinuity is placed. The choice of making squared elements in the zone of the discontinuity is strictly linked with the mathematical model of the cohesive zone, illustrated in the previous Chapter. In fact, since the length should be at the least equal to two or three elements, it is worth having squared elements instead of triangular ones. Furthermore, because of the symmetry of the beam created and of the loads applied

at the nodes, it is already known that the crack will propagate in horizontal direction ( $0^\circ$ ) and triangular elements may cause some problems to the crack path.

It has been shown that taking the stress state obtained from a temporary sample point at the tip of the discontinuity gives inaccurate results (e.g. [76]). A better approach to determine the stress state in the tip is by using a non-local approach using a Gaussian weight function. In literature (e.g. Wells and Sluys [105]; see also formula 2.75) many Authors have taken the  $l_a$  parameter as approximately three times the typical element length  $l_e$ .  $l_a$  being a length scale parameter defining how fast the weight factor decays as a function of the distance between the integration points and the crack tip. A disadvantage of the approach is that the average stress is significantly smaller than the actual stress at the tip. As a result, the discontinuity will be extended slightly late. For these reasons, the elements have been chosen to be squared, so that the three-times-criterion can be better respected in each simulation.

Several meshes have been created in order to adequately investigate the research topic, however each mesh uses the same boundary conditions for every simulation. Hence, the only things that change are the dimensions, and consequently the number, of the elements inside the beam.

### 3.2.2: Numerical model

The numerical model is programmed in Dawn, a numerical tool developed by Remmers *et al.* [76]. Dawn is build on the Jem/Jive finite element toolkit developed by Habanera.

The numerical implementation of the cohesive zone, and all the input files containing the parameters about the materials, are written in C++. In this project the number of elements in the mesh is upper bounded since the administrator of the central server did not allow to build meshes with a too high number of elements. For instance, simulations with nearly 130000 elements had been killed by the administrator since the process occupied more than 60 Gb of memory and the computation was extremely slow. Almost one month of calculations was not compatible with the time schedule of this Thesis. Suggestions to overcome the problem will be given in the next Chapter.

---

Once the mesh is prepared, in order to start a simulation, three input files need to be managed.

The first one directly descends from the mesh. In this file are listed the nodes, the elements, the node groups (i.e. the nodes in the boundary sides, distinguishing, for instance, the nodes in the middle-bottom side of the beam, the nodes in the corner-bottom, etc..), the node constraints (in this work the only limitations will concern pressures and displacements) and the loads applied to the structure (position, intensity, direction).

Instead, the second file contains the material parameters. Since the personal taste of the Author of this Thesis is focused on Oil&Gas fracturing problems, the porous materials chosen for the simulations are soils. Especially, attention is given to different types of sandstone, varying some physical parameters of interest. The most important information that have to be insert in this file are the values of: Young's modulus, Poisson's modulus, Ultimate Strength, Toughness, Intrinsic Permeability, Dynamic Viscosity, and two Specific Length referred to 2.75. One length is more general, the other one is established in order to circumscribe the zone around the tip and to involve a lower number of integration points during each time step.

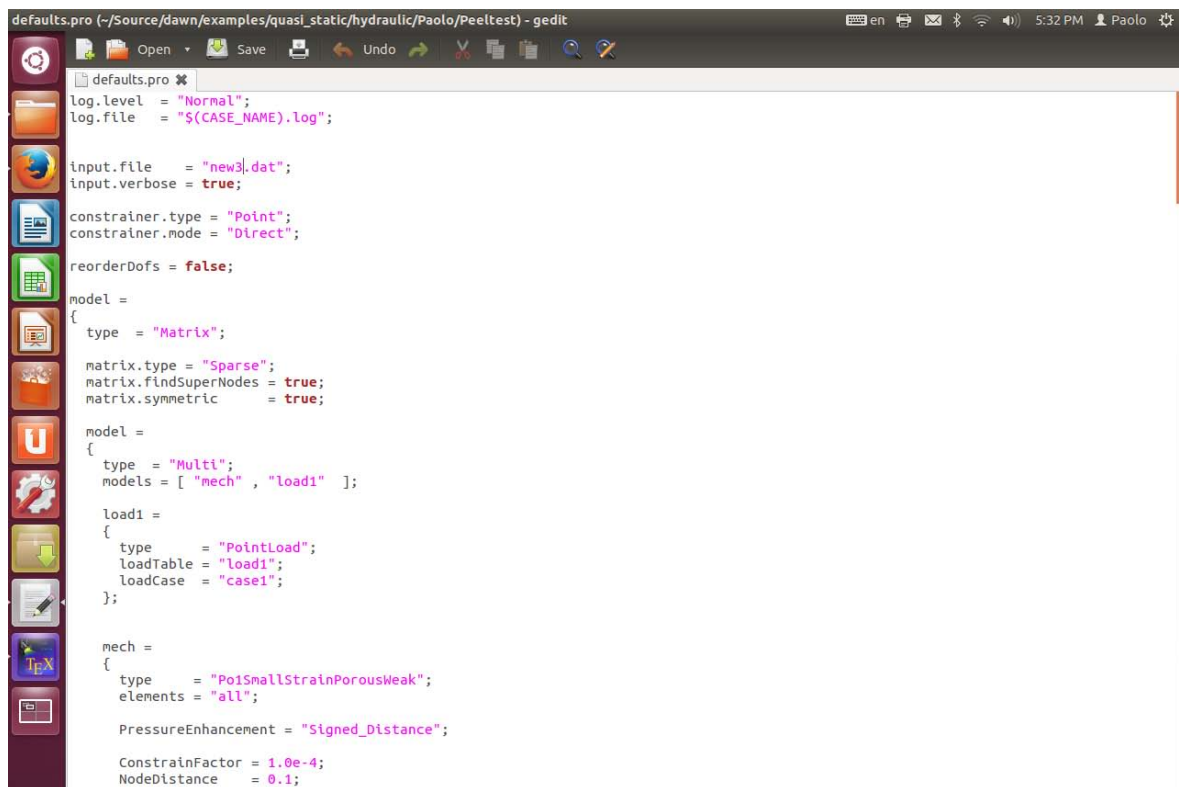
The third file that has to be compiled is the so-called defaults file. This is the biggest of the three. It contains all the general choices that will be run by the code. Here all the main information, such as which kind of input file has to be considered or which model should be implemented, are listed. Moreover, in this document are written several additional information that play a key role on the simulations, for example: the location and the dimensions of the initial crack, the velocity used during the pulling process of the material, the interval of time between one integration and the next one. A screenshot of this file is given in Figure (3.4).

### **3.2.3: Matlab and ParaView**

When the simulations are finished, the code gives as outputs different files that can be divided into two groups: the .gnu files and the .vtu files.

The first set of files contains 13 columns of numbers. Each column corresponds to

---



```
defaults.pro
log.level = "Normal";
log.file = "${CASE_NAME}.log";

input.file = "new3.dat";
input.verbose = true;

constrainer.type = "Point";
constrainer.mode = "Direct";

reorderDofs = false;

model =
{
  type = "Matrix";

  matrix.type = "Sparse";
  matrix.findSuperNodes = true;
  matrix.symmetric = true;

  model =
  {
    type = "Multi";
    models = [ "mech" , "load1" ];

    load1 =
    {
      type = "PointLoad";
      loadTable = "load1";
      loadCase = "case1";
    };

    mech =
    {
      type = "PoiSmallStrainPorousWeak";
      elements = "all";

      PressureEnhancement = "Signed_Distance";

      ConstrainFactor = 1.0e-4;
      NodeDistance = 0.1;
    };
  };
};
```

Figure 3.4: In this picture a part of the defaults file can be seen. The file, written in C++, contains a list of commands that have to be written in order to start the simulations.

a particular parameter of interest (e.g. position of the crack in the beam, pressure in the crack). There is one .gnu file for each time step expected in the simulation. The longer is the simulation (i.e. the bigger is the end time), the higher will be the number of output files. The parameters that will be considered particularly important for this project will be plotted using Matlab. Matlab is a high-level language and interactive environment for numerical computation, visualization, and programming. The reason why this tool has been used in this work lies in the fact that it reaches solutions faster than usual spreadsheets or traditional programming languages.

The second set of files, on the other hand, have to be read through ParaView. This tool is an open-source, multi-platform data analysis and visualization application. ParaView was developed to analyze extremely large datasets using distributed memory computing resources. With ParaView, the fracture propagation can be seen as well as the evolution of all the parameters of interest on the porous medium. Like for the .gnu

files, also for the .vtu files the code produces one file for each time step.

Several plots and pictures containing the results of the simulations performed will be shown and commented in the next Chapter.

### 3.3: Settings

Mesh independence of the model and, eventually, stepwise propagation are investigated. In order to study the mesh independence, an X-FEM code is used. For the advantage of implementing a X-FEM code is that it works well also with not refined meshes, the leading idea used in this work is the following. Three meshes with identical boundary conditions are created. The only difference is in the number of elements, especially in the refined zone in the middle. Then, the different behaviors will be analyzed, particularly changing some strategical parameters.

The general features of the meshes prepared in this project are listed in Table 3.2. The shape of the mesh is chosen arbitrary.

Table 3.2: List of the boundary values of the beam prepared for the simulations. Whereas the boundary values of the mesh will be kept constant, the size of the elements inside the beam will vary. Each side of the beam has been identified with a number. See also Figure 3.2 for references.

Side	Black Line	Red Line
1 = 3	60000 <i>mm</i>	
6 = 8		30000 <i>mm</i>
2 = 4	25000 <i>mm</i>	
5 = 7		3000 <i>mm</i>

The reason for using *mm* in the beam, lies in the fact that if *m* were used, the difference in the orders of magnitude in the stiffness matrix would have been too high (e.g. Young's modulus:  $10^9$ , permeability:  $10^{-15}$ ). While using *mm* this gap can be reduced.

## 4: Numerical simulations: results

### 4.1: Physical behavior or numerical artifact?

It is difficult to exactly predict how fractures propagate under thousands of meter of soils during hydraulic fracturing processes. Even in the field, by using instruments for remote data acquisition, is rather difficult to obtain the evolution profile of the cracks. Thus, the numerical modeling of their behavior is a research topic.

In the last years of studies, the research groups from the Technical University of Eindhoven and the University of Padova achieved similar results by means of completely different techniques. Both groups observed a stepwise behavior of the fracture during its advancement in the soil (or the material involved in the study) through FE simulations.

However, the scientific community did not have paid much attention on this feature in the past decades, that is therefore still a relatively unknown argument. Does the fracture propagate following a stepwise behavior or is it a numerical artifact?

It has been recently demonstrated, by means of experiments, that mode I crack propagation in hydrogels is stepwise [71]. However, no experimental data can be found in literature concerning low permeable porous materials such as shale rocks or sandstone rocks. In fact, it is difficult to reproduce in laboratory the exact *in situ* conditions of these rocks, especially the fully saturation of the material (J.M.R.J. Huyghe, personal communication). Moreover, an accurate numerical description of the phenomenon is still missing.

The main idea that will be followed in this FE Analysis work, consists in comparing the results obtained by testing three different meshes with a mode I crack propagation. If a mesh-independent behavior of the fracture will be seen, this could lead to conclude that there is a physical stepwise advancement in the tested material.

Therefore, in the next sections of this Chapter, the performances of the numerical model used in this Thesis, to try to give an answer to this problem, will be shown by several fracture simulations.

## 4.2: Solid

Before skipping directly to the porous problem, a study on a solid material has been done. This part of the work chronologically represents the first period of simulations. Although the results are not particularly interesting for the aim of the Project, this period was extremely useful for the *calibration of the model and the parameters*.

In fact, after having run different tests, it was possible to establish the definitive setup of the material's properties.

Moreover, a threshold of reliability for the *number of elements* in the mesh has been defined. Even if there were no problems for the convergence of the code with a number of elements that was higher than 10000 elements (this number involves both squared and triangular elements), the simulations took too much time with respect to the time schedule of this work. Therefore, it was reasonably determined that the most refined mesh would not have had more than 11000 elements. Although, it must be specified that typically the computational costs are defined not by the number of elements but by the degrees of freedoms associated to them.

A *continuous pressure profile* across the crack is accounted for. Kraaijveld [55] already tested such pressure for ionized porous materials. However, the stepwise advancement in Mode I propagation was difficult to see since the continuous pressure profile only works for sufficiently smooth meshes. On the other hand, using a very refined mesh, the advantage of implementing X-FEM, that allows the utilization of a quite rough mesh, is lost. Hence, dealing with the stepwise progression of the crack in mode I, this is only possible with finer meshes [89].

The choice of the *squared element sizes* in the central region of the mesh is based on a mathematical criterion. The length of cohesive elements is chosen so that the fracture process zone is discretized with adequate resolution, and the need for numerical convergence is satisfied. In fact, since the cohesive length should be two or three

---

times the element size, this value is established by using the following equation:

$$R_c = \eta \frac{E' G_c}{(T_{ult})^2} \quad (4.1)$$

Equation (4.1) was also used by Khoei *et al.* in 2010 [53]. Here,  $R_c$  is the length of process zone,  $G_c$  is the specific fracture energy,  $T_{ult}$  the tensile strength,  $\eta$  a constant equal to  $\pi/8$  according to the Barenblatt cohesive theory [13] and  $E'$  the effective elastic modulus defined as  $E$  for plane stress and  $E/(1 + \nu^2)$  for plane strain problems.

According to this formula, and choosing the following parameters:

- $E = 18 \cdot 10^3 \text{ MPa}$
- Tensile Strength =  $T_{ult} = 9 \text{ MPa}$
- $\pi/8 = 0.3925$
- Toughness =  $G_c = 11.46 \frac{\text{N}}{\text{mm}}$

The length of the process zone (see also Figure 4.1) reads:

$$R_c \simeq 1000 \text{ mm} \quad (4.2)$$

Recalling that the element size  $\Delta x$  is related to  $R_c$  by:

$$\frac{R_c}{3} = \Delta x \quad \Delta x = 333 \text{ mm} \quad (4.3)$$

This number represents the element size of the coarsest mesh prepared. The *rough mesh* contains 3844 elements. The refined central zone contains 90 elements squared elements along the horizontal side and 9 squared elements on the vertical one. The other two meshes used for the simulations have different elementary sizes and in particular dimensions decrease. The so-called *medium mesh* has  $\Delta x = 250 \text{ mm}$ , 5262 elements and 120x12 squared elements; while the *smooth mesh* has  $\Delta x = 150 \text{ mm}$ ,

---



10148 elements and 200x20 squared elements in the strategic zone.

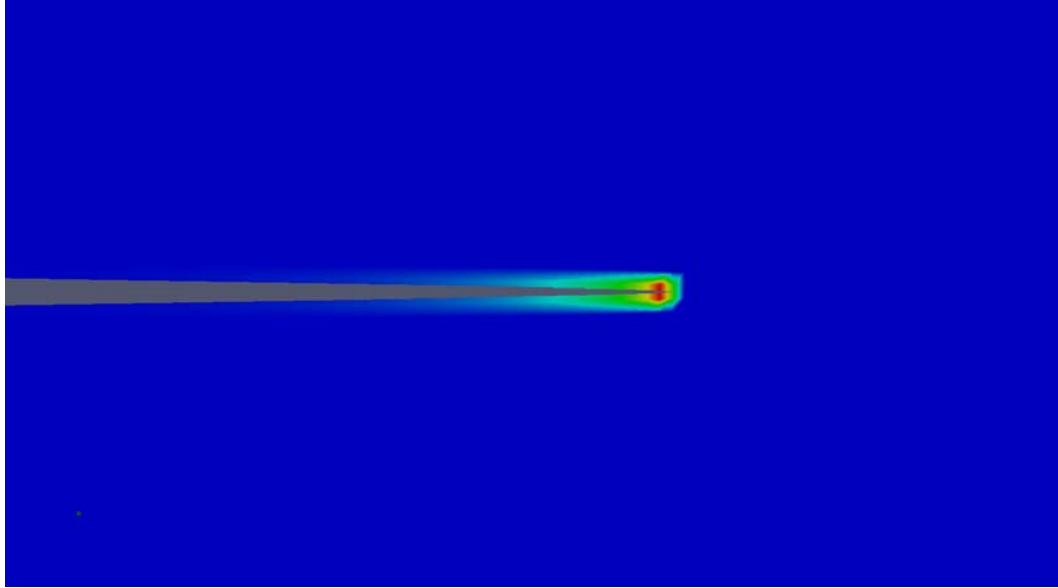


Figure 4.1: In this Figure, the cohesive traction zone obtained in the simulations is shown. The highest traction values can be detected at the crack tip, as foreseen by the theory. The cohesive traction values represent the cohesive length. As it was calculated previously, the area where the cohesive zone plays its role is just around the crack tip. In this image, the length of the process zone is equivalent to three rough squared mesh elements.

The choice of taking such high values of  $\Delta x$ , compared to the ones commonly used in literature, is due to the fact that the limiting values for the size of a fully developed fracture process zone, range from 0.3 to 2  $m$  for concrete and similar quasi-brittle materials [53], like sandstone. Hence this value of  $R_c$ , in order to have the most realistic simulations.

Finally, an investigation about the *velocity of the prescribed displacements* has been done. The prescribed displacements can be seen as a continuous pulling load applied at some predefined nodes. The magnitude of the loadings applied in the nodes of the structure heavily affects the response of the material. The loadings are related with

the prescribed displacement  $u$  by means of the linear relation:

$$u = v \cdot \Delta t \quad (4.4)$$

where  $v$  represents the velocity of the displacements and  $\Delta t$  is the time step.

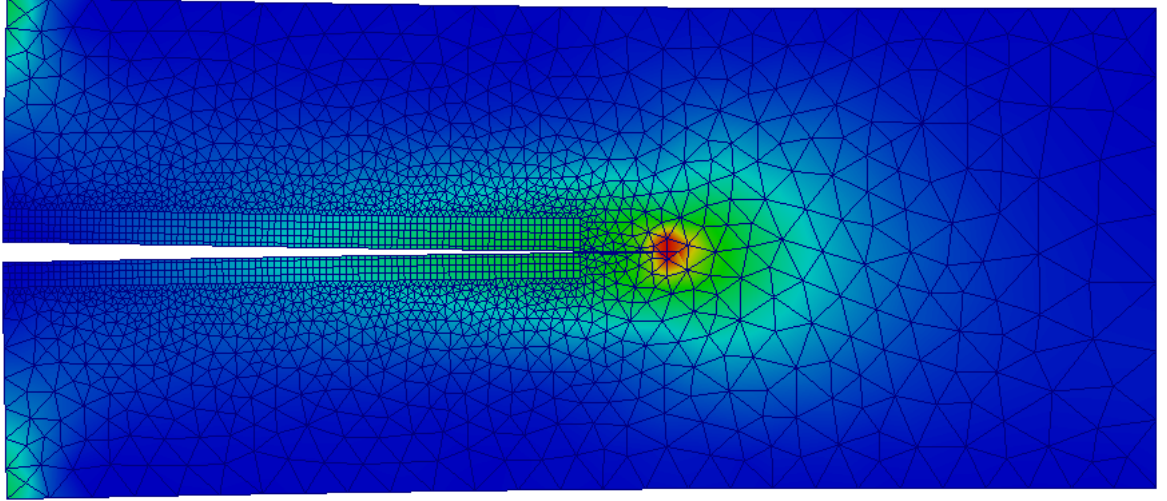


Figure 4.2: Influence of the pulling force on a solid beam. Here, one of the simulations in which the initial crack directly jumps over the refined central zone, due to a too high prescribed displacements. The distribution of the Maximum Principal Stress is illustrated.

In this work  $\Delta t = 1s$  is chosen for the simulations, since it comes from:

$$\Delta t > \frac{\Delta x^2}{EK} \quad (4.5)$$

where  $K = \frac{K_{int}}{\mu}$  is the ratio between the intrinsic permeability and the dynamic viscosity. This criterion is always verified and for every mesh. The displacements are assumed to be constant, without interruptions or jumps, during their development from the first time-step until the end time of the process.

Without an adequate pulling force, the fracture cannot propagate or maybe it starts propagating and then suddenly stops. On the contrary, if too much displacement is imposed to the structure, the process is not developed in the aimed way: which means, with moments of quiescence and rapid advancements in the refined mesh during

fracture propagation. In the second scenario, in fact, numerical simulations show that the fracture can even jump directly after one single step outside the refined region of interest. An example of this wrong failure mechanism is given in Figure 4.2 from the simulations.

### 4.3: Porous

During the simulations with the porous medium, pressure values at every side of the beam are equal to zero ( $p = 0$ ), which means that water is allowed to flow in and out from the beam without any kind of restriction. Therefore, free drainage is assumed at every side of the beam. Boundary conditions are shown in Figure 4.3.

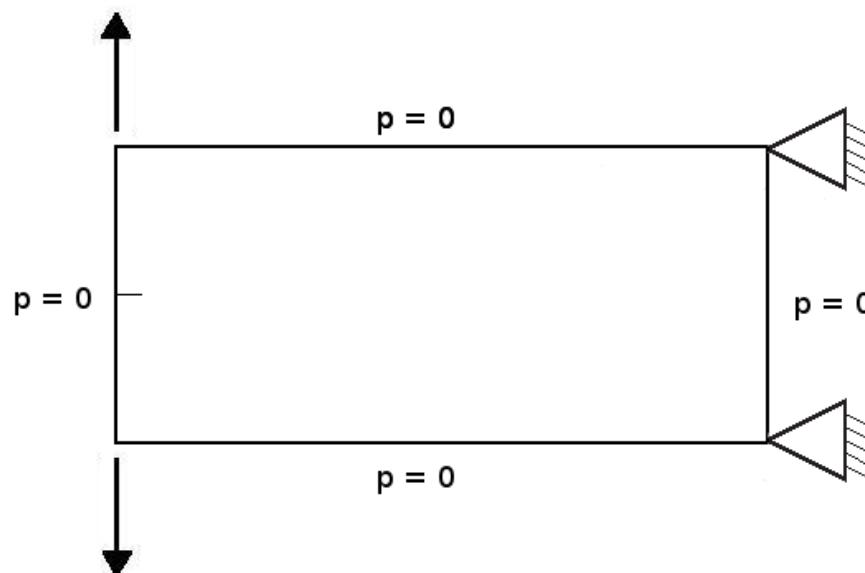


Figure 4.3: Boundary conditions of the beam assumed during simulations considering a porous medium. Two equal forces applied in opposite direction allow the initial crack propagating.

A consolidation process at the tip of the crack as a mechanism for the stepwise propagation is accounted for. The crack is preceded by a cohesive zone to account for damage ahead of the tip. The stress state at the crack tip of a Mode I crack is first carried by the fluid. This, results in a negative pressure and, consequently, in an

attraction of fluid towards the crack tip itself. Hence, fluid is attracted to the crack tip, resulting in progressive transfer of the tensile stress from the fluid to the effective stress of the solid.

In order to enhance the visibility of a stepwise behavior, a term  $\lambda$  is introduced in the code. This is a numerical trick for modifying the velocity of the displacements. Hence  $\lambda = F \cdot \Delta t$ , where  $F$  represents a factor for magnifying the time effects. Therefore, introducing this term, also the end-time must be changed because of Equation 4.4. Which means that for reaching the same prescribed displacement, simulation times vary with respect to lambda. Thus, using different words,  $\lambda$  represents an *éscamotage* for lowering (if  $\lambda < 1$ ) the velocity of the prescribed displacements.

An example that includes a prescribed displacement of  $15mm$  is given. The influence of different values of  $\lambda$  will be investigated, in particular:

- $\lambda = 0.3$       end time = 50 s
- $\lambda = 0.1$       end time = 150 s
- $\lambda = 0.05$      end time = 300 s

In the following plots some general notations will be used and here are briefly recalled:

- *time* = simulation time [s]
- *d* = magnitude in vertical direction of the applied displacement [mm]
- *intf* = reaction due to the displacement in that node [N]
- *tip0x* and *tip0y* = tip locations on *x* and *y* axis respectively [mm]

In Figure 4.4 a comparison between the rough mesh and the smooth mesh is given. Especially, attention is focused on the influence of  $\lambda$  parameter. A time versus reaction force plot will be therefore analyzed. The general trend seems to be similar for the three different curves, with a straight growing line up to the peak, and a curved decreasing tail. The more the time needed to the nodes of the beam to reach the

---

prescribed displacement is increased, the more the time needed to the whole process to occur assumes high values. In other words, if lower traction forces are applied at the nodes, the time needed to achieve the prescribed displacement will increase. The peaks of the curves are in the same range of magnitude both for  $x$  and  $y$  axis either for rough and smooth mesh, while differences can be seen at the end of the tails. Here, the curves reach lower values with the rough mesh. Moreover, a general stepwise trend of the second part of the curve (from the peak to the right side) is detected. This particular behavior is more significant by lowering  $\lambda$  values. Furthermore, this effect is more visible in the rough mesh than in the smooth one.

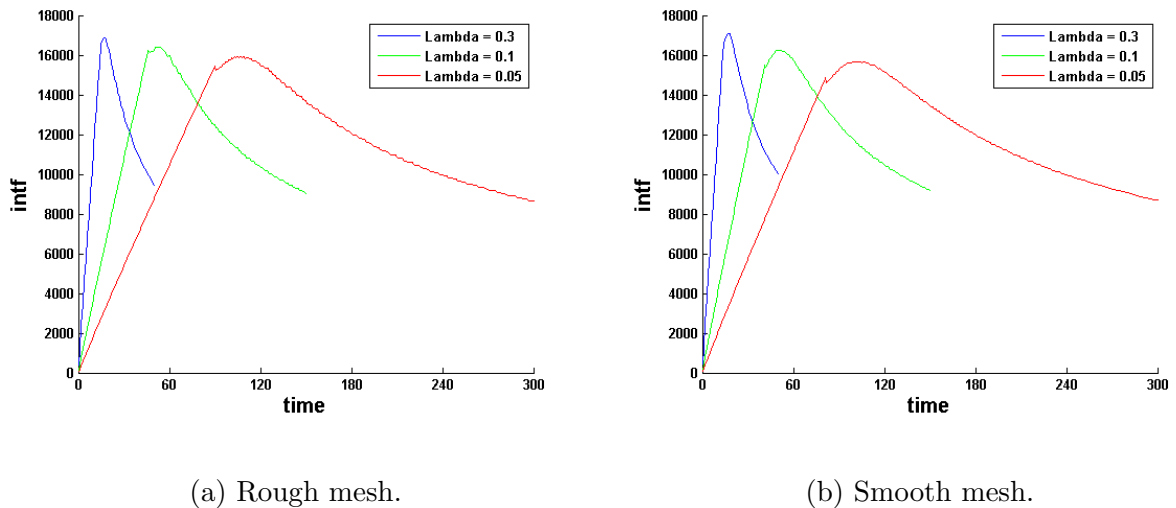
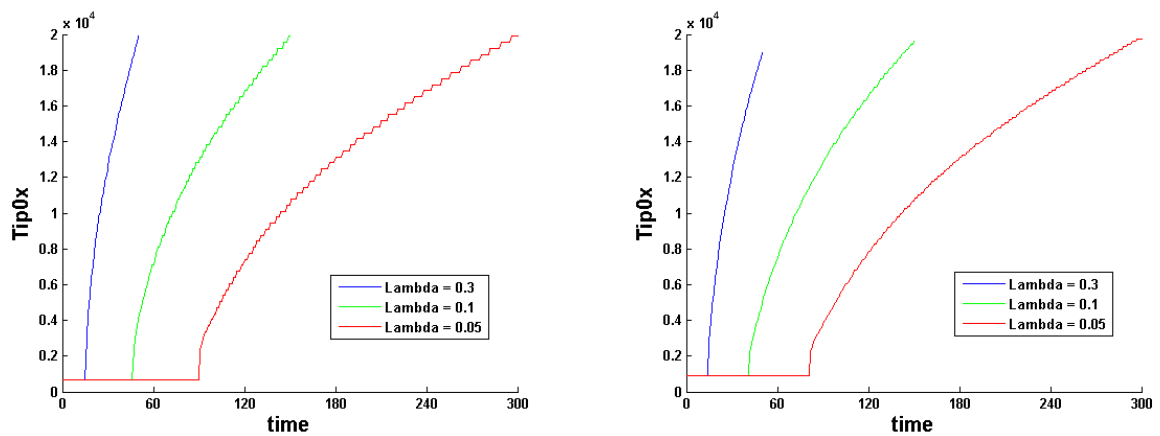


Figure 4.4: The influence of  $\lambda$  on rough and smooth mesh. In these plots, the comparison between time versus reaction due to the displacement in that node plots. The difference between the two meshes is larger for  $\lambda = 0.05$ .

Similar behavior can be found plotting time versus tip location along the  $x$ -axis (Figure 4.5). Here, again, a shifting of the curves on the time-axis, due to the different end times, can be seen. Analyzing these first four graphs it can be concluded that peeling the beam by using a correction factor  $\lambda = 0.3$  is not sufficiently refined for the goal of this project. In fact, in this configuration, mesh independence features and stepwise advancement cannot be seen since the process is performed with too high displacement

velocity. This gives an indication about which values of  $\lambda$  have to be chosen in order to correctly investigate the consolidation phenomenon and, consequently, the stepwise behavior. Therefore, in the following paragraphs, a value of at least  $\lambda = 0.05$ , or even less, will be accounted for during simulations.

Another plot of interest is represented in Figure 4.6. In this comparison, the impact of the mesh chosen is more remarkable. Even though the peaks of the curves take place in the same position along the  $d$ -axis with the smooth mesh, this is not the case for the rough mesh, in which the more  $\lambda$  decreases, the more the peaks move to the right side of the graph. Moreover, the distance between the different curves is more stressed in the smooth mesh. Also in this configuration, a stepwise behavior can be recognized both in rough and smooth mesh, for  $\lambda = 0.05$ . The possibility of investigating the problem with different meshes definitely gives more detailed descriptions about the on-going processes.



(a) Rough mesh.

(b) Smooth mesh.

Figure 4.5: The influence of  $\lambda$  on rough and smooth mesh. Here the comparison between time versus tip location on x-axis plots. Again, using  $\lambda = 0.05$  and also  $\lambda = 0.1$ , a clear stepwise advancement can be seen, especially in the rough mesh. However, rough meshes can lead to false conclusions about the physical interpretation of the plot. In fact the stepwise behavior seems to disappear in the smooth mesh.

Figure 4.7 shows the results obtained by plotting the displacements on the y-axis

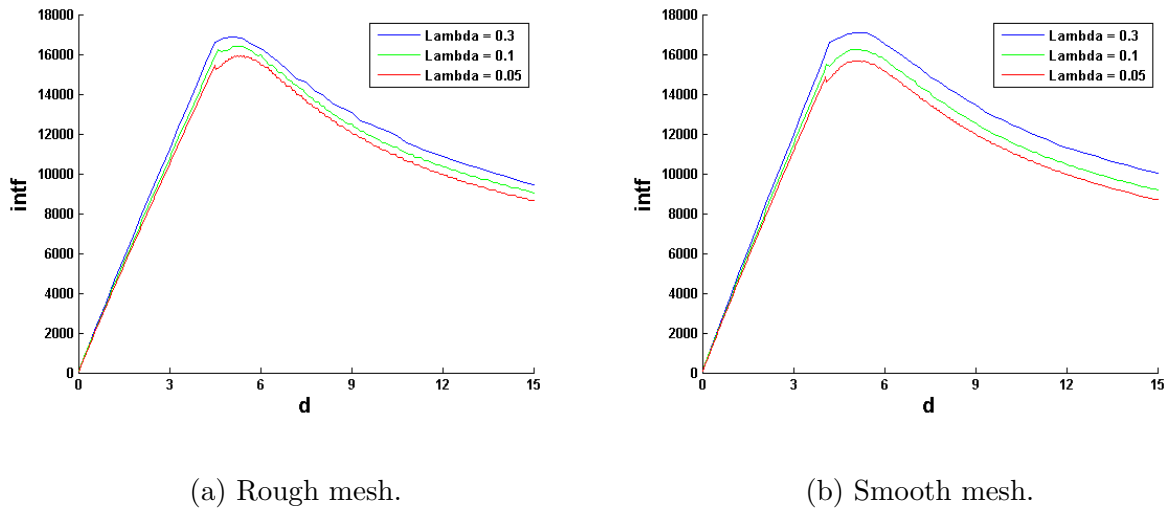


Figure 4.6: The influence of  $\lambda$  on rough and smooth mesh. In these graphs, the comparison between magnitude in vertical direction of the applied displacement versus reaction due to the displacement in that node plots. Rough mesh is not as good as smooth mesh in capturing the differences in using several  $\lambda$  values.

versus the location of the tip on the x-axis. This graph is particularly important because it clearly shows the presence of a stepwise advancement in fracture propagation. Referring to the rough mesh, the three curves are almost flattened into one unique curve. Furthermore, even if in the curve plotted with  $\lambda = 0.3$  there is no a stepwise progression, this can be seen either from  $\lambda = 0.1$  and from  $\lambda = 0.05$ . Slightly different are the results in the smooth mesh. In fact, analyzing the problem in a more detailed way, there is a divergence of the curves, although the general trend is the same. Moreover, here for  $\lambda = 0.1$  the stepwise curve smoothly starts disappearing. Instead, with  $\lambda = 0.05$ , stepwise behavior can be seen again but the steps are smaller than in the rough mesh.

The last plot (Figure 4.8) is particularly interesting if compared with Figure 4.4. Here attention is stressed on the threshold value of the force needed to the fracture to start propagating. Therefore it can be seen that changing  $\lambda$  also the peaks of each curve change. These values physically correspond to the points of instable equilibrium after which the fracture starts propagating if the continuous load is still applied. When

$\lambda$  decreases, also the *intf* assumes smaller values and the tip of the crack advances throughout a stepwise trend. This behavior can be seen especially in two different zones. Looking at the graph, this has a higher effect between *Tip0x* values from 0.3 to 0.5 and from 1 to 2. Again, rough mesh seems to give more visibility to this phenomenon.

At the end of this  $\lambda$ -analysis, it has been understood that the velocity of the prescribed displacements has an influence on the investigation of the stepwise advancement of fractures. In particular, it can be concluded from this study that the more  $\lambda$  decreases, the more the stepwise effect can be detected. Hence, in the following simulation that will be illustrated, a value of  $\lambda = 0.01$  will be assumed. Thus, it has been chosen to perform longer simulations in favor of more detailed results concerning the stepwise property.

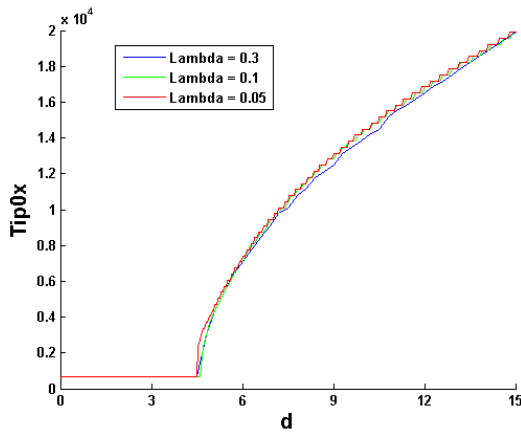
The results are shown in Figure 4.9. The three graphs plot the same parameters that have already been described before. The difference lies in the fact that here the value of  $\lambda$  is kept constant, while the different meshes are put in one single graph.

From a global point of view, rough, medium and smooth meshes assume the same trend in all the three plots. Especially the solution seems to converge at the end of the processes, which means far away from the initial crack at time  $t = 0$ . Therefore, the meshes present more differences at the beginning of the delamination process. As far as the stepwise advancement of the fracture is concerned, all the three meshes show this evidence. This is an indirect confirmation that assuming  $\lambda = 0.01$  is a good testing value. Referring to the third graph of Figure 4.9, it can be seen that the steepness of the loading straight line is higher with the smooth mesh, while rough mesh shows the less steep line. On the other hand, the rough mesh reaches the highest peak values and this peak occurs later than in the smooth mesh. Medium mesh is always placed in between the two other meshes.

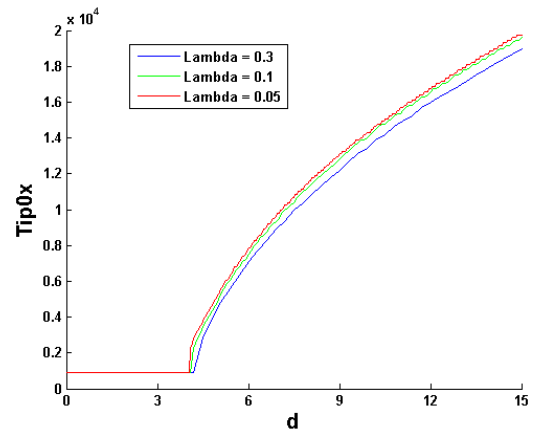
Another important consideration concerns the interval of time between one step and its following. In fact, especially referring to the second graph of Figure 4.9, the more the time increases, the more the pausing time between one jump and the following augments. This is true for every mesh. Physically speaking, it means that when the

---



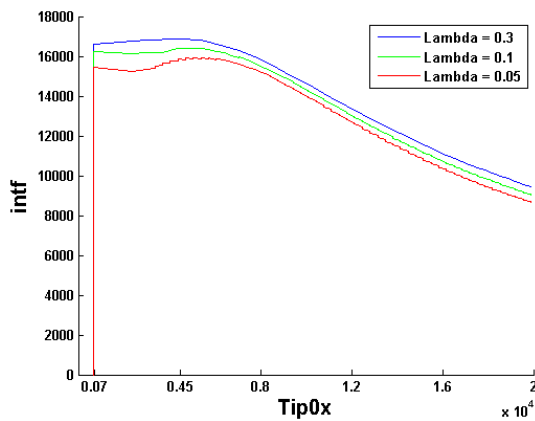


(a) Rough mesh.

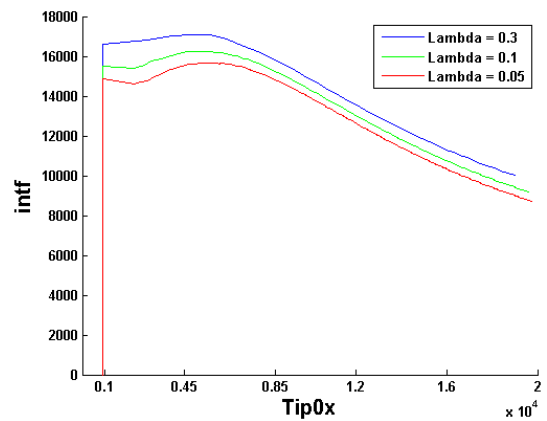


(b) Smooth mesh.

Figure 4.7: The influence of  $\lambda$  on rough and smooth mesh. Here the comparison between magnitude in the vertical direction of the applied displacements versus tip location on x-axis plots. In the rough mesh it can be seen that the code gives almost the same solution implementing a value  $\lambda$  equal to 0.05 and 0.1, while the smooth meshes can capture small differences.



(c) Rough mesh.



(d) Smooth mesh.

Figure 4.8: The influence of  $\lambda$  on rough and smooth mesh. Here the comparison between tip location on x-axis versus reaction force plots. A value  $\lambda = 0.3$  is not able to properly define the process (the peak in the curve is barely visible).

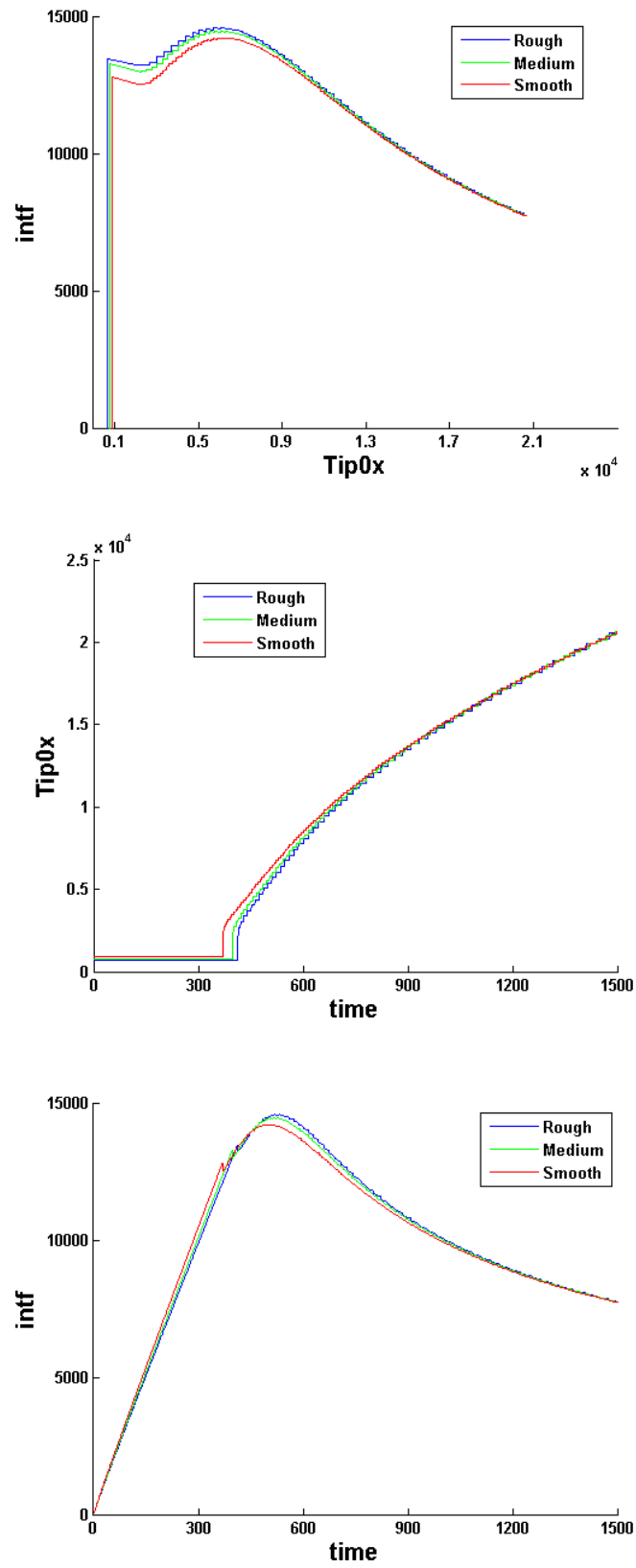


Figure 4.9: Comparison between rough, medium and smooth mesh using  $\lambda = 0.01$ .

crack starts its propagation into the material it will have a sudden diffusion through several elements in a short interval of time. Then, a general decrease of the steepness of the three curves can be seen at the end of the process. Hence, at the end of the fracture process, the jumps will be once in a while. For this reason in the Thesis, in order to better analyze the mesh independence of the problem, fractures at the end of the process will be studied.

The previous simulation considered a constant absolute permeability for the fluid fully saturated medium surrounding the fracture. A cubic law was considered for the permeability within the fracture. This has been stated for a long time in the case of laminar flow (or Couette flow) through open fractures and its validity has been confirmed in the case of closed fractures where the surfaces are in contact and the aperture decreases under applied stress [88].

However, the cubic law (or Poiseuille law) is valid when the fracture surfaces are held open or are closed under stress, without significant changes when passing from opening to closing conditions. This hypothesis is violated during hydraulic fracturing processes, since the presence of proppants and grains of sand reduce the width of the completely opened crack. Moreover, permeability is not dependent on the rock type or stress history, but is defined by crack aperture only.

For these reasons, in this work it was decided to reduce the exponential value that affects the crack opening. Therefore, the cohesive zone permeability still reads a cubic law:

$$K_d = \frac{(\delta_c)^2}{12\mu} \cdot \nabla P_c \quad (4.6)$$

where  $K_d$  is the permeability,  $\delta_c$  is the crack opening,  $\mu$  represents the dynamic viscosity of the fluid. The main difference is that it takes into account a damage model for the cohesive zone permeability that is no more at the power of three but the power of two. This should give more realistic results about the fluid flow especially around the crack tip. Performing several tests, the new implementation brought the important result

---

of seeing the fracture jumping through multiple elements for the first time since the beginning of the simulations.

It has been tried also to do not use a cubic law, but the code gave numerical oscillation problems.

Hence, a study on the influence of the dynamic viscosity and the intrinsic permeability, at this point, is needed.

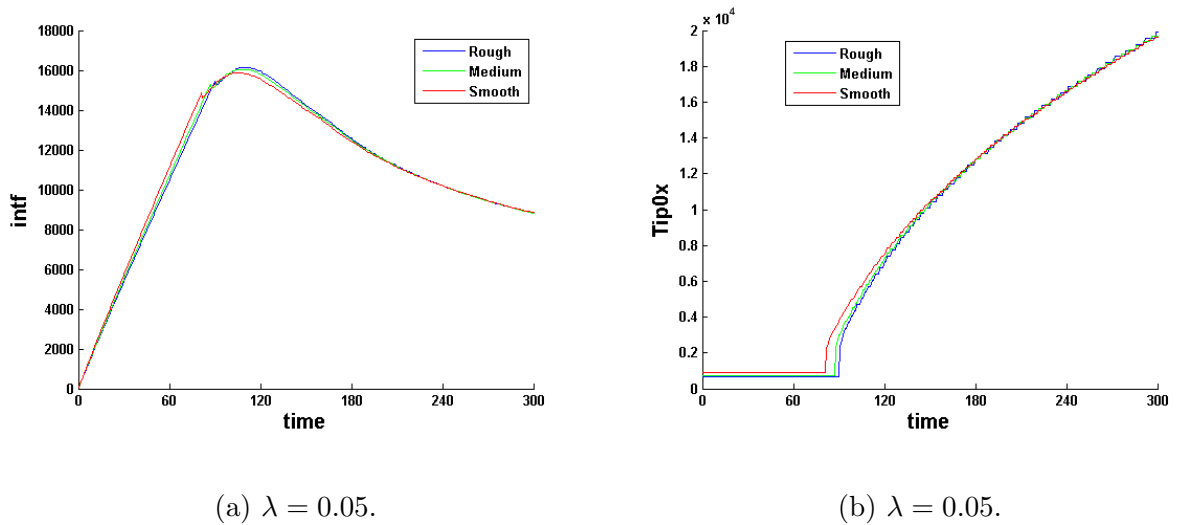


Figure 4.10: Here,  $\lambda = 0.05$  and a new damage model for the cohesive zone permeability are accounted for. This leads to smoother solutions at the beginning of the curve and highlights the jumps of the fracture at the end of the process. Jumps through multiple elements can be seen.

Considering a value  $\lambda = 0.05$  and the new damage model, what can be seen is that the opening assumes a smoother behavior at the beginning, instead during the last cracking moments of the simulations the jumps across multiple elements are more visible. Especially referring to 4.10b this fact can be highlighted. Again, the three different meshes have been tested.

Keeping the ratio between the intrinsic permeability  $K_{int}$  and the dynamic viscosity  $\mu$  constant and equal to  $5 \frac{mm^4}{N.s}$ , several configurations have been tested. Only medium mesh is accounted for. The values used are listed in Table 4.1.

Table 4.1: List of the values for the intrinsic permeability and the dynamic viscosity tested during the simulations.

Dynamic Viscosity $\mu$	Intrinsic Permeability $K_{int}$
$1.0e^{-10} (N \cdot s \cdot mm^{-2})$	$5.0e^{-10} (mm^2)$
$1.0e^{-9} (N \cdot s \cdot mm^{-2})$	$5.0e^{-9} (mm^2)$
$1.0e^{-8} (N \cdot s \cdot mm^{-2})$	$5.0e^{-8} (mm^2)$
$1.0e^{-7} (N \cdot s \cdot mm^{-2})$	$5.0e^{-7} (mm^2)$
$1.0e^{-6} (N \cdot s \cdot mm^{-2})$	$5.0e^{-6} (mm^2)$
$1.0e^{-5} (N \cdot s \cdot mm^{-2})$	$5.0e^{-5} (mm^2)$
$1.0e^{-4} (N \cdot s \cdot mm^{-2})$	$5.0e^{-4} (mm^2)$

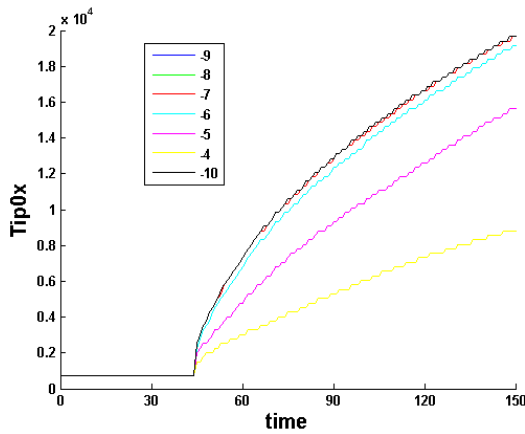
The results are shown in Figure 4.11 and 4.12.

The differences among the curves are very strong. Referring to the trends, and focusing the attention on Figure 4.11b, the behavior of the curves can change a lot. In particular, the more the curve loses its typical shape of a delamination test (i.e. without the peak), the lower is the distance traveled by the crack in the medium. Moreover, for exponential values starting from -6 up to -10, the curves converge into similar solutions. Hence, a more detailed description of these solution-converging simulations have been analyzed. Results are shown in Figure 4.12. Thus, for the following research, a dynamic viscosity of  $1.0e^{-9} N \cdot s \cdot mm^{-2}$ , which corresponds to water at 20 °C, will be used.

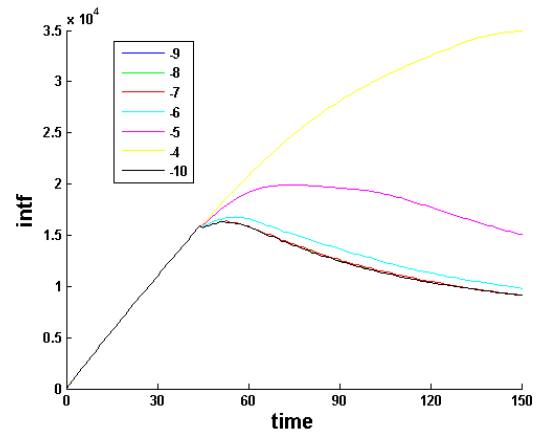
Four more plots (Figure 4.13 and 4.14) show how the intrinsic permeability plays a fundamental role on the correct calibration of the model and how can it changes for different meshes. Especially referring to Figure 4.13b and to Figure 4.13d, the meshes lead to completely different solutions, even though the propagation does not loose its typical stepwise advancement.

Since this moment, no strong argumentations can be given about the mesh independence of the problem, therefore it was decided to create a new mesh, with the smallest possible size allowed for the squared elements: 100 mm. The heaviness of the computation did not allow a further and more refined investigation.

Therefore, the new mesh counts 17702 elements and 12870 vertices. However, in

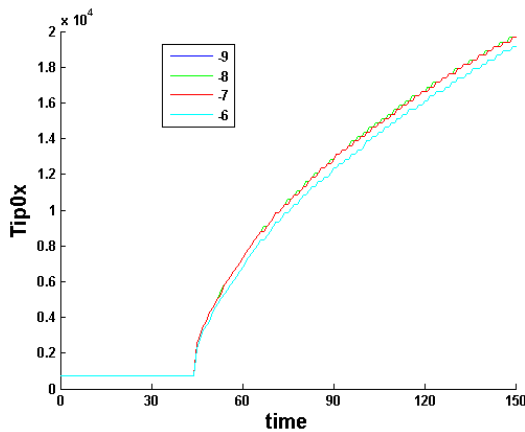


(a) Medium mesh.

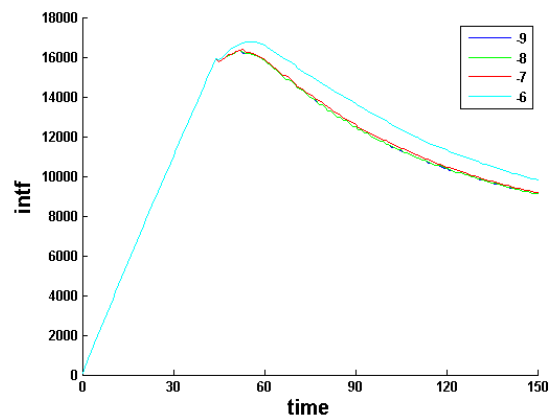


(b) Medium mesh.

Figure 4.11: The two plots above show the influence of the intrinsic permeability and the dynamic viscosity on the propagation of a fracture in a beam under Mode I cracking simulations. (Since the detailed values are listed in Table 4.1, here they are indicated just with the number of their exponential power, that is the same for  $K_{int}$  and  $\mu$ ). The higher is the viscosity of the fluid, the more the fluid needs time to advance, since the tangential friction is more important.



(c) Medium mesh.



(d) Medium mesh.

Figure 4.12: Since the results of Figure 4.11 show a convergence of the solutions to low permeability and low dynamic viscosity values analyzed, a more detailed study on those values has been done with a magnification on the zone of interest. (Again, since the detailed values are listed in Table 4.1, here they are indicated just with the number of their exponential power, that is the same for  $K_{int}$  and  $\mu$ ).

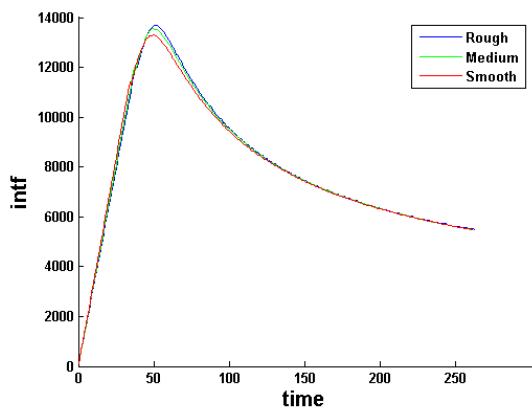
this configuration, the physical phenomenon challenges the numerical scheme. In fact, stepwise growth of fractures in mode I propagation in porous media is difficult to see considering a continuous pressure profile. Moreover the continuity of the problem, needs a sufficiently fine mesh in order to resolve the steep pressure gradients by means of the discretization. On the other hand, the advantage of using X-FEM, that guarantee accurate solutions with quite rough meshes all over the continuum, is lost.

The results obtained seems to go in this direction. A stepwise behavior through multiple elements can be seen, even if the problem should be investigated with a more refined mesh. Sandstone material is studied, and the values reads:

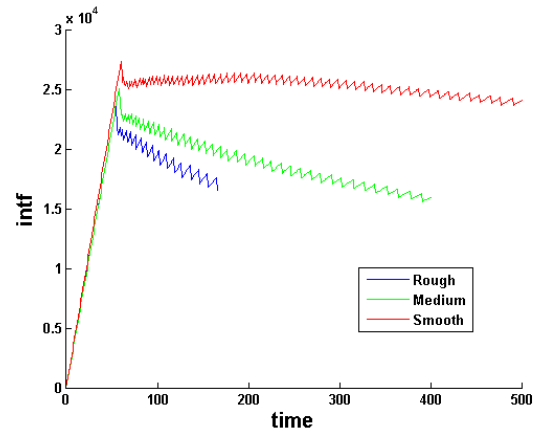
- $K_{int} = 5.0e^{-12} \text{ mm}^2$
- $\mu = 1.0e^{-9} \text{ N} \cdot \text{s} \cdot \text{mm}^{-2}$
- $E_{mod} = 18 \text{ GPa}$
- $Poisson's \text{ Ratio} = 0.275$
- $Tensile \text{ Strength} = 3 \text{ MPa}$
- $Fracture \text{ Toughness} = 11.465 \frac{\text{N}}{\text{mm}}$

What can be observed during a simulation can be divided into different parts. At time  $t = 0$  no forces act in the beam, no pre-stresses are applied into the material, the structure has no initial deformations and a discontinuity is placed on the left side in the middle. Then the boundary conditions are applied (see also Figure 4.3) but the loading needs to overcome a threshold value before the crack starts its propagation through the medium. The first two or three propagations have a bigger entity than the following ones. In fact, later on, the process reach a stable stepwise advancement. Here the pause time (from 7 up to 15 time steps) and the fracture progression (from 2 to 3 elements each jump), see Figure 4.15 and 4.16. Finally, in Figures 4.17 and 4.18 some parameters of interest are shown.

---

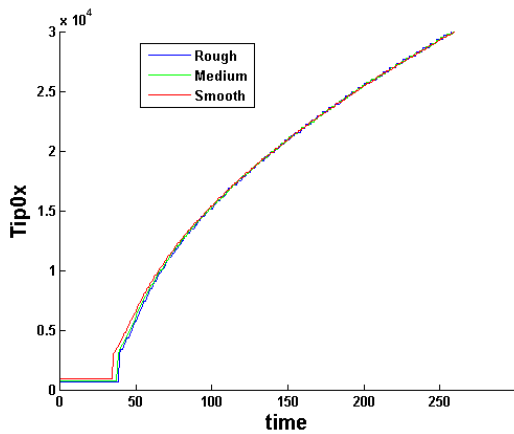


(a)  $K_{int} = 5.0e^{-6} \text{ mm}^2$ .

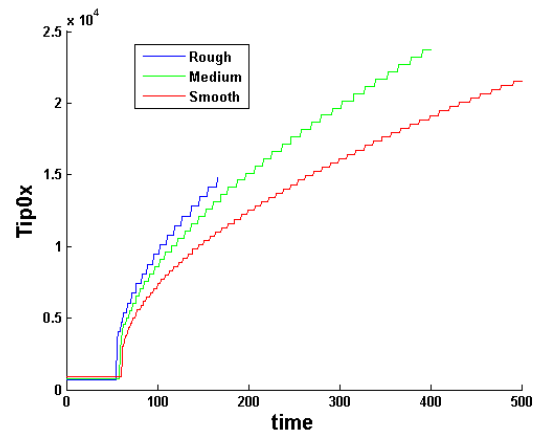


(b)  $K_{int} = 5.0e^{-12} \text{ mm}^2$ .

Figure 4.13: The intrinsic permeability plays a central role on the study of the mesh independence problem. In fact, inadequate values may lead to wrong solutions or misunderstanding scenarios. In these graphs the different behavior of the meshes gives completely different solutions, especially for the less permeable material.



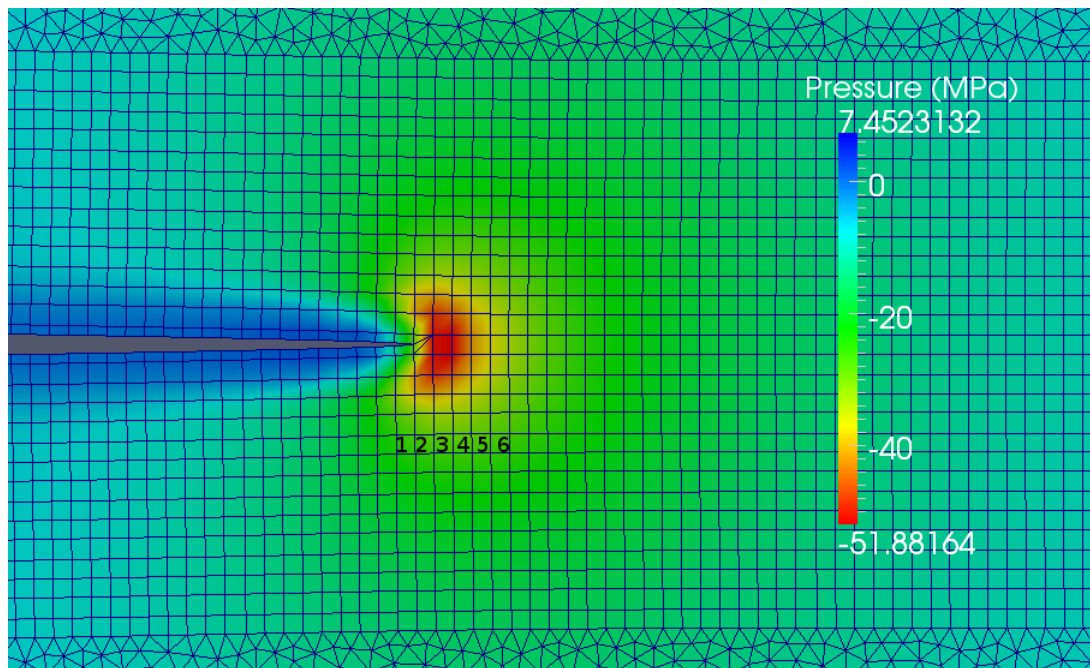
(c)  $K_{int} = 5.0e^{-6} \text{ mm}^2$ .



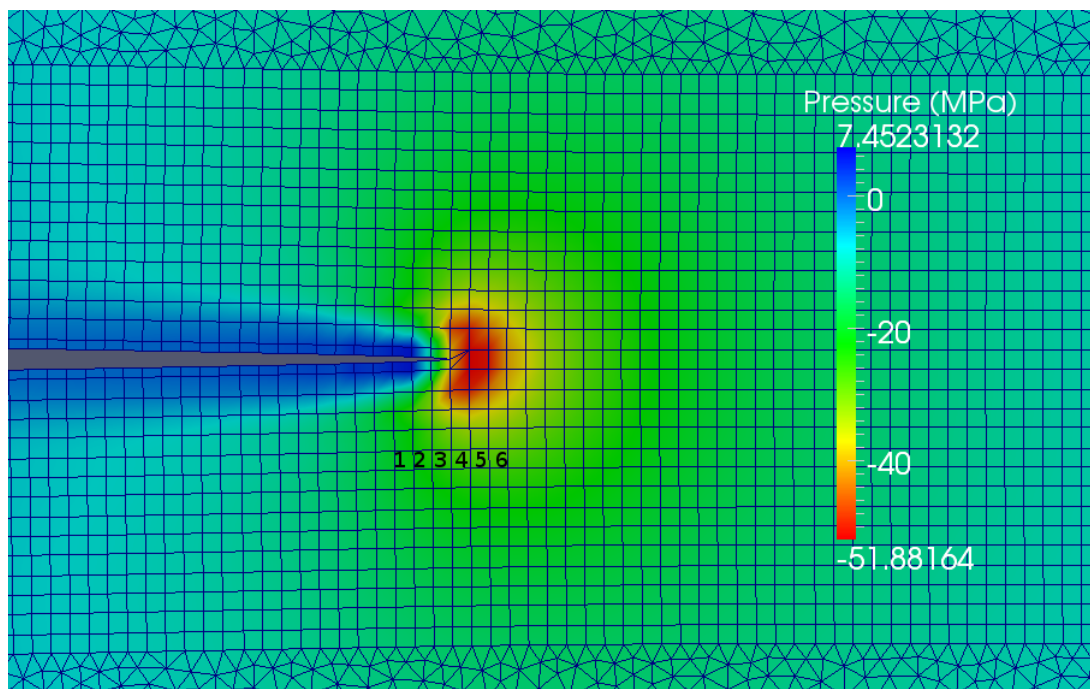
(d)  $K_{int} = 5.0e^{-12} \text{ mm}^2$ .

Figure 4.14: These plots reflect the same aspects already underlined in Figure 4.13. Even though a clear stepwise advancement can be seen in the less permeable material, the influence of the mesh assumes a key role. This is not the case for the more permeable material, since the three meshes present just tiny differences.



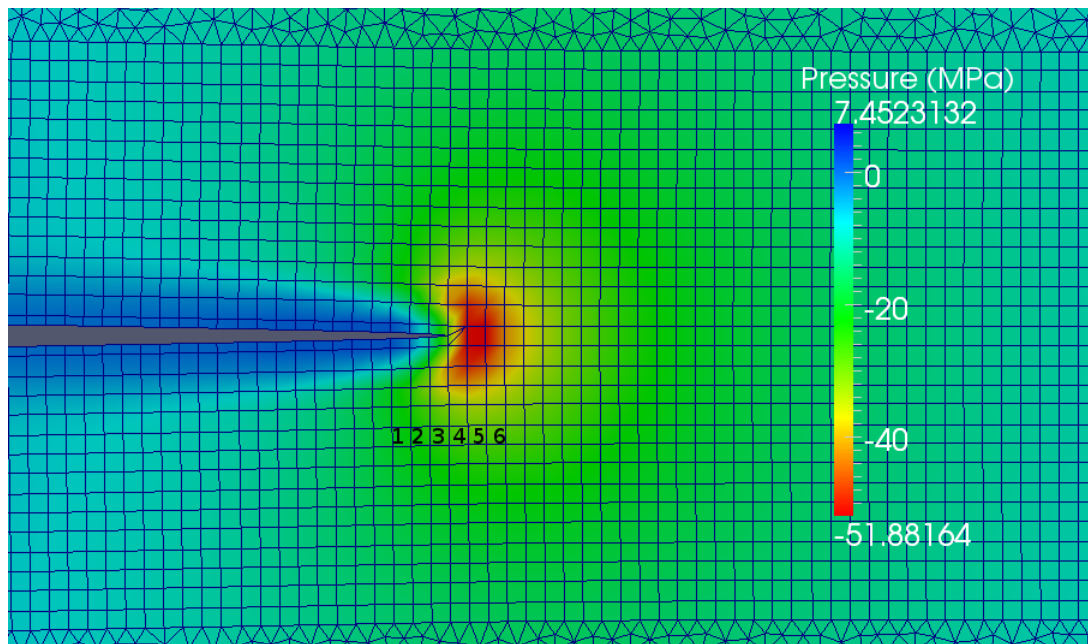


(a) Time step = 327.

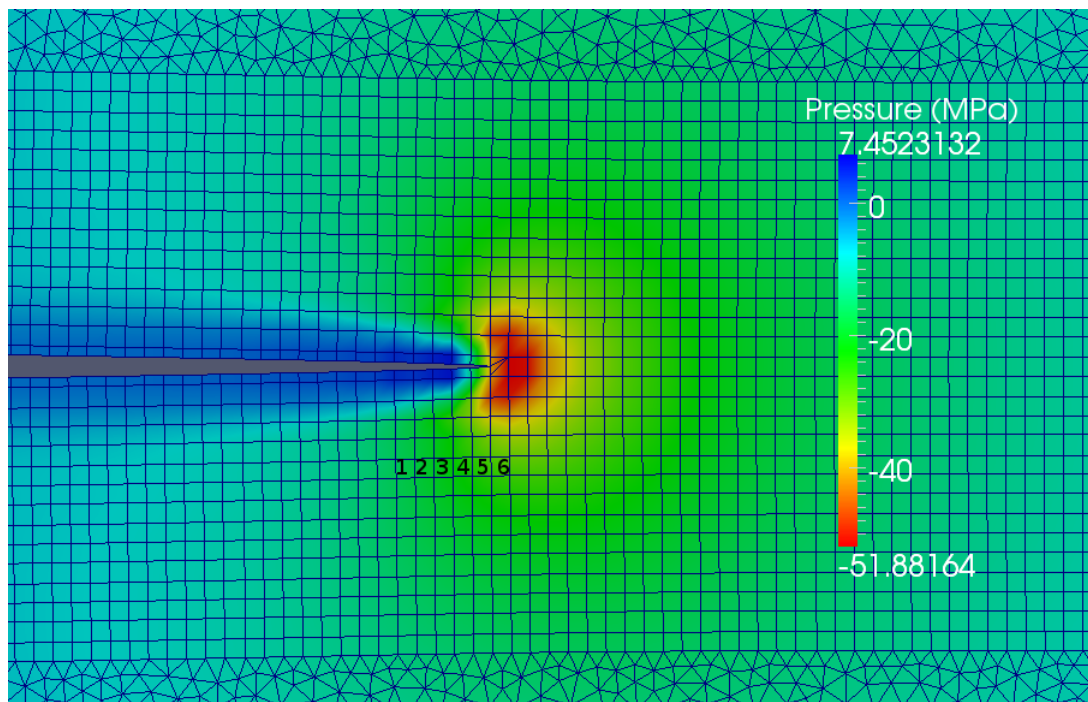


(b) Time step = 328.

Figure 4.15: Starting from a Paraview screenshot of the simulation, numbers have been added below the zone of interest to identify each element. Here in particular attention is focused on the jump of the fracture through two elements, in two following time steps, with a redistribution of the underpressure zone in front of the tip.



(a) Time step = 335.



(b) Time step = 336.

Figure 4.16: Here, attention has to be paid to the time steps in which this phenomenon occurs. In fact, looking at Figures 4.15 and 4.16 together, it can be seen that two following jumps are showed with a pause time in between (from time step 328 to 336). During the quiescence time, the underpressure ahead the crack tip is redistributed in the material.

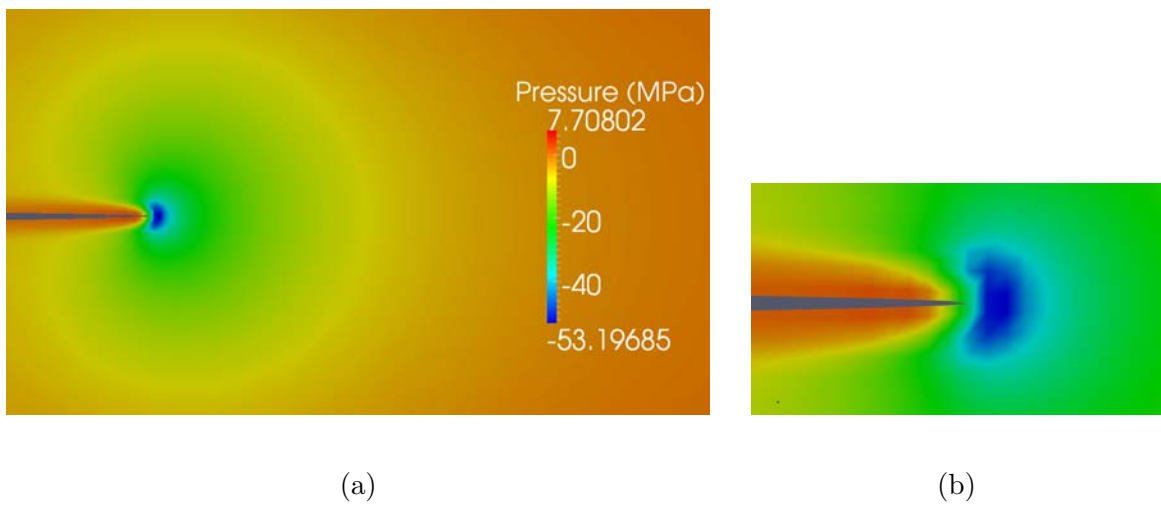


Figure 4.17: Pressure distribution (MPa) for the delamination test at  $t = 250$  s. (a) for a large part of the sample and (b) for a zoom around the crack tip.

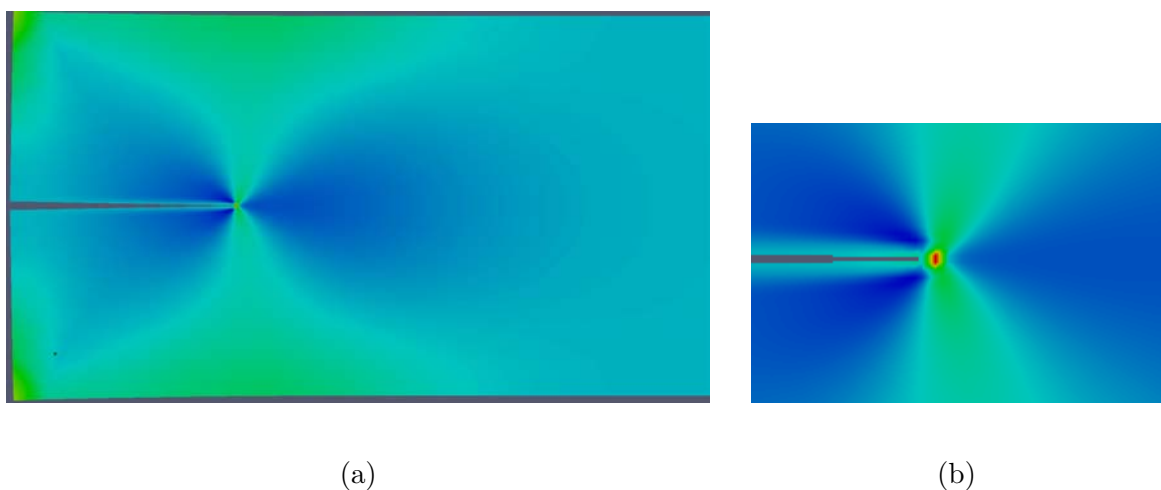


Figure 4.18: S22 (stress on y-plane) distribution at the end of the process. In the first picture (a) an overall view of the beam is given, while in the second one (b) attention is focused on the tip zone.

#### 4.4: Discussion

Numerical simulations in mode I crack propagation (shear traction is assumed to remain zero) of fractures in a fully saturated material are presented. The partition of unity

approach is used to integrate cracks into the FEM. A discontinuity is inserted in the displacement field by enhancing the field with the Heaviside function. The accuracy of the numerical performance has been tested on several benchmarks.

A zero propagation angle was assumed in every propagation step. The results obtained show the presence of a stepwise growth of the fracture along the cracking path. Crack growth (i.e. the extension of the discontinuity) is governed by the stress state at the tip.

When the stress state exceeds the value of the ultimate traction of the material, the discontinuity propagates. Due to the pure mode I fracture conditions, the discontinuity is extended when the maximum stress in tip in the direction perpendicular to the weak interface (i.e. the y-direction) exceeds the normal strength. The presence of a duration of a pause  $\Delta t$  between one jump and the following can be observed. A possible explanation [89] is that an incompressible fluid consolidation comes into play which prevents tip advancement until the underpressures due to the last advancement have been dissipated, and the stress has been transferred again to the solid phase. This means that pressure dips exist after each advancement stage. Instead, during the period of quiescence, the effective stress is below the threshold. Hence, no advancement can be seen. Underpressures keep the crack tip closed, while very high tractions in the cohesive zone try to open the fracture. The stress state is first carried by the fluid, which results in reduced pressures and attraction of fluid towards the crack tip. Crack propagation velocity increased with higher permeability values. In the context of consolidation of the porous material this can be explained as faster tensile stress transfer from the fluid to the solid skeleton in the highly permeable material. The presence of periods of quiescence is in accordance with previous literature [95]. Moreover, the results show an attraction of fluid before the crack tip, while, along the sides of the crack fluid is pushed from the crack into the bulk formation. The influence of the local mass balance is considered. Decreasing the intrinsic permeability, the area of underpressure before the crack tip reduces its dimensions without altering the crack path. When the material is less stiff and permeable, the influence of the fluid becomes more profound and the time needed to resolve the problem is bigger. Upon loading the effective stresses at the

---

crack tip increases. Therefore the influence of the fluid flow on the crack propagation is verified. The extension of the cohesive length through multiple elements is verified as well (see also Figure 4.1).

However, the sudden propagation of the fracture from one time step to its following, can only be seen through two or maximum three elements (see Figures 4.15 and 4.16). While the reason of preparing meshes with different element sizes was to eventually put in evidence a jump through much more elements. Identification of stepwise propagation will be more clear if there is completely no mesh-dependent crack growth. This is why this problem deserves further scrutiny.

Figure 4.4 shows that by lowering the pulling force, the time needed to reach the ultimate strength increases.

Considering Figure 4.6, an indication about the mesh independence of the problem can be detected. In fact, moving from rough to smooth mesh, the peaks of the curves are almost aligned into one single  $d$  value, which means that the mesh is finer enough not to be affected by variations of  $\lambda$ .

Referring to Figure 4.8 the influence of the porous material can be observed. If a solid material was considered, the force needed for the propagation of the fracture (*intf*) would have been the same. Instead, looking at the graphs, the blue line, corresponding to  $\lambda = 0.3$ , needs a higher pulling force, and higher underpressures are detected at the crack tip. On the contrary, applying a lower prescribed displacement (red line) the fluid inside the beam, that initially carries the load, according to the consolidation theory, has more time to transfer the stresses to the solid part. The time of consolidation is approximately coupled to the Young's modulus  $E$  and the hydraulic permeability  $K$  (see Equation 4.5). In the second scenario, the fluid has more time to flow out. The effects are even enhanced in the smooth mesh, since the reduced element sizes can better describe the phenomenon.

However, the general picture of the failure (Figure 4.9) gives some indications that the phenomenon is probably mesh independent. In fact, even though the curves are slightly different, and the smooth mesh propagates earlier, because it better captures the on going process, the general trend is the same and, continuously reducing the mesh

---

---

sizes, it is reasonable to think that at a certain point, below a mesh-size threshold value, there will be no more differences among the graphs. Which means that the phenomenon would be mesh-independent. Unfortunately, further investigation was not possible because of the presence of a certain number of limitations. Therefore, what can be concluded is that, considering a sufficient low velocity for the prescribed displacements and a sufficient fine mesh, a mesh independent problem coupled with a stepwise crack propagation can be seen. The numerical results are qualitatively consistent with the previous experimental work [71].

#### 4.4.1: Limitations, recommendations and future work

The main limitation encountered during simulations concerned the duration of the process. The computational time required by the simulations, especially for very dense meshes, was too high (e.g. the last simulation presented took almost two weeks without any interruption).

A consequence of using the continuous pressure profile is that the element size around the discontinuity must be small enough to capture a pressure jump. This interferes with the main advantage of X-FEM: X-FEM does not require a fine mesh.

Another limitation lies in the code itself. In fact, the discontinuity is not allowed to stop in any part of an element that is not a boundary side (i.e. it cannot stop in the middle of an element, thus stepwise advancement observed, especially in rough meshes, can be misleading because it might not be a physical behavior).

Concerning the numerical implementation, improvements on the numerical calculation times can be made by changing the method on how the average stress is calculated. In the current method the distance between the crack tip and every integration point is calculated and assigned with a weight factor (defined with equation 2.75).

A possible and most important remediation for the first problem illustrated could be the parallelization. This computer astuteness would allow to resolve the problems in a faster way. Parallel computing is a form of computation in which many calculations are carried out simultaneously, operating on the principle that large problems can often be

---

---

divided into smaller ones, which are then solved concurrently (i.e. in parallel).

As far as the future work is concerned, there are many possible tips that have to be implemented.

First of all, gravity should be taken into account on the code in order to make it more realistic.

Another work of interest, that could be useful for Oil & Gas industries, would be a complete characterization of the materials used in the simulations. In fact, while sandstone presents more or less the same properties wherever in the world, shale rock may vary a lot (J.M.R.J. Huyghe, personal communication). This is the reason why in this Project sandstone has been chosen.

Moreover, despite sandstone materials, shale rock formations present a swelling behavior during hydraulic fracturing processes. Hence, also this characteristic should be accounted for in the code. In order to better represent the behavior of rock formations submitted to fracturing processes, it would be better to consider a special orthotropic material: a transverse isotropic material. A transversely isotropic material is one characterized by physical properties which are symmetric with respect to an axis that is normal to a plane of isotropy. This transverse plane has infinite planes of symmetry. Hence, within this plane, the material properties are the same in all directions. Such materials are also known as “polar anisotropic” materials. Details will be given in Appendix B.

An interesting next step is to extend the current method to 3D situations, especially for hydraulic fracturing. X-FEM has been used before in 3D situations but none of them addressed hydraulic fracturing [88]. However, some more experimental tests should be performed in order to validate the numerical models developed, especially to investigate the stepwise propagation behavior.

Finally, the stepwise advancement may be relevant for earthquake engineering [89]. Thus, a possible further investigation could be the coupling between the current code and a tool for capturing and solving the acoustic wave propagation related to hydraulic fracturing operations and, probably, to the physical stepwise advancement. This could

---

lead to sharply capture pressure fluctuations and acoustic wave propagations simultaneously and, therefore, to better understand the stepwise advancement.

---



## 5: Conclusions

In this Thesis a X-FEM formulation for 2D poroelasticity is presented. The numerical model can simulate crack propagation for Mode I of fracture mechanics in a fully saturated medium. The fluid flow from the formation into the crack is accounted for. The research goal has been investigated analyzing the behavior of three similar meshes characterized by the fact of having different mesh sizes. Crack propagation occurs firstly, and by applying a lower load, for smoother meshes than coarsest ones. In the context of consolidation phenomenon of the porous material, this can be explained as a more accurate tensile stress transfer from the fluid to the solid skeleton. With respect to the mesh independence problem, the numerical model is robust for stiffer materials with a short process zone (low fracture toughness). The permeability of the material also plays a key role.

From this work it can be concluded that the model is, at least, not mesh dependent. A weak mesh independence of the model has been shown, although a finer mesh is needed. Indications about a physical stepwise advancement of the fracture through the material have been found. However, more efficient calculation systems need to be used before such a conclusion can be drawn. Comparing rough meshes with more refined meshes, the X-FEM model seems to yield smooth solutions for a phenomenon which in nature is not smooth. The results of this work strongly indicate that the X-FEM in combination with a cohesive law description can become a reliable tool to model stepwise fracture propagation in porous materials. Therefore, further experimental and numerical analysis are required. Finally, from an industrial point of view the main question is whether this kind of X-FEM model can be extended to three-dimensional hydraulic fracturing situations.

## 6: Bibliography

- [1] <http://en.skifergas.dk/technical-guide/what-is-hydraulic-fracturing.aspx>.
- [2] <http://www.bp.com/en/global/corporate/sustainability/the-energy-future/unconventional-gas-and-hydraulic-fracturing.html>.
- [3] B. Aadnoy and R. Looyeh. *Petroleum Rock Mechanics. Drilling Operations and Well Design*. Gulf Professional Publishing, 2011.
- [4] Y. Abousleiman, A.H.D. Cheng, L. Cui, E. Detournay, and J.C. Roegiers. Mandel's problem revisited. *Geotechnique*, 46(2):187–195, 1996.
- [5] M.A. Adams. Biomechanics of back pain. *Acupuncture in medicine*, 22(4):178–188, 2004.
- [6] M.A. Adams. Degenerative disc and vertebral disease—basic sciences. *Surgery (Oxford)*, 27(7):297–300, 2009.
- [7] M.A. Adams and P. Dolan. Intervertebral disc degeneration: evidence for two distinct phenotypes. *Journal of Anatomy*, 2012.
- [8] M.A. Adams and P.J. Roughley. What is intervertebral disc degeneration, and what causes it? *Spine*, 31(18):2151–2161, 2006.
- [9] G. Alfano and M.A. Crisfield. Finite element interface models for the delamination analysis of laminated composites. *International Journal for Numerical Methods in Engineering*, 50(7):1701–1736, 2001.
- [10] O. Allix and P. Ladevèze. Interlaminar interface modelling for the prediction of delamination. *Composite Structures*, 22(4):235–242, 1992.
- [11] I. Babuška and J.M. Melenk. The Partition of Unity Method. *International Journal for Numerical Methods in Engineering*, 40(4):727–758, 1997.
- [12] S.A. Baeurle, M.G. Kiselev, E.S. Makarova, and E.A. Nogovitsin. Effect of the counterion behavior on the frictional–compressive properties of chondroitin sulfate solutions. *Polymer*, 50(7):1805–1813, 2009.

- 
- [13] G.I. Barenblatt. The mathematical theory of equilibrium cracks in brittle fracture. *Advances in Applied Mechanics*, 7:55–129, 1962.
- [14] T. Belytschko and T. Black. Elastic crack growth in finite elements with minimal remeshing. *International Journal for Numerical Methods in Engineering*, 45(5):601–620, 1999.
- [15] T. Belytschko, J. Fish, and B.E. Engelman. A finite element with embedded localization zones. *Computer Methods in Applied Mechanics and Engineering*, 70:59–89, 1988.
- [16] M.A. Biot. Le problème de la consolidation des matières argileuses sous une charge. *Ann. Soc. Sci. Bruxelles B*, 55:110–113, 1935.
- [17] M.A. Biot. General theory of three-dimensional consolidation. *Journal of Applied Physics*, 12(2):155–164, 1941.
- [18] J. Bisschop. Drying shrinkage microcracking in cement-based materials. 2002. Dissertation, Delft University of Technology, Delft, The Netherlands.
- [19] T.J. Boone and A.R. Ingraffea. A numerical procedure for simulation of hydraulically-driven fracture propagation in poroelastic media. *International Journal for Numerical and Analytical Methods in Geomechanics*, 14(1):27–47, 1990.
- [20] K.B. Broberg. *Cracks and Fracture*. 1999. San Diego, CA, USA, Academic Press.
- [21] E. Budyn, G. Zi, N. Moës, and T. Belytschko. A method for multiple crack growth in brittle materials without remeshing. *International Journal for Numerical Methods in Engineering*, 61(10):1741–1770, 2004.
- [22] G.T. Camacho and M. Ortiz. Computational modelling of impact damage in brittle materials. *International Journal of Solids and Structures*, 33(20):2899–2938, 1996.
-

- 
- [23] A.H.D. Cheng and E. Detournay. A direct boundary element method for plane strain poroelasticity. *International Journal for Numerical and Analytical Methods in Geomechanics*, 12(5):551–572, 1988.
- [24] O. Coussy. *Mechanics and physics of porous solids*. Wiley, 2011.
- [25] C.W. Cryer. A comparison of the three-dimensional consolidation theories of Biot and Terzaghi. *The Quarterly Journal of Mechanics and Applied Mathematics*, 16(4):401–412, 1963.
- [26] R. de Borst and H.B. Mühlhaus. Gradient-dependent plasticity: formulation and algorithm aspects. *International Journal for Numerical Methods in Engineering*, 35(3):521–539, 1992.
- [27] R. de Borst, J.J.C. Remmers, A. Needleman, and M.A. Abellan. Discrete vs smeared crack models for concrete fracture: bridging the gap. *International Journal for Numerical and Analytical Methods in Geomechanics*, 28(7-8):583–607, 2004.
- [28] R. de Borst, J. Réthoré, and M.A. Abellan. A numerical approach for arbitrary cracks in a fluid-saturated medium. *Archive of Applied Mechanics*, 75(10):595–606, 2006.
- [29] R. de Borst, J. Réthoré, and M.A. Abellan. A precis of two-scale approaches for fracture in porous media. *Lecture Notes on Composite Materials*, pages 149–171, 2009.
- [30] E. Detournay and A.H.D. Cheng. Fundamentals of Poroelasticity. Chapter 5 in *Comprehensive Rock Engineering: Principles, Practice and Projects*, Vol. II, Analysis and Design Method, ed. C. Fairhurst, Pergamon Press,.
- [31] E. Detournay and A.H.D. Cheng. Plane strain analysis of a stationary hydraulic fracture in a poroelastic medium. *International Journal of Solids and Structures*, 27(13):1645–1662, 1991.
-

- 
- [32] J. Dolbow, N. Moës, and T. Belytschko. Discontinuous enrichment in finite elements with a partition of unity method. *Finite elements in analysis and design*, 36(3):235–260, 2000.
- [33] D.S. Dugdale. Yielding of steel sheets containing slits. *Journal of the Mechanics and Physics of Solids*, 8(2):100–104, 1960.
- [34] P. Dumstorff and G. Meschke. Crack propagation criteria in the framework of x-fem-based structural analyses. *International Journal for Numerical and Analytical Methods in Geomechanics*, 31(2):239–259, 2007.
- [35] S. Ehrlich, N. Wolff, R. Schneiderman, A. Maroudas, K.H. Parker, and C.P. Winlove. The osmotic pressure of chondroitin sulphate solutions: experimental measurements and theoretical analysis. *Biorheology*, 35(6):383–397, 1998.
- [36] S.J. Ferguson, K. Ito, and L.P. Nolte. Fluid flow and convective transport of solutes within the intervertebral disc. *Journal of biomechanics*, 37(2):213–221, 2004.
- [37] Y. Goto, Y. Watanaber, T. Kasugai, and M. Obata. Elastic Buckling Phenomenon Applicable to Deployable Rings. *International Journal of Solids and Structures*, 27(7):893–909, 1992.
- [38] A.A. Griffith. The phenomena of rupture and flow in solids. *Philosophical transactions of the Royal Society of London. Series A, containing papers of a mathematical or physical character*, 221:163–198, 1920.
- [39] A. Hillerborg, Modeér M., and P.E. Petersson. Analysis of a crack formation and crack growth in concrete by means of fracture mechanics and finite elements. *Cement and Concrete Research*, 6:773–782, 1976.
- [40] N.C. Huang and S.G. Russell. Hydraulic fracturing of a saturated porous medium-ii: Special cases. *Theoretical and Applied Fracture Mechanics*, 4(3):215–222, 1985.
-

- 
- [41] J.W. Hutchinson and A.G. Evans. Mechanics of materials: top-down approaches to fracture. *Acta Materialia*, 48:125–135, 2000.
- [42] J.M. Huyghe and P.H.M. Bovendeerd. Biological mixtures. *Modeling Coupled Phenomena in Saturated Porous Materials, POROCENT, Bydgoszcz*, pages 1–45, 2003.
- [43] J.M. Huyghe and C.J.M. Jongeneelen. 3D non-affine finite strains measured in isolated bovine annulus fibrosus tissue samples. *Biomechanics and modeling in mechanobiology*, 11(1):161–170, 2012.
- [44] C. Hwu. *Anisotropic elastic plates*. Springer, 2010.
- [45] C.E. Inglis. Stresses in a plate due to the presence of cracks and sharp corners. *Spie Milestone series MS*, 137:3–17, 1997.
- [46] A.R. Ingraffea and V. Saouma. Numerical modelling of discrete crack propagation in reinforced and plain concrete. *Fracture Mechanics of Concrete*, pages 171–225, 1985. Martinus Nijhoff Publishers, Dordrecht.
- [47] G.R. Irwin. Analysis of stresses and strains near the end of a crack traversing a plate. *Journal of Applied Mechanics*, 1957.
- [48] F. Irzal, J.C.J. Remmers, J.M.R.J. Huyghe, and R. de Borst. A large deformation formulation for fluid flow in a progressively fracturing porous material. *Computer Methods in Applied Mechanics and Engineering*, 256:29–37, 2013.
- [49] M. Jirasék. Embedded crack models for concrete fracture. *Computational Modelling of Concrete Structures*, EURO C-98(1):291–300, 1998.
- [50] B.D. Johnson, D.J. Beebe, and W.C. Crone. Effects of swelling on the mechanical properties of a pH-sensitive hydrogel for use in microfluidic devices. *Materials Science and Engineering: C*, 24(4):575–581, 2004.
- [51] K.R. Keshari, J.C. Lotz, T.M. Link, S. Hu, S. Majumdar, and J. Kurhanewicz. Lactic acid and proteoglycans as metabolic markers for discogenic back pain. *Spine*, 33(3):312–317, 2008.
-

- 
- [52] F. Kesicki. Modelling the potential for industrial energy efficiency in IEA's WEO. 2013. International Energy Workshop, Paris.
- [53] A.R. Khoei, O.R. Barani, and M. Mofid. Modeling of dynamic cohesive fracture propagation in porous saturated media. *International Journal for Numerical and Analytical Methods in Geomechanics*, 35(10):1160–1184, 2010.
- [54] J. Korsawe, G. Starke, W. Wang, and O. Kolditz. Finite element analysis of poro-elastic consolidation in porous media: Standard and mixed approaches. *Computer Methods in Applied Mechanics and Engineering*, 195(9):1096–1115, 2006.
- [55] F. Kraaijeveld. *Propagating discontinuities in ionized porous media*. PhD thesis, Technische universiteit Eindhoven, 2009.
- [56] F. Kraaijeveld and J. Huyghe. Propagating cracks in saturated ionized porous media. *Multiscale Methods in Computational Mechanics*, pages 425–442, 2011.
- [57] F. Kraaijeveld, J.M. Huyghe, J.J.C. Remmers, and R. de Borst. 2D mode I crack propagation in saturated ionized porous media using partition of unity finite elements. *Journal of Applied Mechanics: Transactions of the ASME*, 80, 2013.
- [58] F. Kraaijeveld, J.M.R.J. Huyghe, J.C.J Remmers, and R. de Borst. Two-dimensional mode I crack propagation in saturated ionized porous media using partition of unity finite elements. *Journal of Applied Mechanics: Transactions of the ASME*, 80:0209071–02090712, 2013.
- [59] Y. Lanir. Biorheology and fluid flux in swelling tissues. I. bicomponent theory for small deformations, including concentration effects. *Biorheology*, 24(2):173, 1987.
- [60] R.W. Lewis and B.A. Schrefler. *The finite element method in the static and dynamic deformation and consolidation of porous media*. Wiley, Chichester, 1998.
- [61] J. Mandel. Consolidation des sols (étude mathématique)\*. *Geotechnique*, 3(7):287–299, 1953.
-

- 
- [62] C.J. Massey, C.C. van Donkelaar, E. Vresilovic, A. Zavaliangos, and M. Marcolongo. Effects of aging and degeneration on the human intervertebral disc during the diurnal cycle: A finite element study. *Journal of Orthopaedic Research*, 30(1):122–128, 2011.
- [63] J.M. Melenk and I. Babuška. The partition of unity finite element method: basic theory and applications. *Computer methods in applied mechanics and engineering*, 139(1):289–314, 1996.
- [64] N. Moës and T. Belytschko. Extended finite element method for cohesive crack growth. *Engineering Fracture Mechanics*, 69:813–833, 2002.
- [65] N. Moës, J. Dolbow, and T. Belytschko. A Finite Element Method for Crack Growth without Remeshing. *International Journal for Numerical Methods in Engineering*, 46(1):131–150, 1999.
- [66] T. Mohammadnejad and A.R. Kohei. An extended finite element method for hydraulic fracture propagation in deformable porous media with the cohesive crack model. *Finite Elements in Analysis and Design*, (73):77–95, 2013.
- [67] A. Needleman. A continuum model for void nucleation by inclusion debonding. *Journal of Applied Mechanics*, 54:525–531, 1987.
- [68] D. Ngo and A.C. Scordelis. Finite element analysis of reinforced concrete beams. *Journal of the American Concrete Institute*, 64:152–163, 1967.
- [69] M. Ortiz, Y. Leroy, and A. Needleman. A finite element method for localized failure analysis. *Computer Methods in Applied Mechanics and Engineering*, 61:189–214, 1987.
- [70] S.L. Philipp, F. Afsar, and A. Gudmundsson. Effects of mechanical layering on hydrofracture emplacement and fluid transport in reservoirs. *Frontiers in Earth Science*, 2013.
- [71] F. Pizzocolo, J.M. Huyghe, and K. Ito. Mode I crack propagation in hydrogels is step wise. *Engineering Fracture Mechanics*, 2012.
-



- 
- [72] F. Pizzocolo, J.M. Huyghe, J.J.C. Remmers, K. Ito, and R. de Borst. A mixed hybrid formulation for 2D poroelasticity with discontinuity.
- [73] S. Razaq, R.J. Wilkins, and J.P.G. Urban. The effect of extracellular ph on matrix turnover by cells of the bovine nucleus pulposus. *European Spine Journal*, 12(4):341–349, 2003.
- [74] E.W. Remij. *Arbitrary crack propagation and nucleation in porous materials*, Eindhoven University of Technology, 2013.
- [75] J.C.J. Remmers, R. de Borst, and A. Needleman. A cohesive segments method for the simulation of crack growth. *Computational Mechanics*, 31(1-2):69–77, 2003.
- [76] J.J.C. Remmers. *Discontinuities in materials and structures*. PhD thesis, Delft University of Technology, 2006.
- [77] J.J.C. Remmers, R. de Borst, and A. Needleman. The simulation of dynamic crack propagation using the cohesive segments method. *Journal of the Mechanics and Physics of Solids*, 56(1):70–92, 2008.
- [78] J. Réthoré, R. de Borst, and M.A. Abellan. A two-scale approach for fluid flow in fractured porous media. *International Journal for Numerical Methods in Engineering*, 71(7):780–800, 2007.
- [79] J. Réthoré, A. Gravouil, and A. Comberscure. An energy-conserving scheme for dynamic crack growth using the extended finite element method. *International Journal for Numerical Methods in Engineering*, 63(5):631–659, 2005.
- [80] J.R. Rice. A path independent integral and the approximate analysis of strain concentrations by notches and cracks. *Journal of Applied Physics*, 35:379–386, 1968.
- [81] J.R. Rice and M.P. Cleary. Some basic stress diffusion solutions for fluid-saturated elastic porous media with compressible constituents. *Rev. Geophys. Space Phys*, 14(2):227–241, 1976.
-

- 
- [82] J.G. Rots. Strain-softening analysis of concrete fracture specimens. *Fracture Toughness and Fracture Energy of Concrete*, pages 137–148. F.H. Wittman, Eds., Amsterdam. Elsevier Science Publishers, 1986.
- [83] J.G. Rots. Smearred and discrete representations of localized fracture. *International Journal of Fracture*, 51:45–59, 1991.
- [84] J.C.J. Schellekens and R. De Borst. A nonlinear finite-element approach for the analysis of mode-I free edge delamination in composites. *International Journal of Solids and Structures*, 30(9):1239–1253, 1993.
- [85] J.C.J. Schellekens and R. De Borst. Free edge delamination in carbon-epoxy laminates: a novel numerical/experimental approach. *Composite Structures*, 28:357–373, 1994.
- [86] B.A. Schrefler, S. Secchi, and L. Simoni. On adaptive refinement techniques in multi-field problems including cohesive fracture. *Computer methods in applied mechanics and engineering*, 195(4):444–461, 2006.
- [87] Y. Schroder. *Putting pressure on the spine: an osmovoiscoelastic FE model of the intervertebral disc*. PhD thesis, Eindhoven University of Technology, 2008.
- [88] S. Secchi and B.A. Schrefler. A method for 3-D hydraulic fracturing simulation. *International Journal of Fracture*, 178:245–258, 2012.
- [89] S. Secchi and B.A. Schrefler. Hydraulic fracturing and its peculiarities. *Asia Pacific Journal on Computational Engineering*, 1(8), 2014.
- [90] S. Secchi, L. Simoni, and B.A. Schrefler. Mesh adaptation and transfer schemes for discrete fracture propagation in porous materials. *International Journal for Numerical and Analytical Methods in Geomechanics*, 31(2):331–345, 2007.
- [91] J.C. Simo, J. Oliver, and F. Armero. An analysis of strong discontinuities induced by softening relations in rate-independent solids. *Computational Mechanics*, 12:277–296, 1993.
-

- 
- [92] P. Stevens. The ‘shale gas revolution’: developments and changes.
- [93] K. Terzaghi. Die berechnung der durchlassigkeitsziffer des tones aus dem verlauf der hydrodynamischen spannungserscheinungen. *Sitzungsberichte der Akademie der Wissenschaften in Wien, Mathematisch-Naturwissenschaftliche Klasse, Abteilung IIa*, 132:125–138, 1923.
- [94] K. Terzaghi. Theoretical soil mechanics. 1943.
- [95] F. Tzschichholz and H.J. Herrmann. Simulations of pressure fluctuations and acoustic emission in hydraulic fracturing. *Physical Review*, E(5):1961–1970, 1995.
- [96] J.F. Unger, S. Eckardt, and C. Könke. Modelling of cohesive crack growth in concrete structures with the extended finite element method. *Computer methods in applied mechanics and engineering*, 196(41):4087–4100, 2007.
- [97] J.P. Urban, S. Roberts, et al. Degeneration of the intervertebral disc. *Arthritis Research and Therapy*, 5(3):120–138, 2003.
- [98] J.P.G. Urban and A. Maroudas. Swelling of the intervertebral disc in vitro. *Connective tissue research*, 9(1):1–10, 1981.
- [99] J.P.G. Urban, S. Roberts, and J.R. Ralphs. The nucleus of the intervertebral disc from development to degeneration. *American Zoologist*, 40(1):53–061, 2000.
- [100] J.P.G. Urban and C.P. Winlove. Pathophysiology of the intervertebral disc and the challenges for mri. *Journal of Magnetic Resonance Imaging*, 25(2):419–432, 2007.
- [101] M.J. van den Bosch, P.J.G. Schreurs, and M.G.D. Geers. An improved description of the exponential Xu and Needleman cohesive zone law for mixed-mode decohesion. *Engineering Fracture Mechanics*, 73(9):1220–1234, 2006.
- [102] J.M.G. van Mier. Fracture Processes of Concrete. 1997. Boca Raton, Florida, CRC Press.
-

- 
- [103] P.A. Vermeer and A. Verruijt. An accuracy condition for consolidation by finite elements. *International Journal for Numerical and Analytical Methods in Geomechanics*, 57(9):1243–1258, 2003.
- [104] G.N. Wells and L.J. Sluys. Discontinuous analysis of softening solid under impact loading. *International Journal for Numerical and Analytical Methods in Geomechanics*, 25(7):691–709, 2001.
- [105] G.N. Wells and L.J. Sluys. A new method for modelling cohesive cracks using finite elements. *International Journal for Numerical Methods in Engineering*, 50(12):2667–2682, 2001.
- [106] G.N. Wells, L.J. Sluys, and R. de Borst. Simulating the propagation of displacement discontinuities in a regularized strain-softening medium. *International Journal for Numerical Methods in Engineering*, 53(5):1235–1256, 2002.
- [107] S. Wognum, J.M. Huyghe, and F.P.T. Baaijens. Influence of osmotic pressure changes on the opening of existing cracks in 2 intervertebral disc models. *Spine*, 31(16):1783–1788, 2006.
- [108] K. Wuertz, K. Godburn, and J.C. Iatridis. Msc response to ph levels found in degenerating intervertebral discs. *Biochemical and biophysical research communications*, 379(4):824–829, 2009.
- [109] X.P. Xu and A. Needleman. Void nucleation by inclusion debonding in a crystal matrix. *Modelling and Simulation in Materials Science and Engineering*, 1(2):111–132, 1993.
- [110] X.P. Xu and A. Needleman. Numerical simulations of fast crack growth in brittle solids. *Journal of the Mechanics and Physics of Solids*, 42(9):1397–1434, 1994.
- [111] C. Yu, A. Pandolfi, M. Ortiz, D. Coker, and A.J. Rosakis. Three-dimensional modeling of intersonic shear-crack growth in asymmetrically loaded unidirectional composite plates. *International Journal of Solids and Structures*, 39(25):6135–6157, 2002.
-

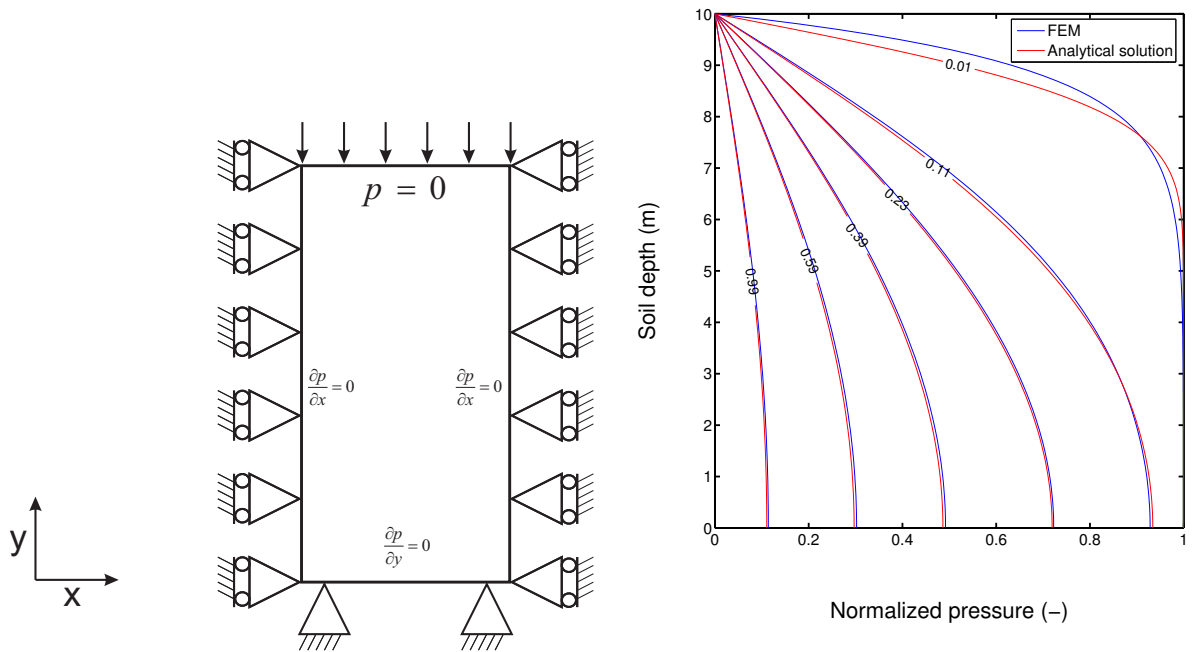
- [112] A. Zehnder. Lecture notes on fracture mechanics. *Cornell University*, 2007.
-

# Appendix A

## Accuracy of the numerical model

The accuracy of the numerical model has been tested with different known analytical solutions [74]. Here two examples of interest, with respect to the target of the work, are performed. However, note that these examples do not consider fracturing processes.

### Consolidation



(a) Representation of the 1D consolidation problem.

(b) Normalized pressure in the soil for various times. The number in the line represents a normalized time defined as  $t_d = \frac{ckt}{H^2}$ . The analytical solution is borrowed from Terzaghi [93, 94].

Figure 1: 1D consolidation problem.

A 1D consolidation problem is considered (Figure 1a). The top surface is drained, so that  $p = 0$ , and it is vertically loaded with a load  $\sigma_{yy}$ . The bottom surface is

constrained, thus displacements are not allowed in both directions, moreover it is also impervious  $\frac{\delta p}{\delta y} = 0$ . The two vertical walls are also impervious and constrained in x-direction, forcing fluid flow through the top surface. The analytical solution based on Terzaghi's theory can be found in [54, 24]. The parameters used in the numerical model are listed in Table 1. The mesh is made of squared elements with width  $\Delta x = 0.1m$ .

The normalized hydrostatic pressure of the soil is shown in Figure 1b at various times. Consolidation behavior can be observed. At early times, almost all the load is carried by the water. Water flows out of a slice of the porous material and the load is carried by the solid skeleton. The numerical model calculates a hydrostatic pressure distribution, that is consistent with Terzaghi's analytical solution.

Table 1: Model parameters used for the consolidation benchmark.

E	=	3.0e4	[Pa]	H	=	10	[m]	$\sigma_{yy}$	=	1000	[Pa]
$\nu$	=	0.2	[-]	$\Delta t$	=	600	[s]				
k	=	10e-10	$[\frac{m^4}{Ns}]$	$\bar{\theta}$	=	1.0	[-]				

### Mandel Cryer (unconfined compression)

Biot's theory of poroelasticity [17] describes the coupling between mechanical and pressure responses. This coupling is not present in the original consolidation theory presented by Terzaghi. In 1953 Mandel [61] presented a solution of Biot's consolidation theory for a cylindrical sample compressed between two parallel plates. This solution describes a non-monotonic pressure response. In 1963 Cryer [25] obtained a similar response at the center of a sphere that consolidates under a hydrostatic pressure. Both results quantify the effect of the Poisson's ratio on the development and dissipation of the pore pressure and are now referred to as the Mandel-Cryer effect [4, 23].

In Mandel's problem a cross-section of a poroelastic infinitely long sample is placed between two rigid plates (Figure 2). Due to the infinite length of the specimen the problem can be considered as a plane strain problem. Both sides of the specimen are stress-free in normal and shear direction and free drainage is prescribed with zero pressure. The two rigid plates are impervious. All model parameters are given in Table

Table 2: Model parameters used in the isotropic Mandel-Cryer benchmark.

$E$	$=$	1.5	[Mpa]	$a$	$=$	2.5	[mm]	$B$	$=$	1.0	[-]
$\nu$	$=$	0.2	[-]	$b$	$=$	0.5	[mm]	$\Delta t$	$=$	150	[s]
$\nu_u$	$=$	0.5	[-]	$F$	$=$	0.05	[N]	$\bar{\theta}$	$=$	1.0	[-]
$k$	$=$	2.8e-4	$[\frac{mm^4}{Ns}]$								

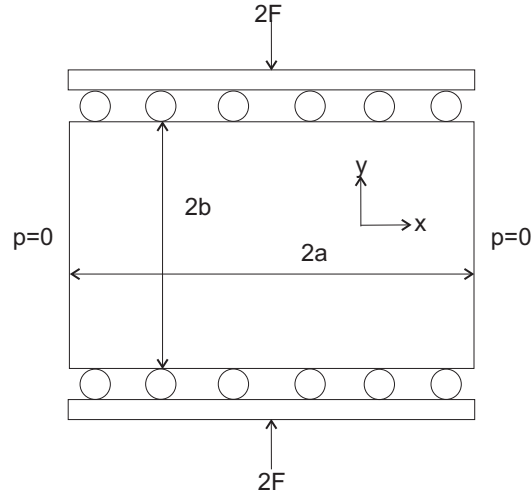


Figure 2: Scheme of the Mandel-Cryer problem.

2. The mesh consists of squared elements with a element size  $\Delta x = 0.05mm$ .

At time  $t = 0^+$  a uniform compression force of  $2F$  is applied to both plates. This initially creates a uniform pore pressure generated by the so-called Skempton effect. The initial pore pressure is half the amount of the applied load ( $\frac{F}{a}$ ). Due to free drainage at the lateral sides the pressure dissipates. The initial pore pressure is added to the compressive stiffness of the sample. At the lateral sides drainage is faster than in the middle of the sample. A load transfer occurs from the softer sides towards the stiffer center. This initially causes the pressure in the center to increase above the initial pressure jump. Eventually all the pore pressure must dissipate due to the free drainage.

Mandel presented only the exact solution for the pore pressure. Both solid and fluid constituents are assumed to be incompressible and the material is considered isotropic. Cheng and Detournay [23] listed the solutions for the displacement, stress, pressure



and flow for the Mandel problem. The normalized pressure for several times across the sample can be seen in Figure 3. The rise of pore pressure in the center is observed for the first two times plotted in Figure 3. This is also shown in Figure 4a, where the pressure in the center of the sample is plotted as a function of time. Validations of the numerical model with the analytical solutions for the x-displacement of the right side, y-displacement of the top plate, and flow in x-direction, at the right side are shown in Figure 4.

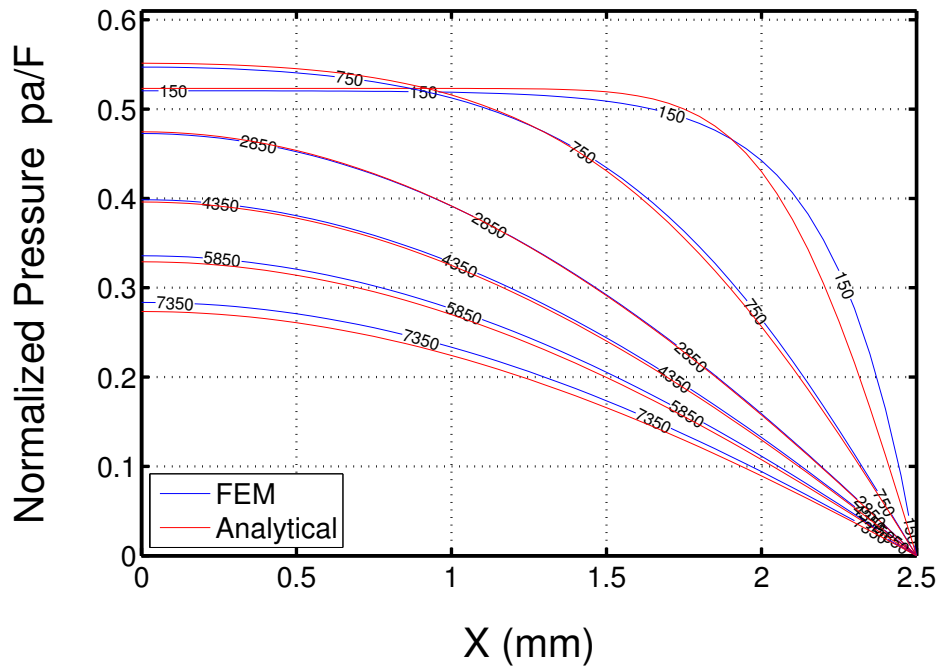
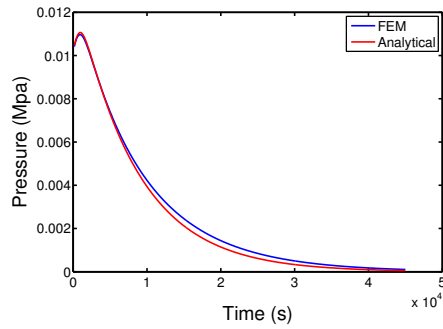
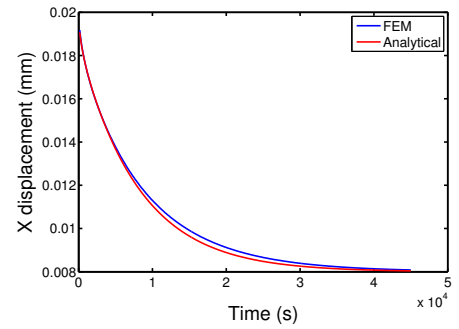


Figure 3: Normalized pressure  $\frac{pa}{F}$  over the sample in x-direction, where  $x = 0$  is in the center. The numbers drawn in the line indicate the time in seconds. Analytical solution from Mandel(1953) [61].

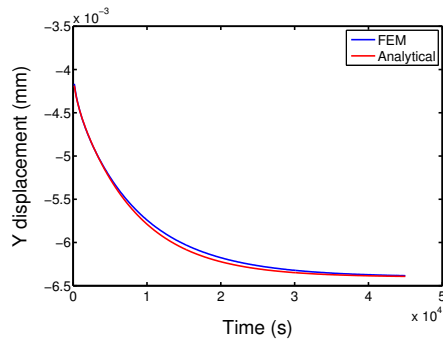
In a confined compression situation the numerical model calculates a hydrostatic pressure distribution that is consistent with Terzaghi's theory (Figure 1b). At early times the difference between the numerical result and the analytical solution is most significant. This difference decreases over time. The analytical solution is slightly in



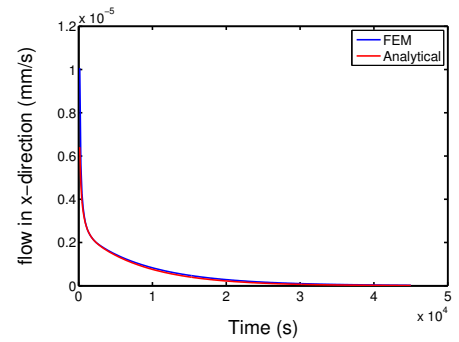
(a) The pore pressure response (MPa) in the center of the sample over time. It can be seen that there is a non-monotonic pressure increase shortly after the loading.



(b) The x displacement (mm) of the right side of the sample shown as a function of time (s).



(c) The y displacement (mm) of the top plate shown as a function of time (s).



(d) The flow (mm/s) in x-direction of the right side of the sample shown as a function of time (s).

Figure 4: Results for Mandel's problem. Analytical solutions from Cheng and Detournay [23].

front of the numerical result at later times. Similar behavior is found in the Mandel-Cryer problem (Figure 3). Here the difference between the analytical and numerical values increases over time. The lagging behind of the numerical solution could be attributed to the implicit time scheme used. However, the problem did not disappear by using a Crank-Nicholson ( $\bar{\theta} = 0.5$ ) time scheme. Taking a time step closer to the minimum time step in equation (2.67) may reduce the effect [55].

It can be concluded that the two accuracy checks are fulfilled successfully.

---

# Appendix B

## Transverse Isotropy

This section describes the constitutive behavior of a transverse isotropic material. Such a material is an orthotropic material with one plane of isotropy. This section has been introduced since the simulations of this Thesis considers an isotropic material. However, in order to better describe a shale/sandstone rock formation, a transverse isotropic material would be more adequate. Here, the mathematical formulation of the problem, that can be implemented in the code, is given.

A material with parallel fibers in one direction which are randomly distributed in the cross-section satisfies this description. A plane strain description in the x-y plane is assumed. It is assumed also that the fibers are aligned in the  $x^*$  direction (see Figure 5). The linear elastic constitutive effective stress formulation under small deformations is the following [4]:

$$\begin{pmatrix} \sigma_{e_{xx}}^* \\ \sigma_{e_{yy}}^* \\ \sigma_{e_{xy}}^* \end{pmatrix} = \underline{\mathbf{S}}_{ani}^* \begin{pmatrix} \epsilon_{xx}^* \\ \epsilon_{yy}^* \\ \gamma_{xy}^* \end{pmatrix} \quad (1)$$

with  $\underline{\mathbf{S}}_{ani}^*$  being a [3x3] stiffness matrix:

$$\underline{\mathbf{S}}_{ani}^* = \begin{pmatrix} \frac{E_l^2(1-\nu_{tt})}{E_l(1-\nu_{tt})-2E_t\nu_{tt}^2} & \frac{E_l E_t \nu_{lt}}{E_l(1-\nu_{tt})-2E_t\nu_{tt}^2} & 0 \\ \frac{E_l E_t \nu_{lt}}{E_l(1-\nu_{tt})-2E_t\nu_{tt}^2} & \frac{E_t(E_l-E_t\nu_{lt}^2)}{(1+\nu_{tt})[E_l(1-\nu_{tt})-2E_t\nu_{tt}^2]} & 0 \\ 0 & 0 & G_{lt} \end{pmatrix} \quad (2)$$

here  $E_l$  and  $E_t$  are respectively the longitudinal and transversal Young's modulus,  $\nu_{lt}$  and  $\nu_{tt}$  are the Poisson's ratios representing the compressive strain in the direction of the second subscript due to a tensile stress in the direction of the first subscript, and  $G_{lt}$  is the shear modulus in the x-y plane. Here, based on symmetry, the following

identity was used:

$$\frac{\nu_{lt}}{El} = \frac{\nu_{tl}}{Et} \quad (3)$$

The stress strain relations used in the numerical model are defined in the global x-y coordinate system. It is therefore necessary to transform the stress  $\underline{\sigma}^*$  to the global stress  $\underline{\sigma}$ . This can be done by applying the following matrix transformations:[44]

$$\underline{\sigma}^* = \underline{\mathbb{T}}\underline{\sigma} \quad (4)$$

$$\underline{\epsilon}^* = \underline{\mathbb{R}}\underline{\mathbb{T}}\underline{\mathbb{R}}^{-1}\underline{\epsilon} \quad (5)$$

where  $\underline{\mathbb{T}}_r$  is the rotation matrix:

$$\underline{\mathbb{T}}_r = \begin{pmatrix} \cos^2 \theta_f & \sin^2 \theta_f & 2 \sin \theta_f \cos \theta_f \\ \sin^2 \theta_f & \cos^2 \theta_f & -2 \sin \theta_f \cos \theta_f \\ -\sin \theta_f \cos \theta_f & \sin \theta_f \cos \theta_f & \cos^2 \theta_f - \sin^2 \theta_f \end{pmatrix} \quad (6)$$

The matrix  $\underline{\mathbb{R}}$  is introduced because the transformation rule is only valid for elastic shears [44]. The factor 2 in matrix  $\underline{\mathbb{R}}$  accounts for the difference between the elastic and engineering shear strain in the constitutive equation.

$$\underline{\mathbb{R}} = \begin{pmatrix} 1 & 0 & 0 \\ 0 & 1 & 0 \\ 0 & 0 & 2 \end{pmatrix} \quad (7)$$

Equation (1) can be written in short as:

$$\underline{\sigma}^* = \underline{\mathbb{S}}_{ani}^* \underline{\epsilon}^* \quad (8)$$

and for the stress in the global coordinate system:

$$\underline{\sigma} = \underline{S}_{ani} \underline{\epsilon} \quad (9)$$

Filling in equations (4) and (5) in (8) results in:

$$\underline{\sigma} = \underline{T}_r^{-1} \underline{S}_{ani}^* \underline{R} \underline{T}_r \underline{R}^{-1} \underline{\epsilon} \quad (10)$$

Thus the stress strain relation in the global x-y coordinate system for a transverse isotropic material rotated with angle  $\theta_f$  is given by stiffness matrix  $\underline{S}_{ani}$ :

$$\underline{S}_{ani} = \underline{T}_r^{-1} \underline{S}_{ani}^* \underline{R} \underline{T}_r \underline{R}^{-1} \quad (11)$$

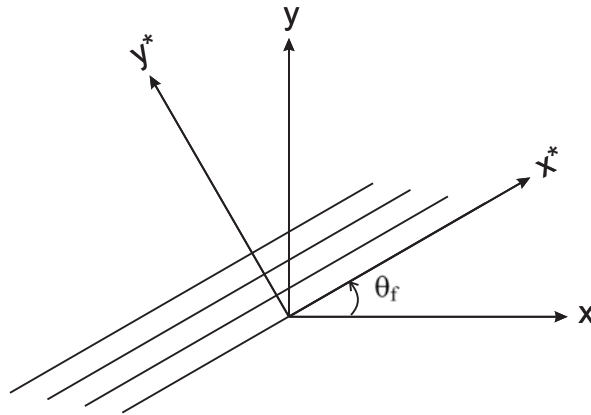


Figure 5: Representation of the fibers rotated around an angle  $\theta_f$  in the x-y coordinate system.



## Acknowledgements

*“Frodo: Non posso farlo, Sam.*

*Sam: Lo so. È tutto sbagliato. Noi non dovremmo nemmeno essere qui. Ma ci siamo.*

*È come nelle grandi storie, padron Frodo. Quelle che contano davvero. Erano piene di oscurità e pericoli. E a volte non volevi sapere il finale. Perché come poteva esserci un finale allegro? Come poteva il mondo tornare com'era dopo che erano successe tante cose brutte? Ma alla fine è solo una cosa passeggera, quest'ombra. Anche l'oscurità deve passare. Arriverà un nuovo giorno. E quando il sole splenderà, sarà ancora più luminoso. Quelle erano le storie che ti restavano dentro. Che significavano qualcosa, anche se eri troppo piccolo per capire il perché. Ma credo, padron Frodo, di capire ora. Adesso so. Le persone di quelle storie avevano molte occasioni di tornare indietro, solo che non l'hanno fatto. Andavano avanti, perché loro erano aggrappate a qualcosa.*

*Frodo: Noi a cosa siamo aggrappati, Sam?*

*Sam: C'è del buono in questo mondo, padron Frodo... Ed è giusto combattere per questo!”*

(J.R.R. Tolkien, ‘Le Due Torri’)

---

Going through this Master’s Thesis has been a wonderful, challenging and truly life-changing experience. One of the joys of completion is to look over the past journey and notice how this work would not have been possible without the invaluable support that I received from many people along this fulfilling road. Here, I would like to take the opportunity and pleasure to thank you.

First of all I would like to offer my special thanks to Jacques Huyghe, with your supervision I had a great freedom to plan and execute my ideas in research without any pressure. This made me to identify my own strengths and drawbacks, and particularly encouraged my self-confidence. Secondly, I would like to express my very great appreciation to Ernst Remij, your critiques and contributions have certainly



improved the quality of my work. Then, I would like to thank David Smeulders, director of the research group “Energy Technology” at the TU/e, that warmly welcomed me as a member of his research team during my internship. I would like to express my deep gratitude to Bernhard Schrefler, without whom this project would never have started. Thank you for having challenged me with this wonderful research topic. I admire your limitless knowledge, your optimistic view on things and how you are able to sharply catch and rephrase complex concepts that I could only describe in a nebulous and long-winded way. Furthermore, I would like to thank the Chairman of the School of Engineering and the Chairman of the Council of Civil Engineering (and promotor in this Thesis) at the University of Padova, Paolo Simonini and Andrea Defina, for always making time in your very busy agenda to talk about new ideas. The friendship that was born with you, especially thanks to the student representative experience, is by far one of the most interesting things of these university years and I will never forget it. Next, I would like to thank the other members of the core committee, in particular Lorenzo Sanavia, for your enthusiasm to be part of the committee and the energy spent for reading this manuscript.

During my time at the TU/e, I have had many nice, happy and inspiring colleagues and some of them, at the end, turned out to become friends. I would like to mention the guys of “The Office” 1.40, with whom I shared my working days: Oğuz, Vignesh, Falco, Berşan, Michel, Noud, Elsa, Arjan, Dario, Jessica, Yoei.

Un caloroso ringraziamento va a tutti gli Amici italiani (e non) con cui ho condiviso questi anni di università, in Italia e all'estero, prima in Francia (a Grenoble), poi in Olanda (ad Eindhoven). Avverto un grande bisogno di ringraziare e ringraziarvi: persone o momenti di persone, nessuno escluso. Da ciascuno ho imparato qualcosa, che ora porto sempre con me. Ma il ringraziamento più grande, importante e sentito è rivolto ai miei genitori, Giovanni e Fanny, che con grandi sacrifici mi hanno sempre educato, sostenuto ed incoraggiato, senza avermi mai privato della libertà di ricercare la mia strada alla felicità. Questa tesi è dedicata ancora una volta a voi, grazie per avermi trasmesso amore incondizionato ogni giorno. Grazie anche a Giuditta, Laura e

---

Simone. Grazie per esserci così come siete, fratelli: non vi cambierei di una virgola, nemmeno se potessi.

Ora guardo indietro la strada percorsa in vostra compagnia, cari tutti, e provo una strana commozione. Perché insieme abbiamo fatto un gran bel viaggio, a ben guardare! (E molti altri ancora ci attendono..).

Ci sono stati anche momenti “pieni di oscurità e di pericolo”, come dice Sam, soprattutto nel Febbraio del terzo anno. Ma “come nelle grandi storie (...) quelle che contano davvero”, giunto alla fine di questo capitolo del libro della mia personalissima storia, “credo di capire (...) adesso so” perché siamo andati, e andiamo, avanti in questa entusiasmante avventura che è la Vita. Abbiamo continuato per due motivi: perché “non dovremmo nemmeno essere qui. Ma **ci siamo**” con il nostro bisogno e il nostro desiderio. E poi perché “**c’è del buono in questo mondo**” che ci precede, ci accompagna, e per cui nulla va perduto e anzi tutto è salvato.

Vi ringrazio, semplicemente per essermi testimoni di questo e compagni nel cammino.

*Eindhoven - Padova, July/Luglio 2014*

↘ Paolo ↵

---

